

Numerical and Experimental Investigations of bend-twist coupling effects for a small wind turbine blade

by

Antariksh Dicholkar

to obtain the degree of Master of Science
in Aerospace Engineering at the Delft University of Technology,
and in Wind Energy at the Technical University of Denmark.

Student number: 4469844
Project duration: November 1, 2016 – August 1, 2017
Thesis committee: Prof. Dr. G. van Bussel, TU Delft, chair of assessment committee
Dr. ir. J. G. Holierhoek, TU Delft, supervisor
Assoc. Prof. Dr. T. Kim, DTU, main supervisor
Dr. F. Zahle, DTU, supervisor
Dr. R. F. Mikkelsen, DTU, supervisor

An electronic version of this thesis is available at <http://repository.tudelft.nl/>.



Technical University
of Denmark



“I almost wish I hadn’t gone down that rabbit-hole — and yet — and yet — it’s rather curious, you know, this sort of life!”

Alice in Wonderland

European Wind Energy Master (EWEM)

Abstract

Technical University of Denmark
Department of Wind Energy

Master of Science

Numerical and Experimental Investigations of bend-twist coupling effects for a small wind turbine blade

by Antariksh DICHOLKAR

Material bend-twist coupling has been widely studied in the research community as a passive control mechanism for a wind turbine. However, there is a lack of research in incorporating it in the rotor design process, with little research being conducted for its application to small wind turbines. The present study focuses on this issue by including bend-twist coupling in the design of a 500W wind turbine by using a combination of parametric studies and a multidisciplinary constrained optimisation approach. By doing so, it aims to establish the effectiveness of bend-twist coupling as a tool for passive load alleviation in small wind turbines. The effectiveness is tested through obtaining a significant decrease in the flapwise blade root bending moment accompanied by only a marginal decrease in the AEP, when compared with the baseline uncoupled turbine.

The reference blade is designed under limitations imposed by the rules of the Small Wind Turbine Design Contest. Bend-twist coupling is introduced in the blades with a fixed aerodynamic design. The rotor performance is analysed in HAWCStab2. The internal structure of the blade is created with the intention of producing flexible blades with a single composite material used throughout the blade. Carbon-epoxy and glass-epoxy FRPs are considered as the material to be chosen in the unidirectional laminae.

The cross-sectional stiffness analysis is conducted using BECAS for a range of fibre layup angles in both carbon-fibre and glass-fibre blades. Carbon outperformed glass for all fibre angles with regard to the amount of coupling seen in the cross-sections. Apart from flapwise bend-twist coupling, other secondary torsion couplings are also present. A load response study is carried out for varying positive fibre layup angles in both carbon-fibre and glass-fibre blades, under steady wind conditions for the operational wind speed range. An increase in the flapwise blade tip displacement and a reduction in the flapwise bending loads with increasing fibre-layup angles is observed for both glass-fibre and carbon-fibre blades.

The HAWTOpt2 aero-structural design tool using OpenMDAO as its core is utilised to implement the optimisation. The spanwise fibre layup angle and laminate thickness distribution are the only design variables that were allowed to be manipulated by the optimiser. The objective function is comprised of two different individual objective functions weighed according to the situation. The optimisation cases failed due to inaccurate gradients of the objective function and constraints. Due to time constraints the manufacturing of the blade and, static load and wind tunnel testing weren't carried out.

Acknowledgements

With this thesis I chose to delve into subjects that I had little or no experience before. The fields of composites, control theory and optimisation formed a major part of my thesis. Having specialised in aerodynamics over the past two years, it certainly was a challenge to pick up skills in these fields and at the same time develop competencies in the multiple design and analysis tools used in this thesis over just 7 months.

This seemingly insurmountable task wouldn't have been possible without the constant support and encouragement of my two supervisors at DTU, Assoc. Prof. Dr. Taeseong Kim and Dr. Frederik Zahle. Their support was especially visible during the countless challenges that were faced in negotiating through the plethora of tools and multidisciplinary concepts involved in this thesis. I would also like to thank my supervisor from TU Delft Dr. Jessica Holierhoek for taking an active interest in the thesis and providing me with crucial advice.

I would like to thank Harmen Martijn Bastiaan for the countless weekends spent at DTU working together on our thesis. I would also like to thank Cody Owen for helping me go through the report even though it was all so sudden. A special thanks to all the EWEM students who have been with me for the past two years for giving me an experience that I will definitely cherish throughout my life.

Lastly, I would like to thank my parents for their unwavering support and belief in my abilities. Their support has kept me going even when I had lost faith in my own abilities.

Contents

Abstract	iii
Acknowledgements	v
1 Introduction	1
2 Methodology	5
2.1 Theoretical content	5
2.1.1 Bend-twist coupling	5
Stiffness coupling	5
Induced torsion	6
Coupling parameter	7
2.1.2 Multidisciplinary constrained optimisation	8
2.2 State-of-the-art	8
3 Aerodynamics, Structure and Control	13
3.1 Competition regulation	13
3.2 Aerodynamic design	14
3.2.1 Airfoil and plaform	14
3.2.2 Rotor performance analysis	16
3.3 Structural design	19
3.3.1 Material properties	19
3.3.2 Internal structure and layup	24
3.4 Controller tuning	26
3.4.1 Controller response	28
3.4.2 Controller gains	29
4 Parametric studies	33
4.1 Stiffness study	33
4.1.1 Results and Discussion	35
Effect of variation in fibre angles	35
4.1.2 Coupling with torsion	36
Flapwise and edgewise bending	36
Edgewise and flapwise shear, and axial extension	39
Secondary couplings	40
4.1.3 Coupling factor	42
4.1.4 Reduced stiffnesses	43
4.1.5 Summary	44
4.2 Load response: Steady	45
4.2.1 Results and Discussion	45
Flapwise loads and deflections	46
AEP and power	50
4.2.2 Summary	54

5	Multidisciplinary Optimisation	57
5.1	Case for optimisation	57
5.2	Optimisation framework and work-flow	58
5.2.1	OpenMDAO	58
5.2.2	HAWTOpt2 work-flow	60
	FUSED-Wind	60
	BECAS	61
	HAWC2	61
5.3	Problem setup	63
5.3.1	Objective function	63
5.3.2	Optimisation cases	64
5.3.3	Design variables and constraints	65
	Case 1	65
	Case 2	65
5.3.4	Optimiser setting	66
5.4	Results and Discussion	68
5.4.1	Case 1	68
5.4.2	Case 2	70
5.5	Challenges in optimisation	74
5.5.1	Scaling, finite difference step and constraint violations	78
5.5.2	Torsional stiffness and solidity	79
5.6	Recommendations	82
5.7	Summary	82
6	Conclusion	85
	Bibliography	91

List of Figures

2.1	Layups for bend-twist coupling and stretch-twist coupling[24]	6
3.1	Power coefficient with varying tip-speed ratios for different airfoil efficiencies [2]	15
3.2	SD-7032 airfoil profile with 10% relative thickness	16
3.3	Comparison of lift curves between SD7032 and SG6043 airfoils [45]	17
3.4	Blade planform properties	18
3.5	Steady state aerodynamic performance of rotor from HawcStab2	20
3.6	Steady state aerodynamic performance of blade at wind speed of 8m/s	21
3.7	Blade cross section profiles	25
3.8	Laminate composition over span	26
3.9	Structural data of blade along span	27
3.11	Gradient polynomial fit of aerodynamic gain scheduling	31
4.1	Cross-sectional stiffness terms at 40% blade length	36
4.2	Comparison of cross-sectional stiffnesses between carbon and glass fibre blades at 40% blade length	37
4.3	Flapwise bending and flap-torsion coupling stiffness terms normalised by their cross-sectional maximum values	38
4.4	K_{44}/K_{46} and K_{46}/K_{66} ratios for carbon and glass fibre blade sections at 40% blade length	41
4.5	Flapwise bending-torsion coupling factor comparison for carbon and glass fibre blade cross-sections	43
4.6	Comparison of reduced cross-sectional stiffnesses between 40% and 90% blade length	44
4.7	Comparison between flapwise structural load and response for varying fibre layup angles	48
4.8	Percentage change in flapwise loads and deflections with varying fibre layup angles, relative to the baseline	48
4.9	Torsional moment for varying positive fibre layup angles	49
4.10	Torsional deflection for varying positive fibre layup angles	49
4.11	Comparison between steady state power curves for varying fibre layup angles	51
4.12	Percentage change in AEP with varying fibre layup angles, relative to the baseline	52
4.13	Angle of attack AoA for varying fibre layup angles	54
4.14	Lift coefficient Cl for varying fibre layup angles	55
4.15	Aerodynamic coefficient curves for SD-7032 airfoil	55
4.16	Wind speed distributions for the given wind climate	56
5.1	HAWTOpt2 internal structure with OpenMDAO and FUSED-Wind core and interfaces to external models [17]	59
5.2	HAWTOpt2 workflow [52]	60

5.3	Thickness perturbation for the blade spar-cap of DTU 10MW wind turbine [40]	61
5.4	Case 1: Value of the objective function with each evaluation for a total of 100 optimiser iterations	70
5.5	Case 1: Comparison of fibre layup angle and laminate thickness spanwise distribution between reference and final version	71
5.6	Case 1: Comparison of flapwise bending, bending-torsion and torsional stiffness spanwise distributions between reference and final version	72
5.7	Case 1: Comparison of aerodynamic moments and maximum flapwise tip deflection between reference and final version	73
5.8	Comparison of spanwise angle of attack distribution between final version and reference case at 7 m/s	73
5.9	Case 2: Value of the objective function with each evaluation for a total of 100 optimiser iterations	74
5.10	Case 2: Comparison of fibre layup angle and laminate thickness spanwise distribution between reference and final version	75
5.11	Case 2: Comparison of flapwise bending, bending-torsion and torsional stiffness spanwise distributions between reference and final version	76
5.12	Case 2: Comparison of aerodynamic moments and maximum flapwise tip deflection between reference and final version	77
5.13	Comparison of solidity and chord of 500W, DTU 10MW and a scaled version of 500W blades normalised by their respective radii	81

List of Tables

3.1	HAWCStab2 aerodynamic model input	17
3.2	Mechanical properties of glass and carbon fibres used in the laminae [30], [4]	23
3.3	Mechanical properties of epoxy matrix used in the laminae	23
3.4	Mechanical properties of the glass-epoxy and carbon-epoxy laminates	23
3.5	Overview of control parameters	28
3.6	Description of control parameters	30
3.7	Aerodynamic gradients calculated by HAWCStab2 and fitted gradients	31
4.1	Description of relevant stiffness terms	35
4.2	Contributions of secondary couplings to the induced torsion for positive fibre layup angles	41
4.3	Maximum and minimum coupling factor for carbon and glass fibre blade cross-sections	43
4.4	Preliminary design summary of the rotor	46
4.5	AEP for steady operation over varying fibre orientations	51
5.1	Design problem formulation: Case 1	66
5.2	Design problem formulation: Case 2	67
5.3	IPOPT settings	68

List of Abbreviations

HAWT	H orizontal A xis W ind T urbine
BTC	B end T wist C oupling
FRP	F ibre R einforced P lastic
MDO	M ultidisciplinary D esign O ptimisation
AEP	A nnual E nergy P roduction
BEM	B lade E lement M omentum
FFD	F ree F orm D eformation
SWT	S mall W ind T urbine
DLC	D esign L oad C ase
HPC	H igh P erformance C omputing
IEC	I nternational E lectrotechnical C ommission
DTU	D anmarks T ekniske U niversitet
UD	U ni- D irectional

List of Symbols

H_{11}, K_{33}	Longitudinal stiffness	[N]
H_{14}, K_{36}	Axial tension-torsion coupling stiffness	[Nm]
H_{22}, K_{44}, K_b	Flapwise bending stiffness	[Nm ²]
$H_{24}, K_{46}, g, K_{btc}$	Flapwise bending-torsion coupling stiffness	[Nm ²]
H_{33}, K_{55}	Edgewise bending stiffness	[Nm ²]
H_{34}, K_{56}	Edgewise bending-torsion coupling stiffness	[Nm ²]
H_{44}, K_{66}, K_t	Torsional stiffness	[Nm ²]
K_{11}	Edgewise shear stiffness	[N]
K_{16}	Edgewise shear-torsion coupling stiffness	[Nm]
K_{22}	Flapwise shear stiffness	[N]
K_{26}	Flapwise shear-torsion coupling stiffness	[Nm]
K_{33}^*	Reduced longitudinal stiffness	[Nm ⁻²]
K_{36}^*	Reduced axial tension-torsion coupling stiffness	[Nm ⁻²]
K_{44}^*	Reduced flapwise bending stiffness	[Nm ⁻²]
K_{46}^*	Reduced flapwise bending-torsion coupling stiffness	[Nm ⁻²]
K_{55}^*	Reduced edgewise bending stiffness	[Nm ⁻²]
K_{56}^*	Reduced edgewise bending-torsion coupling stiffness	[Nm ⁻²]
K_{66}^*	Reduced torsional stiffness	[Nm ⁻²]
K_{11}^*	Reduced edgewise shear stiffness	[Nm ⁻²]
K_{16}^*	Reduced edgewise shear-torsion coupling stiffness	[Nm ⁻²]
K_{22}^*	Reduced flapwise shear stiffness	[Nm ⁻²]
K_{26}^*	Reduced flapwise shear-torsion coupling stiffness	[Nm ⁻²]
F_x	Edgewise shear force	[N]
F_y	Flapwise shear force	[N]
F_t	Tangential aerodynamic force on blade element	[N]
T_z	Axial tension force	[N]
M_x, M_b	Flapwise bending moment	[Nm]
M_xBR	Blade root flapwise bending moment	[Nm]
M_y	Edgewise bending moment	[Nm]
M_z, M_t	Torsional moment	[Nm]
M_xTB	Tower bottom fore-aft moment	[Nm]
r	Radial distance from rotor centre	[m]
R	Rotor radius	[m]
x_p	Planform design variables of wind turbine blade	[-]
x_s	Structural design variables of wind turbine blade	[-]
x_{oper}	Operational design variables of wind turbine	[-]
p	Turbine parameters kept constant in optimisation	[-]
f	Factor assigning weights in objective function	[-]
C	Objective function	[-]
V_0	Speed of oncoming wind	[ms ⁻¹]
V_{avg}	Average wind speed for the given wind climate distribution	[ms ⁻¹]
V_{rated}	Speed of oncoming wind at rated power	[ms ⁻¹]

V_{rel}	Relative wind speed incident on blade element	$[\text{ms}^{-1}]$
V_{cut-in}	Wind turbine cut-in wind speed	$[\text{ms}^{-1}]$
$V_{cut-out}$	Wind turbine cut-out wind speed	$[\text{ms}^{-1}]$
A	Weibull scale parameter	$[\text{ms}^{-1}]$
k	Weibull shape factor	[-]
D	Rotor diameter	[m]
C_P	Power coefficient	[-]
C_{Popt}	Optimal power coefficient	[-]
Cl	Lift coefficient	[-]
Cd	Drag coefficient	[-]
Cm	Aerodynamic moment coefficient	[-]
C_{Topt}	Optimal thrust coefficient	[-]
$P_{rated-aero}$	Aerodynamic rated power of wind turbine	[W]
E_1	Laminate Young's modulus in fibre direction	[GPa]
E_{f1}	Longitudinal Young's modulus of fibre	[GPa]
E_2	Laminate Young's modulus in transverse fibre direction	[GPa]
E_{f2}	Transverse Young's modulus of fibre	[GPa]
E_m	Young's modulus of matrix	[GPa]
G_{12}	In-plane shear modulus of laminate	[GPa]
G_{23}	Out-of-plane shear modulus of laminate	[GPa]
G_{f12}	In-plane shear modulus of fibre	[GPa]
G_{f23}	Out-of-plane shear modulus of fibre	[GPa]
G_m	Shear modulus of matrix	[GPa]
V_f	Volume fraction of fibre in the fibre-matrix laminate	[-]
V_m	Volume fraction of matrix in the fibre-matrix laminate	[-]
K	Constant C_p tracking factor	$[\text{kNmrad}^{-2}\text{s}^2]$
K_{pg}	Proportional gain of constant speed torque controller	$[\text{Nmrad}^{-1}\text{s}^1]$
K_{Ig}	Integral gain of constant speed torque controller	$[\text{Nmrad}^{-1}]$
K_{Pp}	Proportional gain of pitch controller	[s]
K_{Ip}	Integral gain of pitch controller	[-]
K_1	Linear gain scheduling factor	[deg]
K_2	Quadratic gain scheduling factor	$[\text{deg}^2]$
I_r	Turbine rotor area moment of inertia	$[\text{m}^4]$
I_g	Generator area moment of inertia	$[\text{m}^4]$
n_g	Gear box ratio	[-]
Q	Aerodynamic torque	[kNm]
Q_g	Generator torque	[kNm]
c	Blade section chord	[m]
t	Blade laminate thickness	[m]
AoA	Angle of attack	[deg]
AoA_{design}	Design angle of attack	[deg]
AoA_{oper}	Operational angle of attack	[deg]
a	Axial induction factor	[-]
a'	Tangential induction factor	[-]
AEP	Annual energy production	[kWhr/year]
T	Aerodynamic thrust force	[N]
$r01angle$	Fibre layup angle in pressure side laminate	[deg]
$r02angle$	Fibre layup angle in suction side laminate	[deg]
$r01thick$	Laminate thickness in pressure side laminate	[m]
$r02thick$	Laminate thickness in suction side laminate	[m]
B	Number of turbine blades	[-]

A	Area swept by rotor	$[m^2]$
α	Coupling parameter	$[-]$
ϵ_x	Edgewise strain	$[-]$
ϵ_y	Flapwise strain	$[-]$
ϵ_z	Longitudinal strain	$[-]$
κ_x	Flapwise bending curvature	$[-]$
κ_y	Edgewise bending curvature	$[-]$
κ_z	Torsion curvature	$[-]$
β	Total pitch angle of a blade section	$[\text{deg}]$
β_{pitch}	Global pitch angle for all blade sections	$[\text{deg}]$
β_{twist}	Fixed pre-twist angle of blade section	$[\text{deg}]$
δ_z	Torsional deflection of uncoupled blade	$[\text{deg}]$
θ	Induced torsion angle of blade section due to material coupling	$[\text{deg}]$
	Aerodynamic pitch for controller tuning	$[\text{deg}]$
Ω	Wind turbine rotor speed	$[\text{rads}^{-1}], [\text{rpm}]$
Ω_{cut-in}	Rotor speed at wind turbine cut-in	$[\text{rads}^{-1}], [\text{rpm}]$
$\Omega_{cut-out}$	Rotor speed at wind turbine cut-out	$[\text{rads}^{-1}], [\text{rpm}]$
λ, λ_{tip}	Tip-speed ratio	$[-]$
λ_{design}	Design tip-speed ratio	$[-]$
λ_{opt}	Optimal tip-speed ratio	$[-]$
ϕ	Flow angle	$[\text{deg}]$
ν_{12}	In-plane Poisson's ratio	$[-]$
ν_{23}	Out-of-plane Poisson's ratio	$[-]$
ν_{f12}	Poisson's ratio of fibre	$[-]$
ν_m	Poisson's ratio of matrix	$[-]$
ρ_f	Mass density of fibre	$[\text{kgm}^{-3}]$
ρ	Mass density of laminate	$[\text{kgm}^{-3}]$
ρ_m	Mass density of matrix	$[\text{kgm}^{-3}]$
ω_g	Natural frequency of the partial load rigid body rotation pole	$[\text{Hz}]$
ζ_g	Damping ratio of the partial load rigid body rotation pole	$[\text{Hz}]$
ω_p	Natural frequency of the full load rigid body rotation pole	$[\text{Hz}]$
ζ_p	Damping ratio of the full load rigid body rotation pole	$[\text{Hz}]$
r/l	Blade span location normalised by blade length	$[-]$
$\sigma(r/l)$	Solidity of normalised blade span	$[-]$

Chapter 1

Introduction

The growth in wind energy over the last two decades has seen the size of the rotor increase dramatically to facilitate higher energy capture from a single wind turbine. The rotor diameter has grown from 15m powering 0.05MW turbines in 1985 to almost 180m powering 8MW offshore turbines at present date [28]. This increase has been possible due to innovations in blade design and advances in the use of composite materials. An increase in length of the blade is accompanied by a rise in not only the power output but also its mass. The mass in-fact should grow faster than the power with an increase in the rotor area as dictated by the “square-cube” law [28], [23]. However, use of composite materials in the form of glass and carbon fibre reinforced plastics (FRP) are enabling a deviation from this law to produce lighter, flexible blades with slender profiles. They provide higher strength to weight ratio, and better fatigue resistance and stiffness when compared to conventional metals and their alloys [36]. The use of FRPs have also opened up avenues in manipulating the fibre composites to effectuate passive control through bend-twist coupling.

The anisotropic properties of composite FRPs enable for elastic deflections in different directions to be coupled with each other. This property can be utilised to passively realise load reduction in the wind turbine blades by controlling the fibre lay-up such that the blade twists under bending loads. Such a load control mechanism does not involve additional devices and is an outcome of the inherent characteristic of the structure itself. The passive nature of this form of load mitigation makes it an attractive prospect due to the lack of moving parts, actuators and sensors requiring replacement due to failure, thus aiding in a reduction of the cost of energy [10]. The ever-growing rotor sizes and as a consequence the loads on wind turbines, coupled with their deployment in more remote locations, is assigning increasing importance to such forms of “low-maintenance” load alleviation. The structural phenomenon that brings about this load reduction is termed as bend-twist coupling (BTC). The bending of the blades in BTC refers mainly to the flapwise bending that is caused due to the loading in the direction of the oncoming wind. As the blade bends with increasing aerodynamic forces and moments, it twists itself such that there is a reduction in the effective angle of attack which in-turn results in a decrease in the acting aerodynamic loads. Bend-twist coupling can be achieved either through geometric manipulation termed geometric bend-twist coupling or through manipulation of the fibre layup angles in the laminae of the blade, termed material bend-twist coupling. Geometric bend-twist coupling involves altering the geometry of the blades that induces an external torque, such as through sweeping of the blades where aerodynamic loads on the outboard section of the blade induces a torque on the inboard section due to the sweep. Material bend-twist coupling on the other hand utilises the anisotropic properties of composite FRPs to link the load in one direction with a deflection in another. For example applied flapwise bending moment not only produces an expected flapwise deflection but also a torsional deflection.

In the present study, a methodology assimilating material BTC in the rotor design process will be formulated. A wind turbine rotor is designed around specific constraints such as a maximum allowable blade tip displacement so as not to hit the tower, a rated power that should be generated under full load conditions, rotor size, wind class, control type which can be stall or active pitch regulated, constant speed or variable speed, etc. The challenge lies in developing an approach which incorporates BTC in the rotor, satisfying the multiple design constraints and presents feasible alternatives. These alternatives then have to be qualified according to their performance with only the best being carefully selected, thus resulting in a optimally performing turbine. This can be a complicated task due to the inter-dependencies of the different design requirements. For example, depending on the fibre layup angle different degrees of BTC can be achieved, with each configuration uniquely affecting the desired optimum power curve for which the uncoupled rotor blades have been designed. This in turn affects the required pre-twist in the blades to ensure that on activating BTC the blades will generate the aerodynamically optimum power curve. A change in the pre-twist in turn affects the load and the degree of BTC required to mitigate them. Such is the nature of the inter-dependencies of the design variables, objectives and constraints. Because of such complex relationships and the number of design variables, numerical optimisation is made necessary to carry out multidisciplinary design [52].

In this study, wind turbine blades will be designed using a constraint based multidisciplinary optimisation approach as defined by the open source FUSED-wind framework [40] which has been specifically developed for wind energy systems and has been built on NASA's OpenMDAO framework [18]. This framework links a cross-sectional structural analysis tool BECAS [6], [5], [7], [8] and the aeroelastic simulation tool HAWC2 [29] with the HAWTOpt2 [51] optimisation tool. Material BTC will be implemented for a small wind turbine with a rated power of 500W and on a fixed blade planform. Since most of the research in implementing BTC in design is targeted towards multi-megawatt turbines, it is important that there is a study to observe the effects of BTC for small wind turbines that have high rotational speed. The greatest benefits of BTC on small wind turbines could be gained from a reduction in the pitch actuation effort as a result of reduced aggressive controller actions. The turbine is constrained by size, height and rated power requirements as defined by the rules of the *Small Wind Turbine Design Contest 2017*, hosted by NHL University of Applied Sciences in the Netherlands [22]. The aim of this study is to obtain a decrease in the flapwise loads with a marginal decrease in the annual energy production (AEP) through the implementation of BTC in the rotor design. The decision to adopt the design for the competition was to ensure availability of finance to manufacture the rotor.

This thesis aims to defend the hypothesis presented below.

Hypothesis: Material bend-twist coupling is an effective means to substantially decrease the aerodynamic loads in a small wind turbine blade with only a marginal decrease in AEP.

The main research objective is defined followed by sub-objectives.

Main objective: To establish the effectiveness of including material bend-twist coupling (BTC) in a small wind turbine blade by incorporating it in the rotor design process through a multidisciplinary constrained optimisation approach, and comparing the performance of the turbine with that of an uncoupled reference case.

The sub-objectives are:

1. Select the type of BTC that is going to be utilised in the design: twist towards feather or twist towards stall?
2. Select the performance parameters that will judge the effectiveness of including BTC in the design.
3. Identify the materials to be used in the blade and their parameters whose values need to be set based on parametric studies.
4. Define the objective function, design variables and constraints for the optimisation.

A brief outline of the remainder of the report is provided. Chapter 2 focuses on providing a snippet of the underlying theory that is at the core of this thesis. Namely, it explains in brief, the mechanisms governing material bend-twist coupling and multidisciplinary optimisation. A literature review documenting the state-of-the-art in implementation of material BTC and developments in multidisciplinary optimisation, is provided.

Chapter 3 details the aerodynamic design, structural design and tuning of the controller parameters required for the aeroelastic simulations. The rationale employed in selection of the operational parameters such as the rotor speed range, the tip-speed ratio and the rated wind speed is explained. The aerodynamic design is partly constrained by the requirements of the Small Wind Turbine Competition, especially with the wind climate and rotor size. The aerodynamic design including the choice of the airfoil and selection of the blade planform has been performed by Bernitt [30], thus only a qualitative analysis explaining the reasons for the planform choices are described. This is followed by an evaluation of the rotor performance in the linear aeroelastic code HAWCStab2 [21] using BEM and linearised aeroelastic models. Next, the structural design of the baseline blade is finalised by defining the structural properties of the blade through the definition of the internal structure and selection of the composite materials. A primary analysis of the cross-sectional stiffnesses are performed in the structural analysis tool BECAS [6], [5], [7], [8]. Finally, the DTU Wind Energy controller is tuned for the baseline blades and the response of the controller to 1m/s incremental steps of wind speed is recorded.

Chapter 4 focuses on the performance and outcome of two main parametric studies that seek to address some of the sub-objectives of this project. First a stiffness parametric study is performed where the cross-sectional stiffnesses of the blade sections are analysed using the fully populated stiffness matrix outputs by BECAS. This analysis is performed for a carbon-fibre and a glass-fibre blade with the laminate fibre layup angles being varied from -35° to $+35^\circ$. The aim of this study was to identify the contributions of the torsion coupling stiffness terms towards BTC, the fibre angle range that would result in twisting towards feather, the material most conducive to BTC amongst carbon and glass composites, and the dependence of the stiffnesses on cross-sectional dimensions. Next, another parametric study is performed recording the load response of the carbon-fibre and glass-fibre blade at fibre angles conducive to BTC towards feather. The response of the blades is generated through aeroelastic simulation performed in the time-domain aero-servo-hydro-elastic code HAWC2 [29], for steady state winds. The response allows for

choosing the material for the final blade that is the most receptive towards bend-twist coupling. It also provides an indication of the potential benefits of implementing BTC on the 500W turbine blade.

Chapter 5 details the implementation of the the structural design problem in a multidisciplinary optimisation (MDO) environment. A case is made for involving MDO in the design process to implement BTC in a blade with fixed planform. The OpenMDAO [18] optimisation framework with the HAWTOpt2 [52] workflow is introduced and some key concepts are explained. The role of the external analysis codes interfaced for structural analysis and aeroelastic analysis in the HAWTOpt2 workflow is described. The design load cases selected for the MDO and the reasons behind their selection are briefly explained. Next, the optimisation problem setup including the chosen objective function, the design variables and constraints are described with respect to the defined optimisation cases. Finally the results of the MDO are presented followed by a discussion on the impediments encountered during the process. Finally, recommendations are made to carry out a successful MDO and to ensure a better blade design that is conducive to BTC.

Chapter 6 presents the conclusions developed from the implementation of this project.

Chapter 2

Methodology

This chapter begins with section 2.1 focusing on the detailed explanations of theoretical concepts in bend-twist coupling and multidisciplinary optimisation that are central to the thesis. This is followed by section 2.2 involving the presentation of a literature review on the topic of bend-twist coupling and its evolution as a passive control mechanism with the changing control strategies utilised by wind turbines. It also presents the relevant literature concerning multidisciplinary optimisation.

2.1 Theoretical content

This section reviews the theoretical basis of the thesis including the content introduced in section 2.2. The review of these concepts are necessary to understand the analyses presented in the forthcoming chapters. In subsection 2.1.1 the different methods of inducing a bend-twist coupling in the structure are explained. This is followed by a description of the aeroelastic phenomenon that results in passive load alleviation due to bend-twist coupling. Finally, subsection 2.1.1 expounds on the multidisciplinary analysis and optimisation (MDAO) approach of design.

2.1.1 Bend-twist coupling

The development of the theory of bend-twist coupling and its evolution to adapt to the changing control strategies of wind turbines has been extensively covered in section 2.2. In this section the underlying theory of BTC as applied to blade cross-sections, the mathematical formulation of the coupling parameter α and its physical significance will be explained. This will be followed by the definition of the objective function to be used in the optimisation.

Stiffness coupling

Karaolis et al.[24] formulated a theory from classical laminate theory to determine a 4x4 stiffness matrix for a thin-walled monocoque section made from composite FRP. This is shown in Equation 2.1.

Assumptions of Karaolis' theory:

- Blade cross section is a thin-walled beam structure with the thickness much smaller than the chord. As a result the in-plane skin bending and coupling are negligible compared to the beam as a whole [26].
- Only elastic deformations are considered.
- Stress concentrations formed in the skin and their effects are ignored.

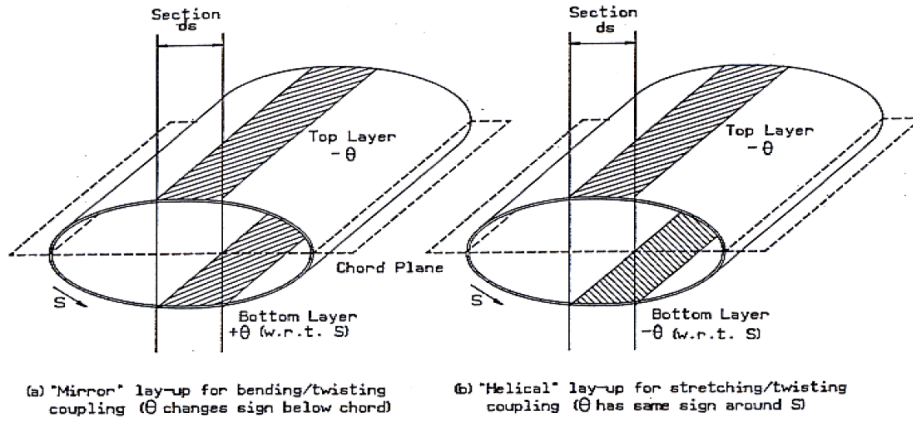


FIGURE 2.1: Layups for bend-twist coupling and stretch-twist coupling[24]

$$\begin{pmatrix} T_z \\ M_x \\ M_y \\ M_z \end{pmatrix} = \begin{bmatrix} H_{11} & H_{12} & H_{13} & H_{14} \\ H_{12} & H_{22} & H_{23} & H_{24} \\ H_{13} & H_{23} & H_{33} & H_{34} \\ H_{14} & H_{24} & H_{34} & H_{44} \end{bmatrix} \begin{pmatrix} \epsilon_z \\ \kappa_x \\ \kappa_y \\ \kappa_z \end{pmatrix} \quad (2.1)$$

where the first matrix on right hand side of the equation is the 4x4 stiffness matrix, H_{11} is the longitudinal stiffness, H_{22} is the flapwise bending stiffness, H_{33} is the edgewise bending stiffness and H_{44} is the torsional stiffness. For an uncoupled cross-section the fibre angles in the layup are aligned with the longitudinal direction with the only non-zero terms in the leading diagonal, whereas the rest of the stiffness terms are zero. The stiffness terms in the diagonal relate the applied forces and moments directly with the observed displacement in the direction of the load. All the other off-diagonal terms essentially would couple this direct displacement produced by an applied load with displacements in directions other than that of the applied load. Additionally, the stiffness matrix is symmetric about the diagonal. Karaolis et al. calculated that for a mirrored lay-up in a symmetrical elliptical tube as seen in Figure 2.1, the stiffness term H_{24} is the only non-zero off-diagonal term. This stiffness term couples the bending deflections with the torsional deflections and is a measure of the induced twist per unit flapwise bending moment. In Equation 2.1 the column matrix on the right hand side of the equation represents the deflections where ϵ_z is the longitudinal strain, κ_x , κ_y and κ_z are the curvatures for flapwise bending, edgewise bending and torsion, respectively. The column matrix on the left hand side of the equation represents the loads with T_z as the axial force, M_x as the flapwise bending moment, M_y as the edgewise bending moment and M_z as the torsion.

Induced torsion

The total pitch angle of a blade section β is defined as the angle between the chord and the rotor plane and is given as the summation of the global blade pitch angle β_{pitch} , the fixed pre-twist of the section β_{twist} , the torsional deflection due to aerodynamic moments acting on the uncoupled blade δ_z , and the induced torsional

deformation θ . This relation is shown in Equation 2.2.

$$\beta(r) = \beta_{pitch} + \beta_{twist}(r) - \delta_z - \theta(r) \quad (2.2)$$

where r is the spanwise coordinate of the blade section. For positive values of the induced twist, the blade pitch is decreased resulting in an increased effective angle of attack and consequentially increased aerodynamic loads. This is termed as twist towards stall. Conversely, negative values of the induced twist will cause a decrease in the aerodynamic loads and is termed as twist towards feather. Thus, to achieve twist towards feather a negative value of the BTC stiffness term H_{24} is required. For the relationship between aerodynamic angle of attack and twist angle, and a detailed mathematical analysis, the reader is directed to Kooijman [26].

Blade coordinate System: The z-axis runs along the blade pitch axis and is positive from the root towards the tip. In the cross-sectional plane the x-axis is defined positive towards the leading edge and the y-axis is defines such that it is positive towards the suction side of the blade section. This coordinate system is employed in the HAWTOpt2 workflow. Other solvers that are interfaced, such as HAWC2 and BECAS, use different definitions of the blade coordinate system. For example, in HAWC2 the co-ordinate system for each cross-section is attached not at the blade pitch axis but at the half-chord point, however the positive directions of the axes are the same as in HAWTOpt2. The definitions in other coordinate systems are transformed to the coordinate system utilised by HAWTOpt2.

Coupling parameter

Lobitz and Veers [32] formulated a relation defining the amount of coupling that can be achieved in a blade. Applying the stress-strain relationship for bend-twist coupling, a 2x2 matrix system was derived consisting of a subset of the system shown in Equation 2.1. The following assumptions were made to facilitate building of the matrix system:

- Edgewise bending is considered small compared to flapwise bending, with insignificant amount of coupling.
- The coupling due to the axial force is considered negligible and ignored.

The flapwise bending terms and torsional terms including the moments and deflections, along with the coupling stiffness term K_{btc} were the only terms to be included in this formulation. The matrix system representing the stress-strain relation for bend-twist coupling is shown in Equation 2.3.

$$\begin{pmatrix} M_b \\ M_t \end{pmatrix} = \begin{bmatrix} K_b & -g \\ -g & K_t \end{bmatrix} \begin{pmatrix} \kappa_x \\ \kappa_z \end{pmatrix} \quad (2.3)$$

where K_b is the flapwise bending stiffness, K_t is the torsional stiffness, g is the bending-torsion coupling term, M_b is the flapwise bending moment and M_t is the torsional moment. For an uncoupled blade the value of g is zero. This matrix system is positive definite only if Equation 2.4 is satisfied. A positive definite matrix system is one in which the determinant of the stiffness matrix in Equation 2.3 is greater than zero.

$$g = \alpha \cdot \sqrt{K_b K_t}, \quad -1 < \alpha < 1 \quad (2.4)$$

where α represents the coupling parameter and gives the amount and type of coupling observed in the blade section. A negative α represents twist coupling towards feather, a positive value represents twist coupling towards stall while a zero value of the coupling parameter represents an uncoupled blade. Greater the magnitude of the coupling parameter, greater is the coupling between bending and torsion in the blade.

2.1.2 Multidisciplinary constrained optimisation

A key challenge in blade design is to compromise between aerodynamics (AEP) and the structure (mass and loads). As shown by Ning et al. [39] and Bottasso et al. [9], utilising multidisciplinary optimisation with the appropriate objective function that captures this trade-off can effectively realise the solution to this challenge. The robustness of the solution provided by the numerical optimisation algorithms will also depend on the structural, aeroelastic and geometric design and analysis tools that are linked in this optimisation. In this study the optimisation tool and workflow described by Zahle et al. [52] will be adopted. The objective function for this study will represent a trade-off between the annual energy production and the flapwise root bending loads. This objective cost function is shown in Equation 2.5.

$$C(\{x_p, x_s, x_{oper}\}, p) = f \cdot \frac{AEP(\{x_p, x_s, x_{oper}\}, p)}{AEP(\{0, 0, 0\}, p)} + (1 - f) \cdot \frac{M_x(\{0, 0, 0\}, p)}{M_x(\{x_p, x_s, x_{oper}\}, p)} \quad (2.5)$$

where C represents the cost function, AEP is the annual energy production, M_x is the flapwise blade root bending moment, f is the weight given to the aerodynamic and structural parameters that determines the trade-off, x_p are the collection of the blade planform design variables, x_s is the collection of the blade structural variables, x_{oper} is the collection of wind turbine control variables and p represents the variables that are kept constant. $AEP(\{0, 0, 0\}, p)$ and $M_x(\{0, 0, 0\}, p)$ represent the AEP and the flapwise root bending moment for the baseline uncoupled rotor, respectively. The cost function will also be subject to design constraints for the planform and structure which will be defined at a later stage in the thesis.

2.2 State-of-the-art

Techniques to achieve passive control of wind turbine blades have existed since the early days of wind energy research. These early systems focused on achieving power regulation through the use of mechanical means that reacted to the resulting forces on the wind turbine. Cheney and Speirings [13] achieved power regulation through a FRP hub, designed to be soft in torsion. On being actuated by the centrifugal action of a hub mounted pendulum, this would change the pitch of the stiff blade. Karaolis, Musgrove and Jeronimidis [24] first suggested the use of different types of twist couplings to regulate the power output by exploiting the anisotropic properties of FRP composite blades. Both flapwise and centrifugal loading could be utilised to twist the blades during operation of the wind turbine. The initiation of the bend-twist or the stretch-twist coupling would depend on the alignment of the fibres with respect to the spanwise axis of the blade. Karaolis et al. also showed that the level of twist coupling and stiffness reduction could be controlled by appropriately selecting the fibre orientation, thus resulting in a minimal disturbance to the beam stiffness properties from those obtained from symmetrical lay-ups used to inhibit

torsional deformations. They additionally suggested the use of an internally pressurised spar to actively control the spanwise distribution of the blade twist. Veers, Bir and Lobitz [48] in their review of aeroelastic tailoring mention that the concept of using a pressurised spar to actively control blade twist was dismissed by Corbet and Morgan [15] due to shortcomings in the manufacturing process with regard to repeatability.

The flapwise bending deformations of the blade can be coupled to produce torsional deformations either towards stall or towards feather. Early on, BTC was utilised to twist the blade towards stall which resulted in an increased angle of attack. This was targeted towards constant-speed and stall-controlled rotors. Kooijman [26] investigated the effects of BTC in enhancing power generation below rated wind speed for a constant-speed pitch-controlled rotor. The optimal power was found to be obtained when the inboard 40% of the span twisted towards the feather while the remaining 60% twisted towards the stall. Kooijman concluded that BTC gives the potential of an improvement in the annual energy production (AEP) by a few percentages with an increment of 10% in the starting torque of the constant-speed pitch-controlled rotor. He investigated the optimal spanwise bend-twist flexibility distribution through invoking the bend-twist coupling in the skin of the blade. Kooijman also managed to analytically confirm the theory formulated by Karalios et al. [24] on twist couplings in a monocoque cross-section. Lobitz, Veers and Migliore [35] studied the effects of BTC towards stall on AEP of a constant-speed stall-controlled rotor. By initiating stall, a decrease in loads during peak power production was observed. This allowed for an increase in rotor diameter keeping the maximum power at its design point. In a follow-up study, Lobitz and Laino [31] showed that BTC towards stall also substantially increased fatigue damage in turbulent wind and caused the blade to be prone to stall flutter. Lobitz and Veers [32] investigated the aeroelastic stability of bend-twist coupled blades towards stall and feather. They observed a destabilising of divergence for twisting towards stall. However, this could be controlled through the coupling factor α to prevent attainment of critical divergence speeds. Twisting towards feather showed a decreased fatigue damage by a factor of two. It also aeroelastically stabilised the blade for divergence and showed an absence of stall flutter. Classical flutter, however, is destabilised but could be controlled through the coupling factor α . Divergence onset by twisting towards stall was found to be significantly more critical than the classical flutter due to twisting towards feather [32].

Ong, Wang and Tsai [42] designed a bend-twist coupled D-spar to establish the real limits of coupling factor α that can be achieved for a composite FRP. Although Lobitz and Veers [32] mathematically derived the limits of the coupling factor α to be between -1 and 1, Ong, Wang and Tsai [42] showed that practically the maximum coupling limits were between -0.6 and 0.6. This was observed for carbon/epoxy laminate that has shown the highest coupling amongst known FRPs with a theoretical limit of α between 0.8 and -0.8. Furthermore, they concluded that the ply orientation, the laminate material, torsion warping and the proportional volume of anisotropy layers in the laminate had the greatest impact on the coupling coefficient.

As the wind turbine industry moved away from using constant speed stall controlled rotors towards using variable-speed pitch-controlled rotors, the research in BTC appropriately adapted to this change. Whereas early on, the research was primarily focused on achieving different degrees of passive power regulation, the advent of variable-speed pitch-controlled rotors made this requirement moot. Their control strategy enabled these rotors to operate close to their optimal aerodynamic design point for below rated wind speed. Above rated wind speed, the rated power

could be maintained by collectively pitching the blades. The research into BTC thus shifted focus from passive power regulation to passive load alleviation. Lobitz, Veers and Laino [33] investigated the load alleviation potential of blades designed to twist towards feather for a variable-speed rotor. The results showed a significant reduction in fatigue damage for a range of materials for different wind loadings. The blades were pre-twisted such that optimum aerodynamic twist distribution would ensue at rated power. This pre-twisting prevented any deterioration of the power captured compared to the uncoupled baseline rotor. Lobitz and Veers [34] studied the effect of BTC towards feather for variable-speed pitch-controlled rotors noting a decrease in fatigue damage over all wind speeds without a reduction in average power. Maximum loads were observed to decrease as well. Furthermore, the authors generalise that significant reductions in fatigue damage are produced when the blades operate in the linear part of the aerodynamic profile. The reductions in fatigue damage were found to be the greatest in the variable-speed pitch-controlled rotors when compared with variable-speed stall-controlled and constant-speed stall-controlled rotors for the same amount of coupling. This was mainly attributed to the ability of the variable-speed pitch-controlled rotors to operate in the linear aerodynamic range over all wind speeds. Ashwill [1], discussed the results obtained from testing of a 9m blade consisting of unidirectional carbon fibres in the skin with a fibre orientation of 20° to the blade pitch axis. The blade was designed to twist towards feather. Design constraints to maintain flapwise strength and maximum tip deflection were applied. The coupling was implemented onward of 25% blade spanwise location. The results showed that using off-axis carbon in the skin will induce extra twist and reduce fatigue damage [1].

Capallero [11] investigated the design limits of bend-twist coupling and load alleviation using the UpWind reference turbine [16]. He oriented the fibres in the spar caps to initiate BTC and increased spar cap thickness to maintain the maximum tip displacement and offset bending stiffness reduction. The investigation concluded that design limits are imposed on the BTC by the anisotropic properties of the material, blade design, amount of asymmetric materials and blade geometry. There is an interdependency observed between blade bending stiffness and the degree of coupling. This constrains the amount of coupling in the blade. Maximising the coupling would cause the tip deflections to exceed the maximum allowable limit due to a decrease in bending stiffness and furthermore it would reduce the AEP. In lieu of these design constraints and couplings, Capallero suggests using small fibre orientations which cause sufficient coupling to decrease loads, prevent the use of extra material to improve the bending stiffness and produce nearly the same AEP as the uncoupled baseline rotor.

The various interdependencies that exist among the different design variables make wind turbine design a complex problem. Numerous considerations of the design variables have to be taken into account to reach a acceptable compromise between the desired performance and cost. Bottasso, Campagnolo and Croce [9], stating the importance of a MDAO approach emphasise that "an integrated multidisciplinary optimisation of wind turbine rotors addresses a much more complex problem that considers the aerodynamic shape optimisation, the evaluation of all relevant load conditions (which in turn requires the definition of appropriate control laws), the optimal sizing of the structural members under the effects of the loads, considering the mutual couplings between the various sub-disciplines and simultaneously accounting for the presence of a number of design constraints of various nature." They consider the objective function of the multidisciplinary optimisation of a wind turbine as a compromise between maximising the AEP and minimising

the weight of the rotor. Ning, Damiani and Moriarty [39] argue that optimising a combined aerodynamic/structural objective function results in a better performing design over a sequentially optimising aerodynamic and structural objectives or just maximising the aerodynamic objective of AEP. They reach this conclusion by comparing the objective functions comprising maximising AEP, minimising ratio of turbine mass to AEP and minimising cost of energy. Zahle et al. [52] demonstrated the optimisation of the DTU 10MW reference wind turbine by maximising the AEP with the loads envelope of the reference turbine constrained to their original values. This was achieved by integrating the time domain aero-elastic solver HAWC2 and the cross-section analysis tool BECAS with an in-house MDAO tool HAWTOpt2. The optimisation resulted in a 11.1% increment in the AEP accompanied by an increase in blade length of 8m. The optimised blade also produced a shear-twist coupling that caused a decrease of flapwise fatigue damage when compared to the reference case. Zahle et al. state that this aeroelastic tailoring was achieved by the optimiser without any prior knowledge being included in the optimisation. The study proposed in this paper intends to utilise the same MDAO workflow as used by Zahle et al. [52]. However, unlike the study by Zahle et al., a combined aerodynamic and structural objective function will be the subject of the optimisation as suggested by Ning, Damiani and Moriarty [39] with the inclusion of bend-twist coupling in the structure.

Chapter 3

Aerodynamics, Structure and Control

A description of the preliminary aerodynamic and structural design of the proposed wind turbine rotor has been provided in this chapter. This initial design is limited in characteristics such as rotor size, hub height and wind climate by the rules defined in the Small Wind Turbine competition hosted by the NHL University of Applied Sciences [22]. Section 3.1 introduces the regulations of the competition that are relevant to the design of the rotor. This is followed by section 3.2 that focuses on the design of the planform of the blade including the twist distribution to obtain an optimal performance. It also highlights the decisions that led to the chosen airfoils for the blade. Section 3.3 portrays the internal structure of the blade, including the selected composite materials and the laminate composition. The DTU Wind Energy basic controller is then tuned for the preliminary design in section 3.4 and will facilitate successful execution of the aero-servo-elastic simulations in the remainder of the report.

3.1 Competition regulation

The Small Wind Turbine Design Contest is an annual competition organised by NHL University of Applied Sciences in the Netherlands. The entries to the competition are assessed based on an evaluation criteria that judge in three aspects, namely the design report, manufacturing of the turbine and its performance in wind tunnel tests. For more details on the competition the reader is directed to their official website [22]. The rules that have a direct effect on the aerodynamic and planform design are listed below.

- The rotor swept area is limited to a maximum of 2m^2 .
- The hub height of the rotor should not exceed 3m including a mounting pile.
- The rotor is to be designed for a low wind speed climate given by an average wind speed $V_{avg}=4$ m/s, with the Weibull scale parameter $A=4.5$ m/s and shape parameter $k=2$, in standard atmospheric conditions.

Other miscellaneous rules that are important for the design of the whole turbine but do not directly affect the rotor design are listed [22], [47]:

- The turbine must be designed for automatic operation and achieve the rated power output with a DC output voltage of 24-42 V with a limit of 60V (Important for generator design).

- All control and safety functions are to be integrated within the interface boundaries.
- The rotational speed and power shall never exceed the limits for all load cases.
- The turbine shall have a mechanism for a manual emergency stop and blocking of the rotor.
- The turbine shall be provided with an independent superior protection system that automatically protects the turbine from single failures or faults in any component within the control and protection system, and also from faults in the load connection.

3.2 Aerodynamic design

This section is divided into two main parts. First, subsection 3.2.1 deals briefly with the choice of the airfoil, describing the factors that led to this choice while presenting important characteristics and ending with a description of the planform. The selection of the rotor speed, airfoils and the final aerodynamic design explained here are according to the author's understanding of the process through consultations with design reports and project supervisors of the previous iterations of the Small Wind Turbine project. It has been the aim to discuss the motivations behind key decisions that have played an important role in the finalising the current aerodynamic rotor design. This has been done to avoid repetitions from previous reports. For a more detailed analysis that led to the choice of the current airfoil and blade geometry, the reader is directed to read the master thesis of Bernitt [30].

This section is followed by subsection 3.2.2, where the resulting rotor is analysed with a BEM (Blade Element Momentum) aerodynamic model using the linear aeroelastic code HawcStab2 [21].

3.2.1 Airfoil and plaform

The airfoil and the resulting planform was chosen in the previous iterations of the small wind turbine project, and has been carried forward this year. The design itself follows the aerodynamic design philosophy laid down by Bak [2] and the reader is directed to the same for an in-depth explanation about the procedure on topics such as blade element momentum theory (BEM) and one-point aerodynamic design process. As a design prerequisite, and keeping with the times, a variable speed pitch-control strategy was selected for the control of the rotor. In this control strategy the rotor would operate at the optimal aerodynamic design points of the power producing blade sections, below the rated wind speed extracting the highest possible power from the oncoming wind in the swept area. This would be made possible by varying the rotor speed Ω to get an optimum performance. For wind speeds equal to and greater than the rated wind-speed V_{rated} the power is limited to its rated value by pitching the blades such that the turbine gradually moves away from the aerodynamically optimal point of operation.

The restriction of 2m^2 on the rotor area placed by the competition guidelines mentioned in section 3.1, led to a diameter of 1.58m with a blade length of 0.75m and a hub length of 0.04m. An important parameter in determining the choice of airfoil is the tip-speed ratio λ of the rotor. It is defined as the ratio between the tangential

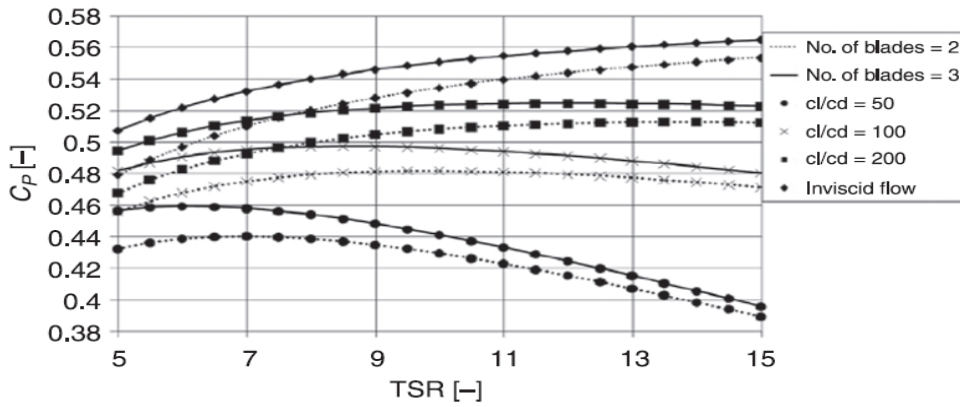


FIGURE 3.1: Power coefficient with varying tip-speed ratios for different airfoil efficiencies [2]

velocity of the blade tip to the oncoming wind-speed, as shown in Equation 3.1:

$$\lambda = \frac{\Omega R}{V_0} \quad (3.1)$$

where Ω is the rotor speed in rad/s and V_0 is the speed of the oncoming wind in m/s. Since the tip-speed ratio is directly proportional to the radius of the rotor, a small rotor would require high values of the rotor speed for a high value of the tip-speed ratio. As the prescribed wind climate has an average wind speed of 4m/s, a low cut-in velocity V_{cut-in} is desirable in order to have a good annual energy production AEP . A high cut-in rotor speed Ω_{cut-in} is not desirable due to difficulties faced in the start-up of a wind turbine from standstill. Taking these arguments into account, a low design tip-speed ratio λ_{design} of 5 was chosen for the rotor. The rated wind speed of $V_{rated}=10$ m/s was chosen using the rule of thumb that the rated wind speed at a site would be 6m/s higher than the mean wind speed [2]. Bak [3] conducted an investigation into the effect of aerodynamic design parameters of airfoils, such as the lift-to-drag ratio Cl/Cd , on the power coefficient of wind turbine rotors. The investigation revealed a clear dependence of power coefficient C_P and tip-speed ratio λ on airfoil efficiency Cl/Cd . This dependence can be witnessed in Figure 3.1. It was also recommended that for a rotor diameter of $D=1.75$ m a design tip-speed ratio λ_{design} of 5.5 should be chosen, corresponding to a maximum airfoil efficiency (Cl/Cd) of 50. This recommendation played an important role in the selection of the airfoil family chosen for detailed analysis for the SWT 500W's aerodynamic design.

With selection of the rotor speed range $\Omega_{cut-in}, \Omega_{cut-out}$ and rough guesses of the chord at the root and tip, a Reynolds number (Re) range of 75,000-200,000 was obtained. The SD7032, Clark-Y, E387, SG6043 and SD7003 airfoils were investigated as they all have a maximum airfoil efficiency of around 50 for Re range of 100,000-200,000. SD7032 was chosen as the main airfoil due to a steady performance with similar lift curve across the range of Reynolds number, and a higher airfoil efficiency compared to the other airfoils. SD7032 is an asymmetric, low Reynolds number airfoil with a maximum thickness of 10% and a maximum camber of 3.4% at 26.6% and 45.1% chord length respectively, measured from the leading edge [45]. The profile of the Selig/Donovan SD7032 airfoil with the points of maximum relative thickness and maximum camber is shown in Figure 3.2. A comparison of lift curves for the SD7032 and SG6043 are shown in Figure 3.3.

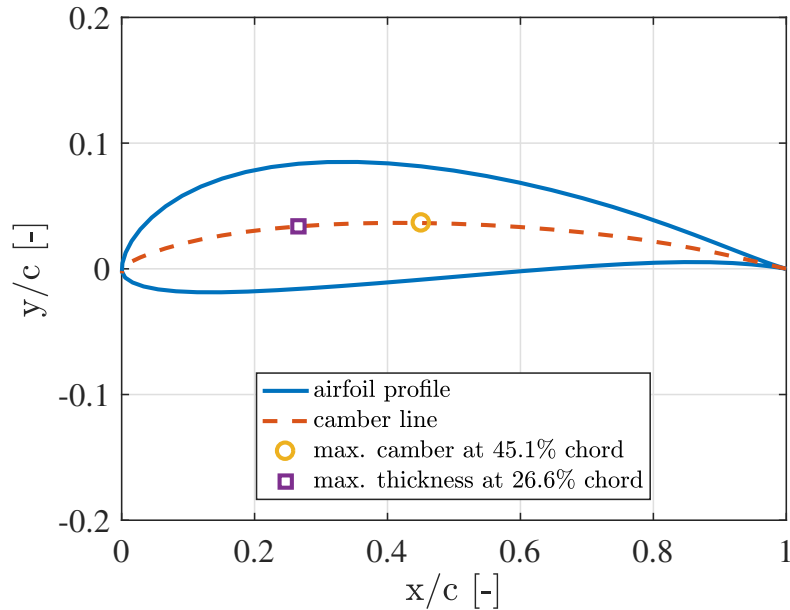


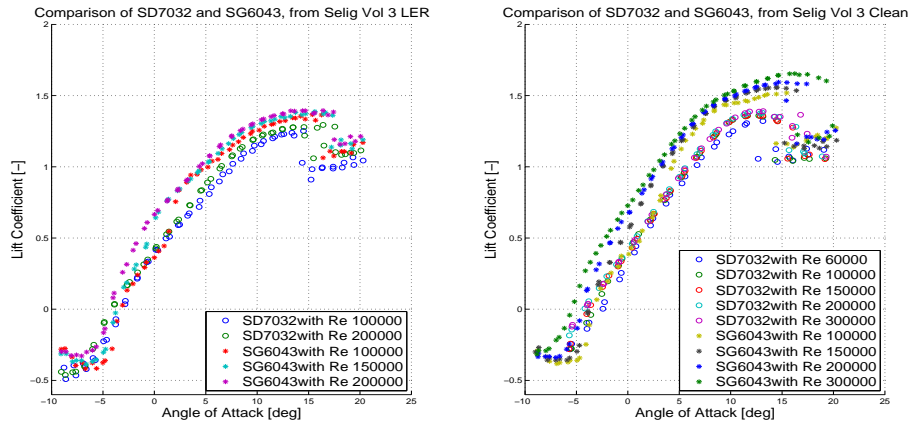
FIGURE 3.2: SD-7032 airfoil profile with 10% relative thickness

The final airfoil chord and thickness distribution was arrived at using a BEM method and the steps defined by Bak [2]. After selecting the chord distribution the BEM was used to find the twist angles at which the blade geometry would produce the highest power coefficients at the design angle of attack. The SD7032 with a relative thickness of 10% was the only airfoil used throughout the blade. The relative thickness distribution was interpolated between the circular root and the 0.23m point on the blade span. Beyond this point the blade has a constant relative thickness of 10%. The aerodynamic coefficients (C_l , C_d , C_m) were also linearly interpolated between the circular root and the SD7032 airfoil. The distance of the pitch axis from the leading edge was taken as 35% of the chord length for the SD7032 airfoil and 50% of the chord length for the circular root. It was interpolated between the value at the circular root and the 0.23m point on the blade span. The resulting blade geometry and planform is shown in Figure 3.4.

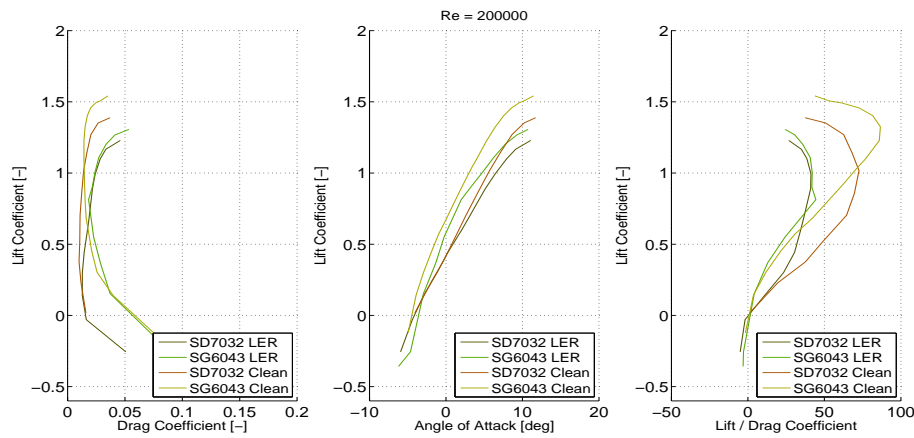
3.2.2 Rotor performance analysis

The rotor performance analysis is carried out using the linear aeroelastic code HAWCStab2 [21]. In this code a nonlinear finite element beam model is linearised and coupled with an unsteady blade element momentum (BEM) aerodynamic model considering induction from the shed vorticity, dynamic stall and dynamic inflow. HAWCStab2 is utilised to gauge the aerodynamic performance and predict steady state loads due to two main reasons. First, HAWCStab2 uses the same aerodynamic models as in the time domain aeroelastic code HAWC2. This removes the differences in prediction of the aerodynamic loads and produced power between the steady state model and HAWC2, enabling the use of loads predicted from HAWCStab2 to determine the controller tuning parameters and aerodynamic gain scheduling constants. Second, HAWCStab2 undergoes constant validation due to its widespread usage ensuring accuracy and repeatability. On the other hand, a new steady state BEM code would take time to obtain the same levels of reliability.

The structure analysed is rigid as the final structure of the blade was still not finalised at this point. It was also predicted that due to the small rotor radius, the



(A) Lift curve comparison for Re range 100000- 200000



(B) Lift curve comparison for Re=200000

FIGURE 3.3: Comparison of lift curves between SD7032 and SG6043 airfoils [45]

baseline blade devoid of material coupling would be stiff and the resulting deformations would not sufficiently affect the aerodynamic performance. Additionally, HAWCStab2 lacks the functionality to incorporate material coupling in its structural analysis limiting its usage to the evaluating the steady state rotor performance for the course of this study. The model input parameters for HAWCstab2 are shown in Table 3.1.

TABLE 3.1: HAWCStab2 aerodynamic model input

Model parameter	Value
Wake induction	On
Tip loss	Prandtl
Wind shear: Power law constant	0
Dynamic stall model	MHH-Beddoes [19]

The blade geometry described in subsection 3.2.1 is analysed over the operational range of wind speeds from 3 m/s to 25 m/s for a rotor-speed range of 181.40 rpm to 604.40 rpm. The rated electric power has been selected as 500W at a wind speed of 10 m/s. The aerodynamic performance of the blade geometry is shown in Figure 3.5.

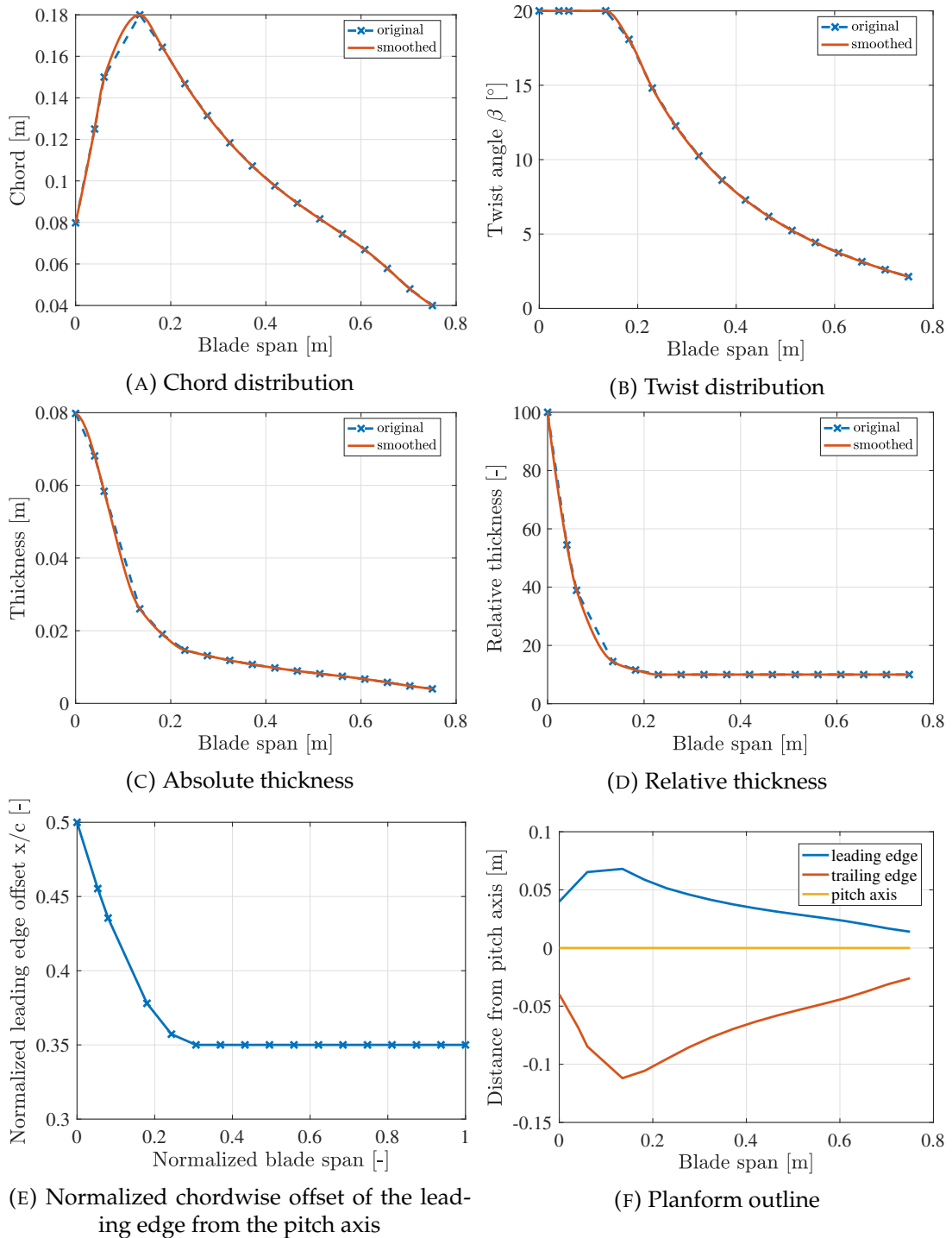


FIGURE 3.4: Blade planform properties

The current blade profile registers an optimal power coefficient $C_{P_{opt}} = 0.45$, thrust coefficient $C_{T_{opt}} = 0.80$ and optimal tip-speed ratio $\lambda_{opt} = 5$ in the partial load region. It can be seen from the power curve that the rated aerodynamic power is being capped at $P_{rated-aero} = 526W$ in order to accommodate the electrical losses of the generator. The generator being used in the final wind turbine is a direct drive permanent magnet generator with a theoretical efficiency of 95%. Thus, the electrical rated power output will be 500W.

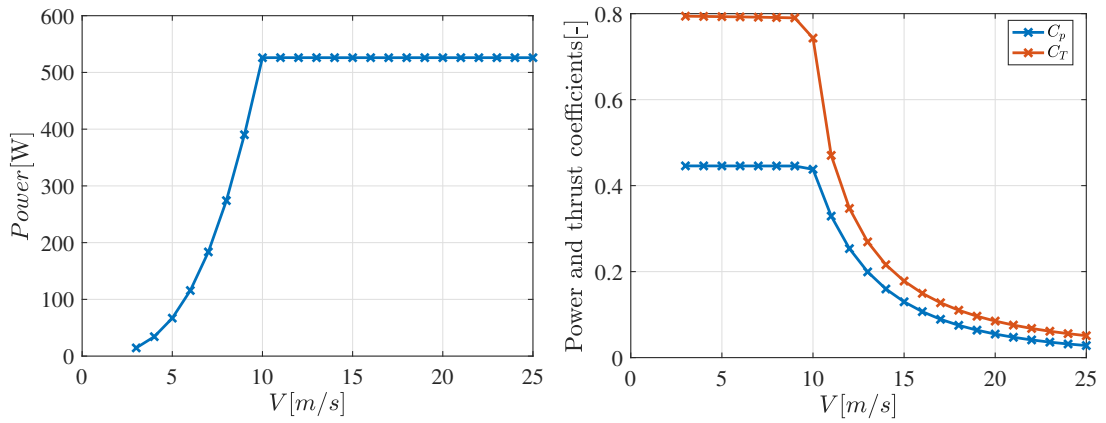
The aerodynamic performance of the spanwise blade sections for the wind speed of 8 m/s in the partial load region is shown through plots in Figure 3.6. It is seen that the angle of attack over the span attains its design value of 5° slightly above the 0.2 m blade length. From this point and onwards the lift to drag ratio and the lift coefficient are also seen to attain their design values of 49 and 0.9 respectively. This point coincides with the use of the SD-7032 airfoil geometry as seen in Figure 3.4. The relative thickness of the blade sections increase from around 10 % at the 0.2 m blade length mark to 100% at the root. Thicker airfoils are generally less aerodynamically efficient than their thinner counterparts [2]. Furthermore, from the velocity triangle the flow angle ϕ is seen to increase closer to the root. This increase in the flow angle and the limit on the maximum twist angle of 20° set by manufacturing constraints causes an increase in the angle of attack experienced by these sections, as witnessed in Figure 3.6a. Such an increase in the angle of attack results in the airfoil operating in the stall region. A high enough twist angle could restrict the performance to the linear region of the lift curve but this isn't possible due to the manufacturing limits placed on the twist angle. Although new manufacturing techniques provide the means to produce increasingly complex blade geometries, the associated costs and challenges in design analysis prove to be important factors in determining the simplifications for manufacturing reasons [44]. The operation in the stall region is accompanied by a drop in the lift coefficient and an increase in the drag experienced by the blade sections, as seen in Figure 3.6b and Figure 3.6c. This causes a decrease in the power and thrust coefficients, with a negative power coefficient very close to the root due to very high relative thicknesses. The power and thrust coefficient variations over the span are seen in Figure 3.6d.

3.3 Structural design

The baseline blade design is finalised in this section by defining the structural properties of the blade. First, the composite materials to be potentially used in the blade are described and their structural properties are analysed. Next, the blade internal structure and the composite layup are defined, including visualisations of their spanwise mass and stiffness distributions.

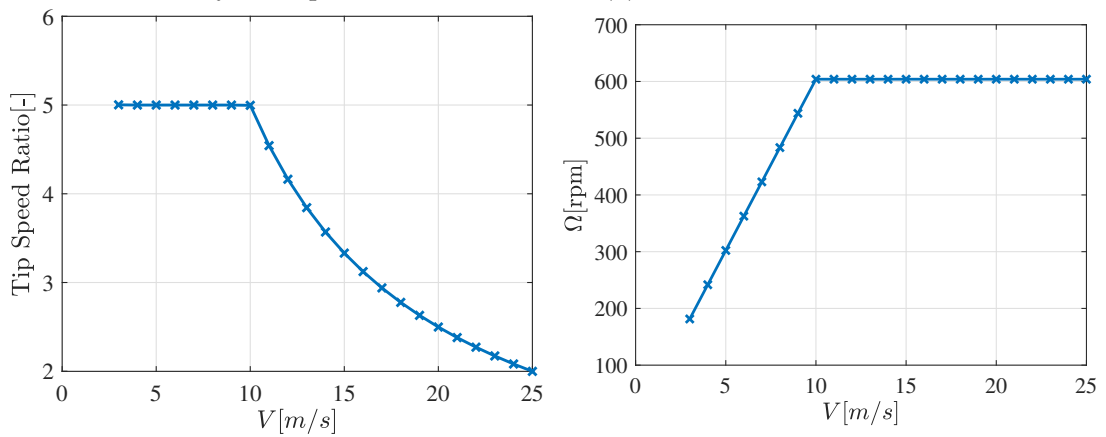
3.3.1 Material properties

Both glass and carbon fibre reinforced composites are considered for the baseline blade devoid of material coupling, and also for its material coupled versions. The choice of the material to be used in the final blade design would depend on the bending-torsion coupling characteristics offered by the blade and thus is deferred to a later stage when these properties are analysed through parametric studies. The choice will become evident in chapter 4.



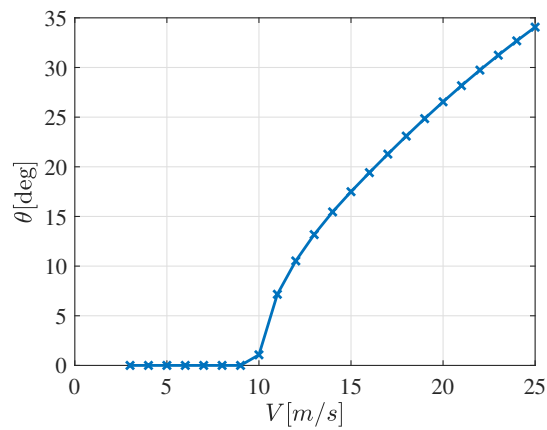
(A) Aerodynamic power curve

(B) Power and thrust coefficient curves



(C) Tip-speed ratio curve

(D) Rotor speed curve



(E) Aerodynamic pitch curve

FIGURE 3.5: Steady state aerodynamic performance of rotor from HawcStab2

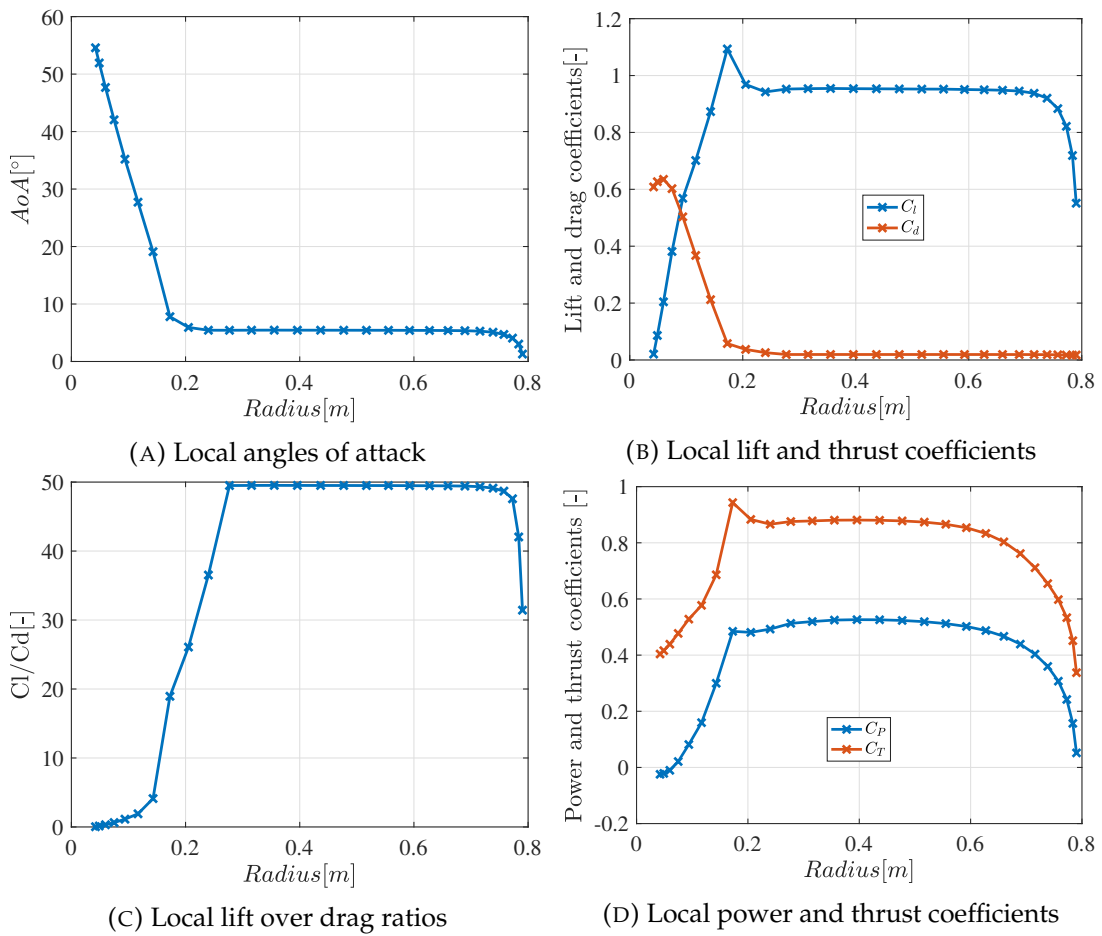


FIGURE 3.6: Steady state aerodynamic performance of blade at wind speed of 8m/s

The mechanical properties of the unidirectional glass-epoxy and carbon-epoxy laminae are obtained by using simple micromechanics equations for composites found in Chamis[12] and repeated here for convenience.

The Young's modulus of the laminae in the direction of the fibres E_1 and in the direction transverse to the fibres E_2 are calculated using Equation 3.2 and Equation 3.3 respectively.

$$E_1 = E_{f1}V_f + E_mV_m \quad (3.2)$$

$$E_2 = \frac{E_m}{1 - \sqrt{V_f} \left(1 - \frac{E_m}{E_{f2}}\right)} \quad (3.3)$$

where E_{f1} and E_{f2} are the longitudinal and transverse Young's moduli of the fibres being used in the laminate, E_m is the Young's modulus of the matrix which in this case is epoxy resin, V_m is the volume fraction of the epoxy resin matrix and V_f is the volume fraction of the fibres in the laminate.

The in-plane shear modulus G_{12} and out-of-plane shear modulus G_{23} of the unidirectional laminae are obtained using Equation 3.4 and Equation 3.5.

$$G_{12} = \frac{G_m}{1 - \sqrt{V_f} \left(1 - \frac{G_m}{G_{f12}}\right)} \quad (3.4)$$

$$G_{23} = \frac{G_m}{1 - \sqrt{V_f} \left(1 - \frac{G_m}{G_{f23}}\right)} \quad (3.5)$$

where G_{f12} and G_{f23} are the in-plane and out-of-plane shear moduli of the fibres and G_m is the shear modulus of the epoxy resin matrix.

The in-plane ν_{12} and out-of-plane ν_{23} Poisson's ratios are given by Equation 3.6 and Equation 3.7 respectively.

$$\nu_{12} = \nu_{f12}V_f + \nu_m(1 - V_f) \quad (3.6)$$

$$\nu_{23} = \frac{E_2}{2G_{23}} - 1 \quad (3.7)$$

where ν_m and ν_{f12} are the Poisson's ratios of the epoxy resin matrix and fibres, respectively.

Due to symmetry the mechanical properties of the laminae in the second direction transverse to the fibres are given, as shown in Equation 3.8, Equation 3.9 and Equation 3.10.

$$E_3 = E_2 \quad (3.8)$$

$$G_{13} = G_{12} \quad (3.9)$$

$$\nu_{13} = \nu_{12} \quad (3.10)$$

The density of the laminate composed of the fibres and matrix is obtained from Equation 3.11.

$$\rho = \rho_f V_f + \rho_m (1 - V_f) \quad (3.11)$$

where ρ_f and ρ_m are the mass densities of the chosen fibre and epoxy matrix.

The mechanical properties of the glass and carbon fibres considered in this study and the epoxy resin matrix are shown in Table 3.2 and Table 3.3. The mechanical properties of the glass-epoxy and carbon-epoxy laminae determined using Equation 3.3 to Equation 3.10 are presented in Table 3.4.

The shear modulus of the matrix and, in-plane and out-of-plane shear moduli of the fibres are calculated from their respective Young's moduli and Poisson's ratios as shown in Equation 3.12, Equation 3.13 and Equation 3.14.

$$G_m = \frac{E_m}{2(1 + \nu_m)} \quad (3.12)$$

$$G_{f12} = \frac{E_{f1}}{2(1 + \nu_{f12})} \quad (3.13)$$

$$G_{f23} = G_{f12} \quad (3.14)$$

TABLE 3.2: Mechanical properties of glass and carbon fibres used in the laminae [30], [4]

Property	Carbon	Glass
Fibre Type	Tenax UTS50 F13 12K [30]	E-Glass [4]
Longitudinal Young's modulus E_{f1} [GPa]	243	75
Transverse Young's modulus E_{f2} [GPa]	243	75
Poisson's ratio ν_{f12} [-]	1.6	0.2
In-plane shear modulus G_{f12} [GPa]	119	31.25
Transverse shear modulus G_{f23} [GPa]	119	31.25
Density ρ_f [kg/m ³]	1799	2550

TABLE 3.3: Mechanical properties of epoxy matrix used in the laminae

Property	Value
Young's modulus E_m [GPa]	4.0
Poisson's ratio ν_m [-]	0.35
Shear modulus G_m [GPa]	1.4815
Density ρ_m [kg/m ³]	1140

TABLE 3.4: Mechanical properties of the glass-epoxy and carbon-epoxy laminates

Property	Carbon	Glass
Volume fraction V_f	0.60	0.55
Young's modulus in fibre direction E_1 [GPa]	147	43.05
Transverse Young's modulus E_2 [GPa]	17	13.42
In-plane Poisson's ratio ν_{12} [-]	0.15	0.27
Out-of-plane Poisson's ratio ν_{23} [-]	0.42	0.33
In-plane shear modulus G_{12} [GPa]	6	5.05
Out-of-plane shear modulus G_{23} [GPa]	6	5.05
Density ρ_f [kg/m ³]	1535	1915.5

3.3.2 Internal structure and layup

First, the internal structure of the blade is described. As mentioned in subsection 3.3.1 two reference blades will be initially generated with one composed of glass-epoxy laminae while the other of carbon-epoxy laminae. In order to maintain simplicity in the structure, the blades will be made up entirely of unidirectional plies. Additionally, this will facilitate ease in the identification of the material most receptive to bend-twist coupling on small wind turbine blades.

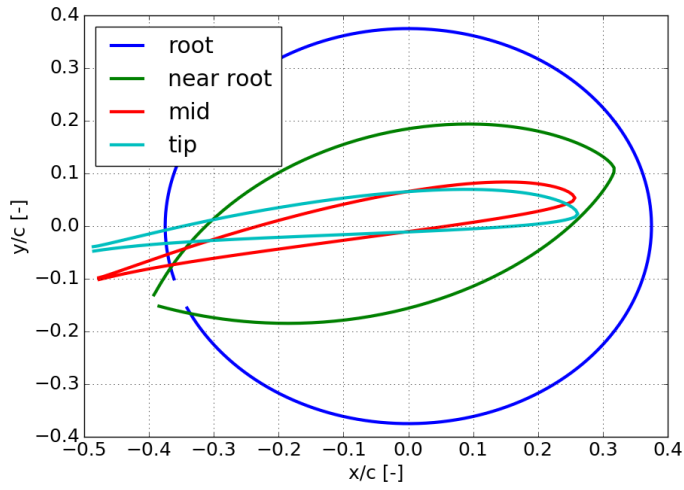
The small size of the blade would restrict the magnitude of aerodynamic forces and moments being generated. Additionally, high stiffness of the blade in the flapwise or the torsional directions would impede the bending-torsion coupling which relies on the magnitude of flapwise and torsional deflections to generate load alleviation. Thus, in order to make the blade as flexible as possible a few key features are implemented in the internal structure:

- A spar has been excluded from the blade design. Thus, the blade is only made up of skin with no structures to provide additional rigidity.
- The thickness of the skin is uniformly maintained at the minimum manufacturing limit of 1mm throughout the blade.
- Simplicity and stiffness reduction is enforced by not including a sandwich material.
- One layer of composite laminate is used throughout the blade.

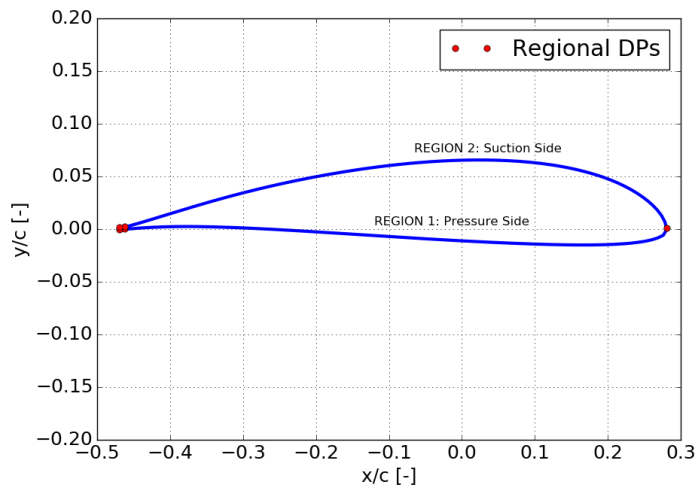
For the reference blades the fibres are aligned along the longitudinal axis of the blade starting from the root and ending at the tip.

In the Fused-Wind framework [40] the internal structure of the blade is created through cross section definitions. The blade is divided into a specified number of structural sections. In each of these sections the composite layup is defined in a cross sectional sense. A cross section is divided into multiple regions with each region consisting of its own stack of composite laminae. The regions are defined by specifying the locations of regional division points (DPs) along the cross section. In the present study, the 0.75m long blade is divided into 17 structural spanwise sections, with each cross-section further divided into 4 regions. The cross section from mid-span of the current blade geometry divided into regions by division points can be seen in Figure 3.7b. There are two main regions separated by a DP at the leading edge of the profile. Region 1 denotes the pressure side surface exposed to the relative wind, whereas region 2 represents the suction side surface of the profile. Two regions near the trailing edge cover around 0.01% of the total cross sectional circumference. Their role is to act as a buffer between the two main pressure side and suction side regions, and the trailing edge to prevent meshing discontinuities. The blade cross sectional profiles at different representative spanwise locations with their respective pre-twist angles are shown in Figure 3.7a. The number of laminate layers, the order of materials in the stack, thickness of the material and fibre layup angle are defined for each region. The mechanical properties of the laminae in the stack are defined and calculated using the approach shown in subsection 3.3.1. The composite layup of the two regions in terms of uniax, biax, triax and core materials used in the laminate is shown in Figure 3.8. It is seen that the blade only consists of unidirectional fibres with a laminate thickness of 1 mm.

The geometry of the blade is generated using the PGL library, which is a collection of classes and methods developed in the FUSED-Wind framework. This library



(A) Profiles at various representative span locations



(B) Profile divided into regions by DPs

FIGURE 3.7: Blade cross section profiles

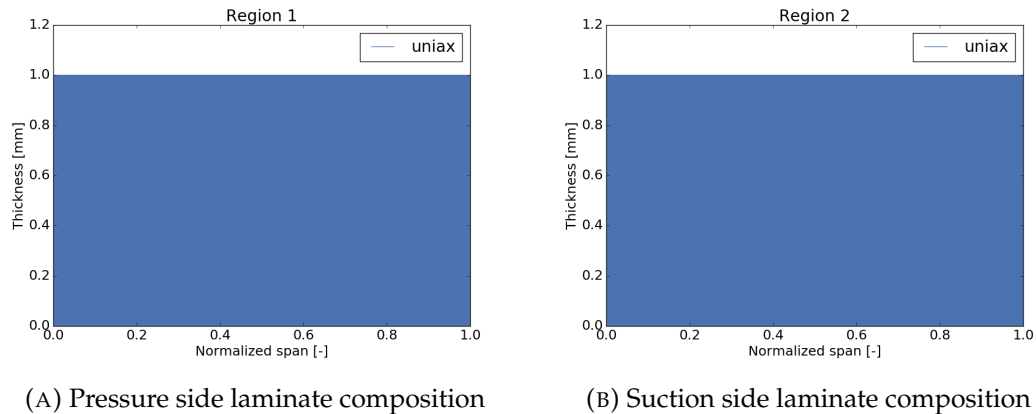


FIGURE 3.8: Laminate composition over span

consists of methods defining different curve types, surface mesh to construct a surface and interpolated airfoil shapes from the airfoil family used in at key regions in a blade. In combination with the information of the internal structure, this data is provided to the cross-sectional analysis tool BECAS and the relevant structural data with stiffness and mass distributions, and the cross sectional locations of the shear centre, centre of gravity and elastic centre along the structural spanwise locations are obtained. The flapwise, edgewise and torsional stiffness distributions of the reference blades composed of both glass-epoxy and carbon-epoxy composites are shown in Figure 3.9b, Figure 3.9c and Figure 3.9d respectively. The stiffness distributions were plotted on a semi-log scale with a logarithmic y-axis and a linear x-axis in order to clearly represent the differences between the glass and carbon fibre blades. It can be seen that generally the carbon fibre blade has a higher flapwise, edgewise and torsional stiffness than the glass fibre blade. However, this difference is low in the torsional stiffness with both blades having similar values. Both, the carbon and glass fibre blades show a decrease in the stiffness values from the root towards the tip. The decrease in stiffness over span mirrors the decrease in the chord and thickness values of the cross-section over the span as seen in Figure 3.4a and Figure 3.4c, pointing towards a dependence on the chord and thickness values of the blade sections. The mass distribution over span is shown in Figure 3.9a. The carbon fibre blade has a lower mass compared to the glass fibre blade owing to the lower mass density of the composite ply. The mass is also seen to decrease with a reduction in the thickness and the chord of the airfoil profiles along the span. For a uniform spanwise laminate thickness and mass density, a lower chord and absolute thickness of the blade section would result in the composite material occupying a smaller volume of space, reducing the mass and making the blade more flexible. Thus, blade profiles with low values of relative thickness are desired.

3.4 Controller tuning

The DTU Wind Energy basic controller [20] has been tuned for the 500W turbine with uncoupled rotor blades of carbon FRP. Wind shear and tower shadow effects have not been considered. Controller testing is done by using 1 m/s wind steps of 30s time intervals from 3m/s to 25m/s. The behaviour exhibited by the controller has been shown in subsection 3.4.1.

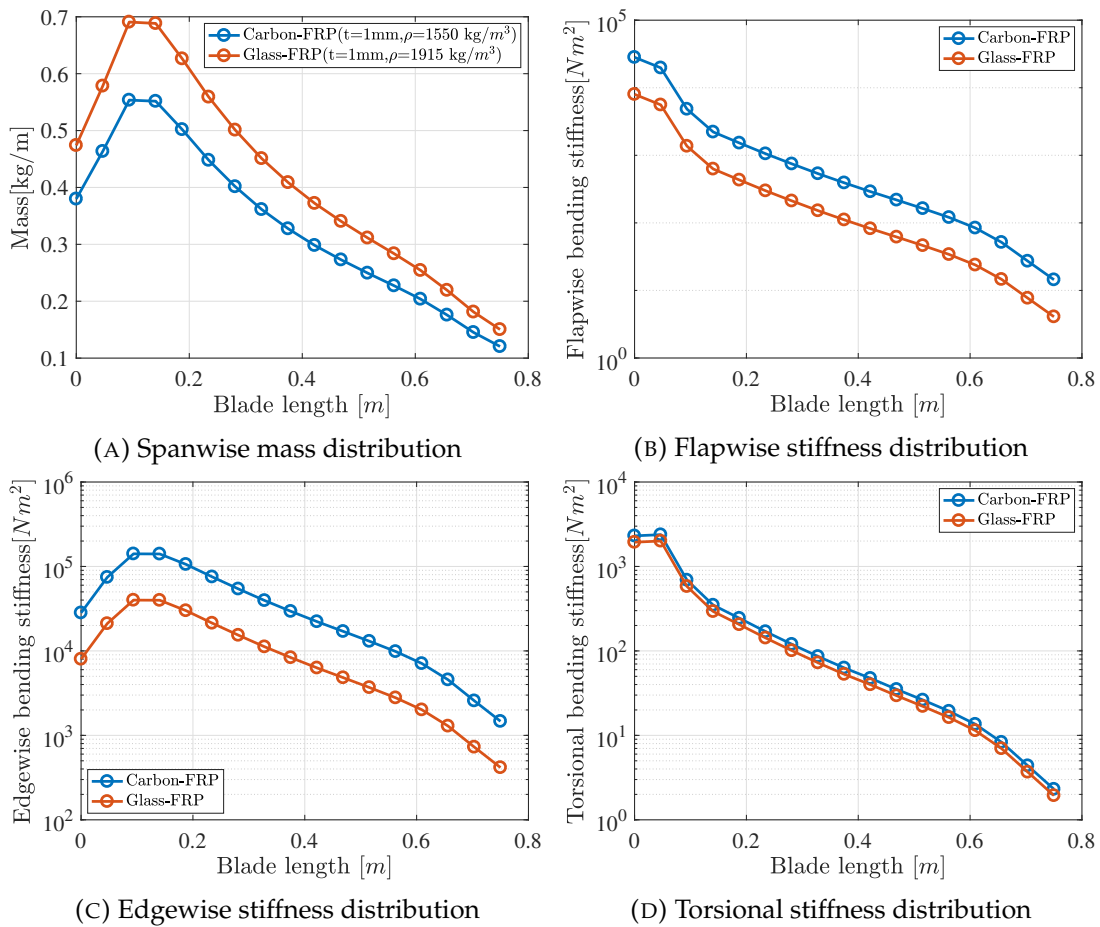


FIGURE 3.9: Structural data of blade along span

The constant C_p tracking factor K , required for control in region 1, is calculated based on a constant C_p of 0.453 and a constant tip-speed ratio of 5. Both proportional gain and integral gain of the torque controller for region 2 and pitch controller for region 3 are calculated according to desired natural frequency and damping ratio of the closed-loop drive train eigenvalue. The aerodynamic gain scheduling constants K_1 and K_2 of the pitch controller are determined by second order polynomial fitting curve. Constant torque control is used for the generator in Region 3 which gives higher damping to the closed loop control system. The values chosen for the parameters are shown below in Table 3.5.

The controller is initially tuned using a known tuning method followed by finer tuning using pole placement. The initial tuning is carried out, first for the partial load region and then for the full load region. The integral gain is set to zero and the proportional gain is increased to find its critical value. At the critical value of the proportional gain the response of rotor speed Ω oscillates and does not decay to the new steady state. The Ziegler-Nichols method is then applied to obtain the proportional and integral gains, utilising the critical proportional gain and the time period of the oscillations.

The initial tuning gives an approximate value of the pole natural frequency ω on fixing the damping frequency ζ to the recommended values of 0.6 or 0.7. This is calculated by using the relation between proportional gain K_p and integral gain K_i as shown in Equation 3.15, which has been derived using the gain equations shown in section 3.4. The remainder of the tuning is performed by observing the response to the stepwise input of wind speeds from 4 m/s to 25 m/s for a step interval of 30s. The response to the final configuration is shown in subsection 3.4.1.

$$K_i = \frac{\omega}{2\zeta} \cdot K_p \quad (3.15)$$

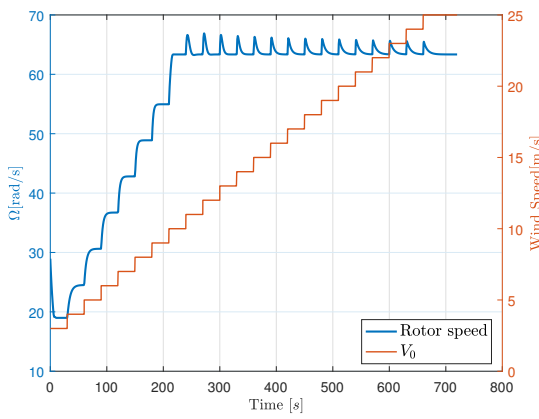
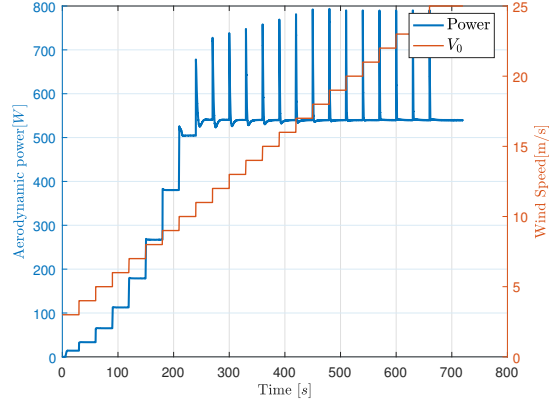
where Ω is the natural frequency of the rigid body rotation pole and ζ is the damping ratio of the rigid body rotation pole.

TABLE 3.5: Overview of control parameters

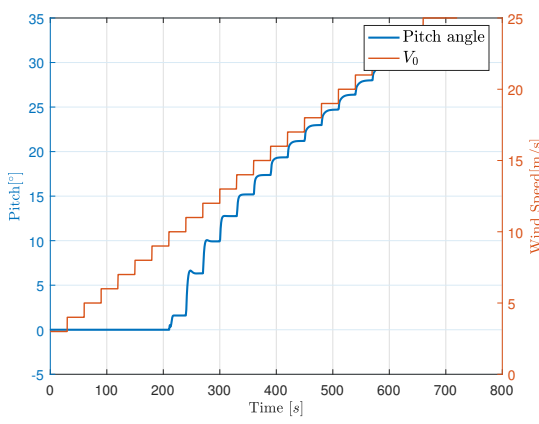
C_p track	Region 2: Torque control				Region 3: Pitch control					
	K_{Pg} [$\frac{Nm}{(rad/s)}$]	K_{Ig} [$\frac{Nm}{rad}$]	ω_g [Hz]	ζ_g [-]	K_{Pp} [$\frac{Nm}{(rad/s)}$]	K_{Ip} [$\frac{Nm}{rad}$]	ω_p [Hz]	ζ_p [Hz]	K_1 [-]	K_2 [-]
0.213E-02	1.44	1.29	0.1	0.7	0.168E-01	0.7180E-02	0.095	0.7	7.69	-3105.59

3.4.1 Controller response

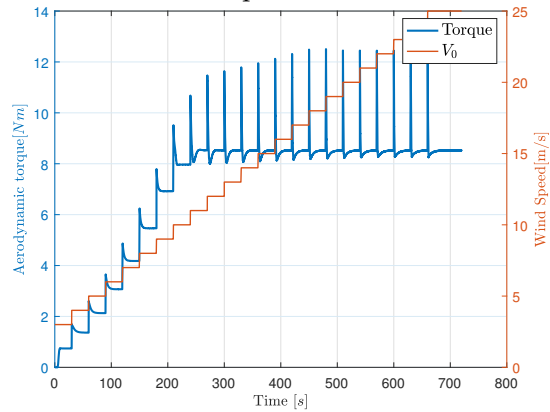
In this section the response of the controller to a wind speed step of 1 m/s applied for a time interval of 30s from 3m/s until 25 m/s has been shown. The response is slower for high wind speed above 20 m/s and can be rectified by selecting a larger value of ω_p for higher gains in the full load region. But, higher gains increase the aggressiveness of the response just above the rated wind speed. Considering the fact that the new turbine is designed for a low wind climate where wind speeds higher than 10m/s are unusual, the fatigue damage to the pitch servo can be mitigated with less aggressive gains.

(A) Controller step response of rotor speed Ω 

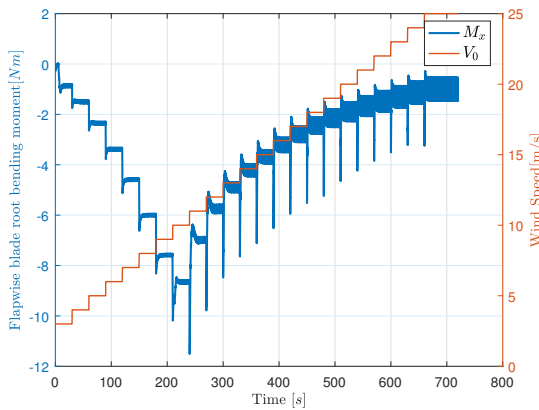
(B) Controller step response of aerodynamic power



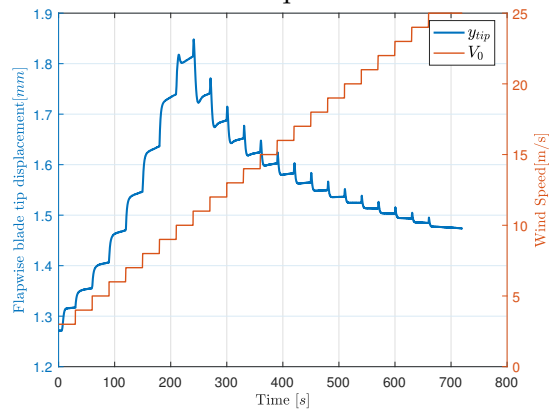
(C) Controller step response of pitch angle



(D) Controller step response of aerodynamic torque



(E) Controller step response of flapwise root bending moment



(F) Controller step response of flapwise tip displacement

3.4.2 Controller gains

The constant optimal C_p tracking factor K required for control in region 1 is calculated by Equation 3.16:

$$K = \eta \frac{0.5\rho AR^3 C_p(\theta_{opt}, \lambda_{opt})}{\lambda_{opt}^3} \quad (3.16)$$

The proportion and integral gain of the constant speed torque controller for control in region 2 are calculated by Equation 3.17 and Equation 3.18, respectively. The

total equivalent area moment of inertia ($I_r + n_g^2 I_g$) of the turbine is found to be $0.819467 Nm/(rad/s)$.

$$K_{Pg} = 2\eta\zeta_g\omega_g(I_r + n_g^2 I_g) \quad (3.17)$$

$$K_{Ig} = \eta\omega_g^2(I_r + n_g^2 I_g) \quad (3.18)$$

The proportion and integral gain of the constant power pitch controller for control in the full load region can be calculated by Equation 3.19 and Equation 3.20.

$$K_{Pp} = \frac{2\zeta_p\omega_p(I_r + n_g^2 I_g) - \frac{1}{\eta} \frac{\partial Q_g}{\partial \Omega}}{-\frac{\partial Q}{\partial \theta}} \quad (3.19)$$

$$K_{Ip} = \frac{\omega_p^2(I_r + n_g^2 I_g)}{-\frac{\partial Q}{\partial \theta}} \quad (3.20)$$

Table 3.6 provides a definition of all the parameters introduced for tuning the DTU Wind Energy controller.

TABLE 3.6: Description of control parameters

K :	Constant C_p tracking factor
K_{pg} :	Proportional gain of constant speed torque controller
K_{Ig} :	Integral gain of constant speed torque controller
ω_g :	Natural frequency of the partial load rigid body rotation pole.
ζ_g :	Damping ratio of the partial load rigid body rotation pole.
K_{Pp} :	Proportional gain of pitch controller
K_{Ip} :	Integral gain of pitch controller
ω_p :	Natural frequency of the full load rigid body rotation pole.
ζ_p :	Damping ratio of the full load rigid body rotation pole.
K_1 :	Linear gain scheduling factor.
K_2 :	Quadratic gain scheduling factor.
I_r :	Turbine rotor area moment of inertia
I_g :	Generator area moment of inertia
n_g :	Gear box ratio
$\frac{\partial Q}{\partial \theta}$:	Aerodynamic torque gradient with respect to pitch angle.
$\frac{\partial Q_g}{\partial \Omega}$:	Generator torque gradient with respect to rotational speed.

The constant torque control strategy used for generator torque control makes $\frac{\partial Q_g}{\partial \Omega}$ equal to 0. The required aerodynamic torque gradients are calculated by HAWC-Stab2 and summarised in Table 3.7. The aerodynamic torque gain with collective pitch angle is given by Equation 3.21:

$$\frac{\partial Q}{\partial \theta} = \frac{\partial Q}{\partial \theta} \Big|_{\theta=0} \left(1 + \frac{\theta}{K_1} + \frac{\theta^2}{K_2}\right) \quad (3.21)$$

where $\frac{\partial Q}{\partial \theta} \Big|_{\theta=0}$ is the gradient at zero pitch.

Equation 3.21 can be expressed as a second order polynomial equation:

$$\frac{\partial Q}{\partial \theta}(\theta) = p_2\theta^2 + p_1\theta + p_0 \quad (3.22)$$

Where, p_0 , p_1 and p_2 are constants. Using the known gradients from HAWC-Stab2, these constants can be calculated by polynomial fitting, and then K_1 and K_2

can be determined. This fitting is required in order to linearise the aerodynamic gains and is shown in Figure 3.11.

TABLE 3.7: Aerodynamic gradients calculated by HAWCStab2 and fitted gradients

θ [deg]	$\partial Q/\partial\theta$ [kNm/deg]	Fitted [kNm/deg]
1.84	-0.00096	-0.00088
7.46	-0.00135	-0.00139
10.74	-0.00157	-0.00168
13.37	-0.00180	-0.00190
15.62	-0.00205	-0.00210
17.64	-0.00229	-0.00227
19.55	-0.00251	-0.00243
21.41	-0.00274	-0.00258
23.21	-0.00282	-0.00273
24.96	-0.00290	-0.00287
26.64	-0.00300	-0.00301
28.25	-0.00306	-0.00314
29.80	-0.00318	-0.00326
31.29	-0.00331	-0.00338
32.71	-0.00352	-0.00349
34.08	-0.00363	-0.00359

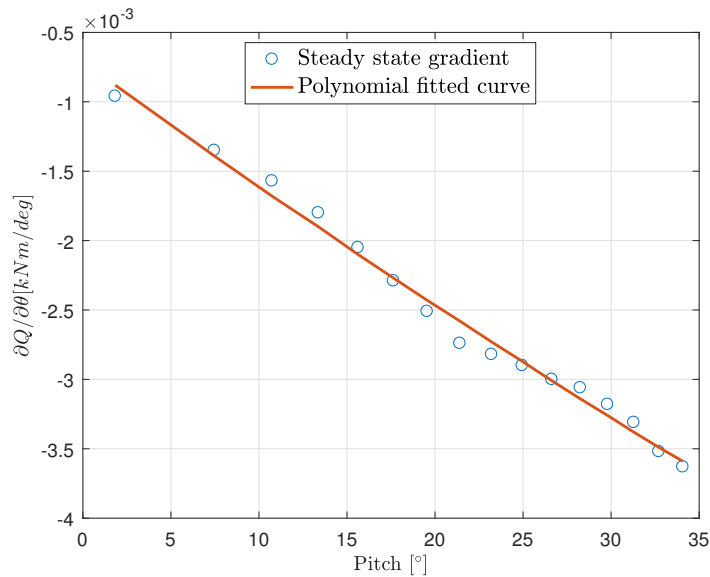


FIGURE 3.11: Gradient polynomial fit of aerodynamic gain scheduling

Chapter 4

Parametric studies

Two different reference blades are used to study the effect of bend-twist coupling through stiffness and load response parametric studies. Material coupling is introduced in these blades to varying degrees and their effect is analysed and compared. Based on this analysis a decision is made regarding the material to be selected in the final reference blade for the optimisation.

4.1 Stiffness study

The study in this section introduces material coupling in the carbon-epoxy and glass-epoxy reference blades generated in chapter 3. The bend-twist coupling is introduced by varying the fibre orientation in the unidirectional laminae from -35° to $+35^\circ$ in intervals of 5° . The blade has been partially coupled from 40% blade span (ie 0.3m from the root of the blade) and onwards. According to Botasso et al. [10] the blade sections near the maximum chord are the most affected by fatigue damage. Preventing fibre rotations in this part of the blade would not reduce the bending stiffness near the root and thus prevent excessive fatigue damage near the root. Additionally, the load reduction by BTC of a 30% partially coupled blade was found to be same as that for the fully coupled blade. Since the wind turbine loading is mostly concentrated near the mid and the tip span sections of the blade, this is the region where BTC towards feather would have the most effect in altering the angle of attack and reducing the loads.

As was explained in section 2.1, the fibre orientation on both the pressure side and suction side surface of the blade section have to mirror each other in order to achieve bending-torsion coupling. In the reference blades the unidirectional fibres in the laminate are aligned along the blade pitch axis from the root to the tip, ensuring a high flapwise bending stiffness for the structural configuration. In this case only the diagonal elements of the symmetric stiffness matrix shown in Equation 2.1 are non-zero while all other coupling stiffness terms are zero. An extended form of Equation 2.1 showcasing the fully populated stiffness matrix is shown in Equation 4.1.

$$\begin{pmatrix} F_x \\ F_y \\ T_z \\ M_x \\ M_y \\ M_z \end{pmatrix} = \begin{bmatrix} K_{11} & K_{12} & K_{13} & K_{14} & K_{15} & K_{16} \\ K_{12} & K_{22} & K_{23} & K_{24} & K_{25} & K_{26} \\ K_{13} & K_{23} & K_{33} & K_{34} & K_{35} & K_{36} \\ K_{14} & K_{24} & K_{34} & K_{44} & K_{45} & K_{46} \\ K_{15} & K_{25} & K_{35} & K_{45} & K_{55} & K_{56} \\ K_{16} & K_{26} & K_{36} & K_{46} & K_{56} & K_{66} \end{bmatrix} \begin{pmatrix} \epsilon_x \\ \epsilon_y \\ \epsilon_z \\ \kappa_x \\ \kappa_y \\ \kappa_z \end{pmatrix} \quad (4.1)$$

where the first matrix on right hand side of the equation is the 6X6 fully populated stiffness matrix, K_{11} is the shear stiffness in the edgewise direction (for the edgewise shear force along the x-axis F_x), K_{22} is the shear stiffness in the flapwise direction

(for the flapwise shear force along the y-axis F_y), K_{33} is the axial stiffness (for the axial force along the z-axis T_z), K_{44} is the flapwise bending stiffness (for flapwise bending moment M_x), K_{55} is the edgewise bending stiffness (for edgewise bending moment M_y) and K_{66} is the torsional stiffness (for torsional moment M_z). The rest of the stiffness terms in the stiffness matrix in Equation 4.1 are the coupling terms, which when have a non-zero value, link the direct displacement due to an acting load with displacements in other directions. Due to the symmetric nature of the stiffness matrix these terms are mirrored about the leading edge diagonal, as seen in Equation 4.1. The coupling terms important for this stiffness study are located in the last column of this matrix until K_{66} . K_{16} and K_{26} couples the shear strains of the laminate and K_{36} couples the axial strain with the torsional deflection. While K_{46} and K_{56} couples the flapwise and edgewise deflections due to M_x and M_y with the torsional deflection. The term K_{46} is the flap-torsion coupling stiffness term.

On varying the fibre orientations, the structural stiffnesses are expected to decrease from their reference value. However, it is also expected that by introducing this variation in a mirrored sense the flap-torsion coupling stiffness or the K_{46} term obtains non-zero values. According to the theoretical formulation of this phenomenon applied to thin-walled skin sections by Karaolis et al. [24], all other coupling terms except K_{46} will either be zero or have a negligible value. However, this theory was formulated for a symmetric elliptical tube representative of a blade section. In reality, blade cross-sections consist of airfoils that may or may not be symmetric in one plane, and except at or near the root, are certainly not elliptical or circular in nature. The terms in the stiffness matrix shown in Equation 4.1, depend not only on the laminate thickness and fibre orientation but also on the physical dimensions (chord and relative thickness) and the symmetry of the blade cross-section. The current blade configuration employs an asymmetric airfoil as seen from the profile shown in Figure 3.2. Thus, other off-diagonal torsion coupling stiffness terms may also obtain non-zero values along with K_{46} .

In section 2.1, it was also theoretically explained that BTC towards feather would be produced when the bending-torsion coupling stiffness term K_{46} would obtain a negative value. Whereas, a positive value of this term would produce BTC towards stall which is undesired in the present study. Thus, it is important to establish the orientation of the fibre layup angle that would produce a negative value of K_{46} in the coordinate system being used by cross-sectional tool BECAS.

The aim of the stiffness parametric study is to:

- Identify contributions from all the torsion coupling stiffness terms.
- Identify the orientation of the fibre layup angle that produces BTC towards feather.
- Identify the material (carbon-epoxy or glass-epoxy) that is more conducive towards bend-twist coupling.
- Confirm the dependence of cross-sectional stiffness terms on the chord and laminate thickness values, as stated in the theoretical formulations by Kooijman [26].

In the upcoming section, the stiffness terms will be referred by their denotations taken from the fully populated stiffness matrix. Thus, in order to facilitate the ease

of reading the various stiffness terms from the figures and text in subsection 4.1.1, a look-up table is provided in Table 4.1. It contains a description of the important stiffness terms from the stiffness matrix in Equation 4.1 and their units.

TABLE 4.1: Description of relevant stiffness terms

Stiffness terms	Description	Units
K_{11}	Edgewise shear stiffness	$[N]$
K_{16}	Term coupling the edgewise shear stiffness and torsion	$[Nm]$
K_{22}	Flapwise shear stiffness	$[N]$
K_{26}	Term coupling the flapwise shear stiffness and torsion	$[Nm]$
K_{33}	Axial force stiffness in the direction along the length of blade	$[N]$
K_{36}	Term coupling axial force stiffness and torsion	$[Nm]$
K_{44}	Flapwise bending stiffness	$[Nm^2]$
K_{46}	Flapwise bending-torsion coupling term	$[Nm^2]$
K_{55}	Edgewise bending stiffness	$[Nm^2]$
K_{56}	Edgewise bending-torsion coupling term	$[Nm^2]$
K_{66}	Torsion stiffness	$[Nm^2]$

4.1.1 Results and Discussion

In this section the results of the stiffness parametric study are presented and discussed.

Effect of variation in fibre angles

Altering the fibre orientation angle of the unidirectional laminae of the reference blades has varied effects on the stiffness terms listed in Table 4.1. The response of the blade cross-sections for both the glass and carbon fibre blades can be seen in Figure 4.1. Figure 4.1a and Figure 4.1b show the response of the main stiffness terms belonging to the leading edge diagonal of the stiffness matrix to the change in fibre-orientation angles for carbon and glass fibre blades, respectively. The K_{11} , K_{22} and K_{66} stiffness terms are seen to increase in magnitude from their reference value with increasing magnitudes of fibre orientations, irrespective of the angle's sign. Whereas, the K_{33} , K_{44} and K_{55} stiffness terms decrease in magnitude for the same change in the fibre angles. The change in these stiffness terms are also observed to be symmetric in nature about the reference fibre angle. Each stiffness term is seen to obtain the same value for the same absolute magnitude of the fibre angle either side of the 0° mark. When made a function of the fibre angle these stiffness terms either attain their respective maxima or minima at the reference fibre orientation. Mathematically, the stiffness terms K_{11} , K_{22} , K_{33} , K_{44} , K_{55} and K_{66} can be regarded as even functions.

In subsection 3.3.2 the spanwise distribution of the glass and carbon fibre reference blades had been compared, and it was observed that the carbon fibre blade had higher K_{44} , K_{55} and K_{66} stiffnesses than its glass fibre counterpart. The same behaviour is also observed with changing fibre angles, as shown in Figure 4.2c. However, the rates at which the stiffnesses change with changing fibre angles is seen to differ between the two materials. The difference in K_{44} and K_{55} between glass and carbon is the highest at a fibre angle of 0° . This difference decreases with increasing magnitudes of the fibre orientation, indicating a varied rates of change of the

stiffnesses for carbon and glass fibre. For K_{44} and K_{55} the rate of decrease in the stiffnesses for the carbon fibre laminate is greater than that of the glass fibre laminate. A similar difference in the rates of change of the torsional stiffness K_{66} is also observed. However, in this case the difference in the glass and carbon fibre torsional stiffness terms increases with increasing magnitudes of the fibre orientation. The rate of increase of K_{66} is greater in the carbon fibre laminate than the glass fibre laminate.

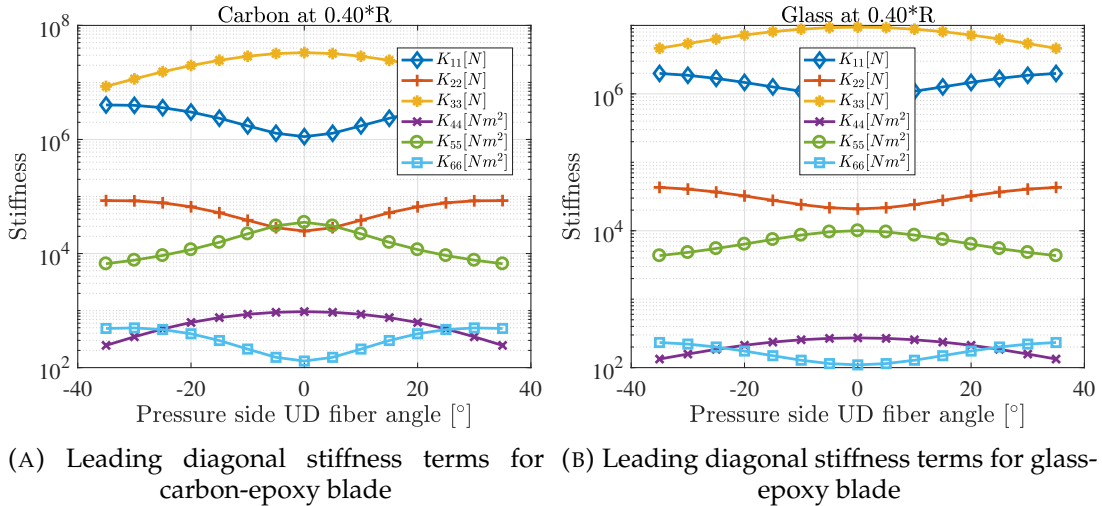


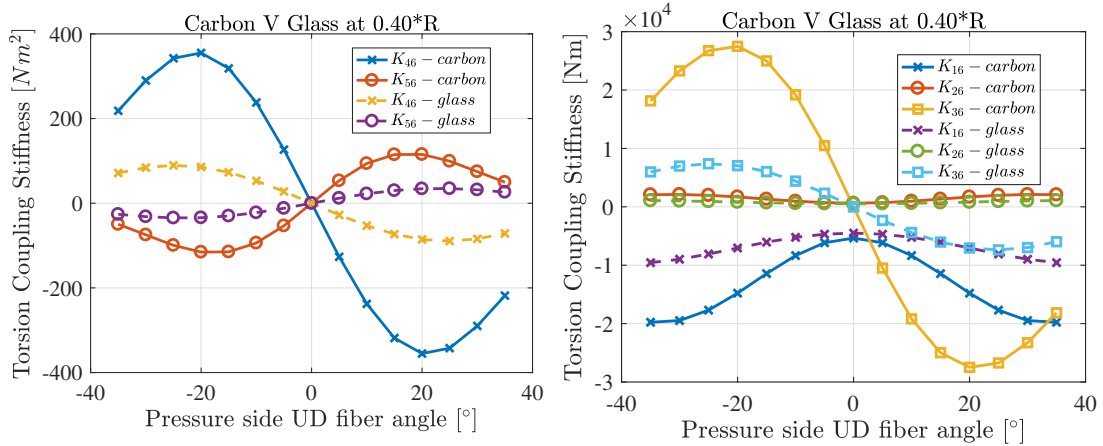
FIGURE 4.1: Cross-sectional stiffness terms at 40% blade length

4.1.2 Coupling with torsion

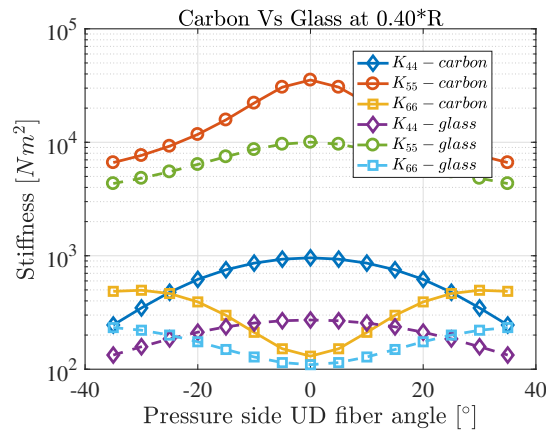
Flapwise and edgewise bending

The flapwise bending-torsion and edgewise bending-torsion coupling stiffnesses K_{46} and K_{56} can, mathematically, be regarded as being odd functions of fibre angle. They obtain the same magnitude with opposing sign for corresponding positive and negative fibre angles, as seen in Figure 4.2a. For the same fibre angle, the stiffnesses of the carbon fibre laminate are greater in terms of their absolute magnitude than their glass fibre counterparts. Since the flapwise and edgewise bending torsion coupling terms have a zero value at the reference fibre angle, the greater magnitude observed in the carbon fibre blade can be attributed to a higher rate of change of the K_{46} and K_{56} terms with respect to a change in the fibre angle, than compared to the glass fibre blade.

As explained in the beginning of section 4.1, the strength of flapwise bend-twist coupling and its final desired effect depends on both the sign and magnitude of the K_{46} stiffness term. The sign of this term determines whether the desired twisting would be towards the stall accompanied by an increase in the local sectional angle of attack (positive K_{46}) or towards the feather accompanied by a decrease in the local sectional angle of attack (negative K_{46}). The magnitude of the K_{46} term together with the magnitude of the flapwise bending stiffness term K_{44} , plays an important role in determining the strength of achievable flapwise bending-torsion coupling. This will however be discussed in detail in the subsection 4.1.3 on the coupling factor. From Figure 4.2a two observations can be made in this regard. First, for positive values of the fibre layup angle the K_{46} term attains negative values. Thus, in order to achieve bend-twist coupling towards feather the positive range of fibre layup angles



(A) Flap-torsion and edge-torsion coupling stiffness terms (B) Shear-torsion and axial-torsion coupling stiffness terms



(C) Comparison of leading diagonal stiffness terms between glass and carbon fibre blades

FIGURE 4.2: Comparison of cross-sectional stiffnesses between carbon and glass fibre blades at 40% blade length

needs to be considered. Second, the highest magnitude of the K_{46} term is attained at a fibre angle of $\pm 20^\circ$ for the carbon fibre cross-section, and at $\pm 25^\circ$ for the glass fibre cross-section. This can be clearly seen from Figure 4.3a, which shows the relative change of the normalised flapwise bending stiffness K_{44} and flapwise bending-torsion coupling stiffness K_{46} with respect to their corresponding maximum values for cross-sections located at 40% blade length for both glass and carbon fibre blade cross-sections. The K_{44} term is seen to decrease with respect to its maximum value at the reference fibre angle for both the carbon and glass fibre blade. It can also be visually confirmed that this decrease is greater for carbon fibre blade than compared to the glass fibre blade. Additionally, the rate of change in the normalised stiffnesses are seen to be the same irrespective of the cross-sectional dimensions of the laminates due to their spanwise locations. This can be observed from Figure 4.3b, wherein the absolute error between the corresponding normalised stiffness at 40% and 90% blade length of the carbon fibre blade are shown. It is seen that the error is in the order of magnitude of 10^{-3} to 10^{-4} . Thus, although the absolute values of these stiffnesses relatively decrease with a reduction in the dimensions of the cross-section, the rate of change of their stiffnesses with respect to the fibre angles remain the same. These rates of change are thus only affected by the symmetry and cross-sectional shape of the blade section.

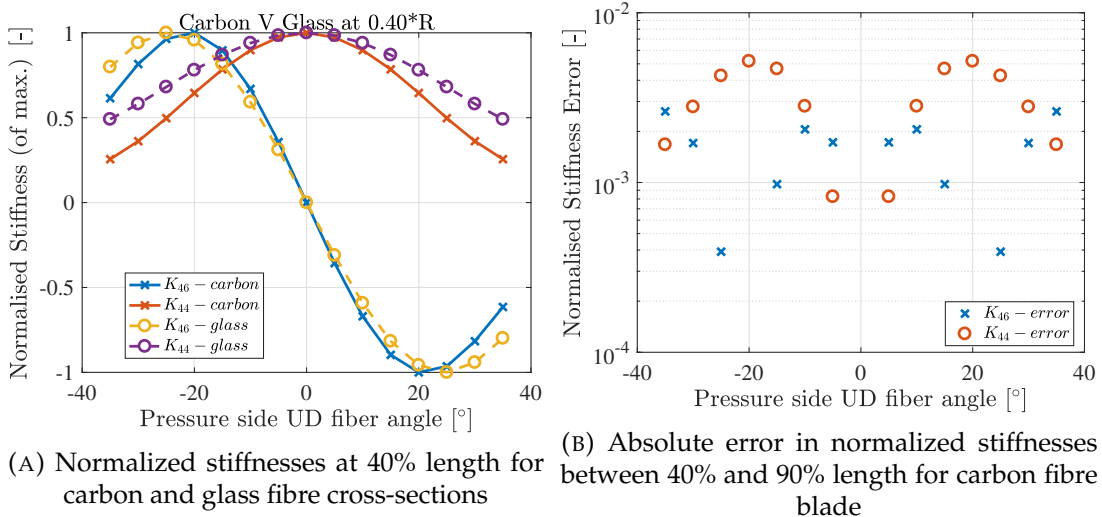


FIGURE 4.3: Flapwise bending and flap-torsion coupling stiffness terms normalised by their cross-sectional maximum values

From Figure 4.2a it is also seen that the edgewise bending torsion coupling term K_{56} has a relatively lower absolute magnitude than the corresponding K_{46} term in both glass and carbon fibre cross-sections. Additionally the signs of the K_{46} and K_{56} terms are also opposite in sense for the same fibre layup angle. Thus, although positive value of the fibre layup angle aids in twisting the blade section towards feather in relation to the flapwise bend-twist coupling K_{46} , the opposite is true for the edgewise bend-twist coupling K_{56} . Positive values of the fibre layup angle assigns a positive value to the K_{56} term, leading to a twist towards stall as a result of a deflection in the positive edgewise direction (x-direction positive towards the trailing edge). While a negative value of the fibre layup angle would assign a negative value to the K_{56} resulting in the edgewise deflection contributing in twisting the blade section towards feather.

Edgewise and flapwise shear, and axial extension

The response of the shear and longitudinal extension - torsion coupling terms (K_{16} , K_{26} and K_{36}) with respect to the variation of the fibre orientation, for both glass and carbon fibre laminate at 40% blade span, is shown in Figure 4.2b. Once again, it is seen that the absolute magnitude of the stiffness terms for the carbon fibre laminate are greater than the corresponding values of their glass fibre counterparts.

However, the shear extension-coupling terms K_{16} and K_{26} , distinctly differ from rest of the three torsion-coupling terms. Primarily, they have a non-zero value even when the rest of the coupling terms are zero for the reference blade with a 0° fibre layup angle. The flapwise and edgewise shear forces F_y and F_x (due to the thrust and tangential aerodynamic forces) acting on the blade section are responsible for creating the flapwise and edgewise bending moments and the corresponding deflections occurring in the blade. Hence, the shear forces give rise to the normal stresses resulting in the bending of the blade and as such their contributions are captured through the flapwise and edgewise bending moments, deflections and stiffnesses. Additionally, these forces can give rise to twisting in the blade if their corresponding equivalent of the distributed force is not applied at the shear centre of the cross-section. When a shear force acts at the shear centre it produces only bending moment without a torsional moment [25]. The location of the shear centre is dependent on the geometry and the presence of symmetry in the cross-section. Due to the lack of symmetry in the blade cross-sections, on application of shear forces the blade experiences unsymmetrical bending. In this regard, the non-zero value of K_{16} and K_{26} for the reference fibre angle is a result of the asymmetrical blade cross-section and indicates the presence of a shear force contribution to the torsional deflection in the reference case.

The absolute magnitudes of both K_{16} and K_{26} increase with rising fibre angle values, from their minima at the reference fibre angle. The edgewise shear-torsion coupling stiffness K_{16} is much larger in magnitude than the flapwise shear-torsion coupling stiffness K_{26} , with negative values for all fibre angles between -35° to $+35^\circ$. Whereas, K_{26} has positive values for the range of fibre angles investigated in this study but has a relatively smaller magnitude. K_{26} also shows a very gradual rate of increase with rising fibre angles, when compared to K_{16} where a much steeper rate of increase is noticed. Thus, for larger fibre angles the contribution from the twist due to the edgewise shear coupling is greater compared to that by the flapwise shear force. From Figure 4.1, it is evident that both the edgewise and flapwise shear stiffnesses are much higher than the bending or torsional stiffnesses. Additionally, the edgewise shear stiffness is approximately 10 times higher than the flapwise shear stiffness at the reference fibre angle. Such high values of K_{11} and K_{22} indicate a much lower contribution to the overall twist angles by the shear forces when compared to the flapwise and edgewise bending moments. For example, K_{11} is approximately 10^3 times higher than the flapwise bending stiffness and 10^1 times higher than the edgewise bending stiffness at the reference fibre angle. This gap further increases with larger magnitudes of fibre angles as the magnitude of K_{11} increases while that of K_{44} and K_{55} decreases. Although, K_{16} is approximately 10^2 times higher in magnitude than K_{46} even for its largest magnitude at a fibre angle of 20° , the degree of contribution to the overall torsion by the edgewise shear coupling will still be severely limited by the high value of K_{11} . Even though the flapwise shear stiffness value K_{22} is lower than K_{11} , the coupling term K_{26} is of the same order of magnitude as K_{46} . When considered together with the comparatively lower value of the flapwise bending stiffness, the contribution to torsion due to the flapwise shear

will be relatively lower.

The variation of the axial force-torsion coupling stiffness K_{36} is shown in Figure 4.2b. The variation in K_{36} is seen to follow a similar trend as seen in K_{46} , albeit with a relatively higher magnitude. Like K_{46} , K_{36} too attains its highest magnitude at a fibre angle of $\pm 20^\circ$ for carbon fibre and $\pm 25^\circ$ for glass fibre. Additionally mirroring K_{46} , K_{36} attains negative values for positive fibre angle and positive values for negative fibre angle. Thus, in implementation of flapwise bending-torsion coupling towards feather, an increase in the axial force T_z gives a positive elastic torsion towards feather contributing towards a decrease in the local angle of attack. The axial force T_z is the result of the centrifugal forces acting on the blade and as such is proportional to the mass and square of the rotational speed Ω^2 and increases in magnitude towards the root. However for the 0.75m blade considered in this thesis with a laminate thickness of 1mm, the involved length and blade mass are low enough for insufficient axial forces to develop that can overcome the high axial stiffness K_{33} . Similar to the shear force, the contribution to the induced torsion from the axial force can be considered to be negligible. In order to exploit tension-torsion coupling helical plies can be used in the composite layup instead of a "mirror" layup. More information in this regard to this can be obtained from Karaolis et al. [24].

Secondary couplings

Along with the main contribution to the induced torsion from the flapwise bending, the asymmetric profile of the blade cross-sections results in contributions to the induced torsion from edgewise bending, edgewise and flapwise shear forces, and axial tension. The edgewise and flapwise shear forces directly contribute directly to the torsional moment M_z affecting the torsional deflection. The contributions of these secondary couplings have been qualitatively discussed in subsection 4.1.2. In summary, a high applied force or moment, low direct stiffness and torsional stiffness along with a high coupling stiffness are factors conducive to a strong contribution to the induced torsion.

In order to highlight this point only the flapwise bending and torsion coupling terms from Equation 4.1 are considered. In order to simplify the analysis the following assumptions are made:

- Only the absolute value of the terms involved are considered. Hence, all terms are positive.
- The coupling term K_{46} has a non-zero value.
- The contribution from other coupling terms are ignored.

A coupling equation formulated between flapwise bending and torsion is reorganised and normalised to represent the curvature for torsional deflection κ_z as shown in Equation 4.2 and Equation 4.3. In Equation 4.2 the terms have been normalised by the flapwise bending-torsion coupling stiffness K_{46} , while in Equation 4.3 they have been normalised by the torsional stiffness K_{66} .

$$\kappa_z = \frac{1}{|K_{46}|} |M_x| - \frac{|K_{44}|}{|K_{46}|} |\kappa_x| \quad (4.2)$$

$$\kappa_z = \frac{1}{|K_{66}|} |M_z| - \frac{|K_{46}|}{|K_{66}|} |\kappa_x| \quad (4.3)$$

In the equations above, it is seen that for the same applied loads and κ_x , minimising the stiffness ratio of K_{44}/K_{46} and maximising the ratio of K_{46}/K_{66} would result in larger torsional deflections which would in-turn affect the aerodynamic characteristics of the section to a greater extent. This should be regarded as a simplified analysis, as the actual values of the torsional deflection would also largely depend on the magnitude of the applied aerodynamic forces, the flapwise tip deflection and to a certain extent on the contributions from the secondary couplings. For the present study these ratios have been shown in Figure 4.4 for both carbon and glass fibre blades at 40% blade length.

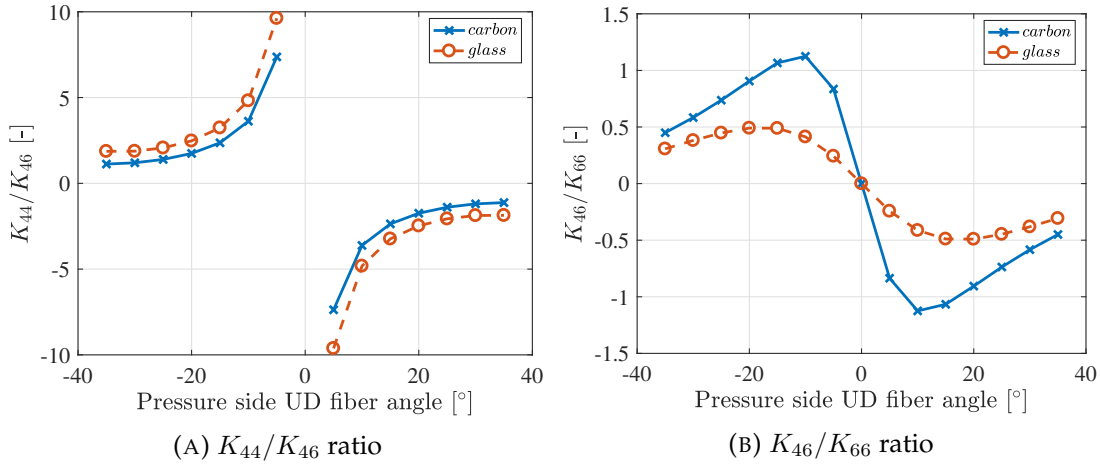


FIGURE 4.4: K_{44}/K_{46} and K_{46}/K_{66} ratios for carbon and glass fibre blade sections at 40% blade length

Several studies in the existing literature for BTC applied to turbines of various sizes have highlighted the contribution to the induced torsion from the flapwise bending moment as the most important factor affecting the performance of the turbine. The thrust force and the resulting flapwise bending moment are the largest of all the aerodynamic loads applied on a wind turbine. In addition, apart from the torsional stiffness, the flapwise stiffness of turbine blades is usually the lowest. In this thesis, the BTC towards feather is studied by assigning importance to flapwise bending-torsion coupling as the main driver of induced torsion. In order to achieve this, positive fibre layup angles will be chosen in the laminae. The contributions from the secondary couplings are considered negligible and as such are not individually studied in greater detail. However, regardless of the considerations made for simplifications in the analysis, cognisance is given to the contributions of these secondary couplings. Their contributions towards the induced torsion for positive fibre layup angle are listed from a qualitative view point in Table 4.2.

TABLE 4.2: Contributions of secondary couplings to the induced torsion for positive fibre layup angles

Torsion coupling terms	Sign	Effect on induced torsion
Edgewise shear- K_{16}	Negative	Twist towards feather
Flapwise shear- K_{26}	Positive	Twist towards stall
Axial tension- K_{36}	Negative	Twist towards feather
Edgewise bending- K_{56}	Positive	Twist towards stall

4.1.3 Coupling factor

The coupling factor has been introduced briefly in subsection 2.1.1. The mathematical formulation of the coupling factor α was developed by Lobitz and Veers [32] to quantify the amount of coupling seen in BTC blades. This formulation has been reproduced for convenience in Equation 4.4 from Equation 2.4. The notations for the stiffnesses in Equation 4.4 are same as those used in the fully-populated matrix in Equation 4.1.

$$K_{46} = \alpha \cdot \sqrt{K_{44}K_{66}}, \quad -1 < \alpha < 1 \quad (4.4)$$

A negative coupling factor α represents twist coupling towards feather, a positive value represents twist coupling towards stall while a zero value of the coupling parameter represents an uncoupled blade. Greater the magnitude of the coupling parameter, greater is the coupling between bending and torsion in the blade. Mathematically, the limits of the coupling factor α are between -1 and 1. However, Ong, Wang and Tsai [42] showed that practically the maximum coupling limits were between -0.6 and 0.6. This was observed for Carbon/epoxy laminate that showed the highest coupling amongst known FRPs with a theoretical limit of α between 0.8 and -0.8. They identified that along with the fibre orientation, the ply orientation, the laminate material, torsion warping and the proportional volume of anisotropy layers in the laminate had the greatest impact on the coupling factor.

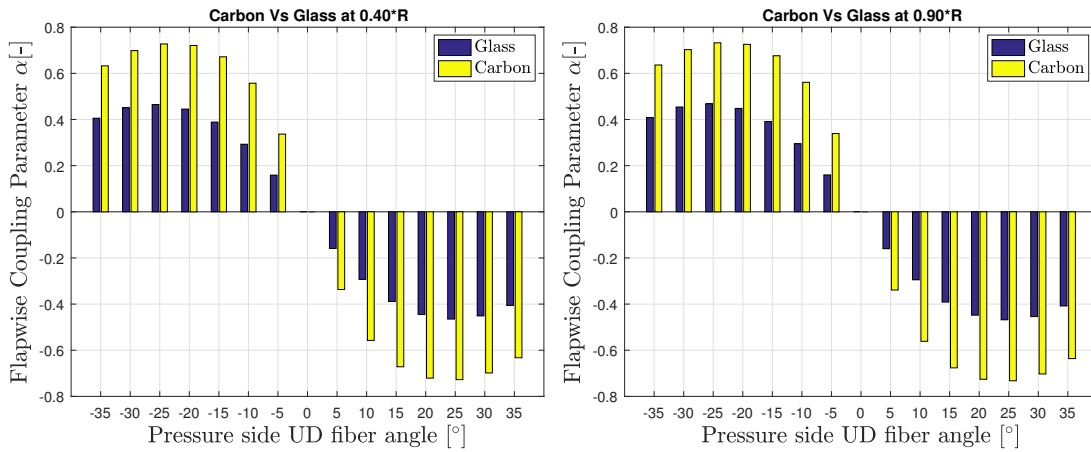
In the current study, the ply is oriented with the main axis along the blade span axis and torsion warping has been ignored. The blade sections are made of 2 layers of unidirectional laminae with both being anisotropic in nature. With these influences being fixed, the coupling factor can be affected by the choice of material to be used in the blades. The choice to be made is between carbon-epoxy and glass-epoxy FRP. In this stiffness study, it was seen in the earlier sections that a blade cross-section made of carbon fibre recorded larger stiffnesses across the board than when it was made of glass fibre. With regard to bend-twist coupling, carbon fibre cross sections have higher flapwise bending stiffness K_{44} and flapwise bending-torsion coupling stiffness K_{46} than their glass fibre counterparts. At the same time, as seen in Figure 4.3a, the rate of decrease in the normalised flapwise bending stiffness from its reference value for the carbon fibre section is higher, accompanied by a marginally higher rate of increase in the normalised K_{46} , with growing magnitudes of the fibre layup angle. This indicates a relatively higher tendency in carbon fibre sections of achieving BTC as the fibre angle is increased from that in the uncoupled case. It was also observed in Figure 4.4 that the higher values of K_{46} and K_{44} in carbon fibre sections than the glass fibre sections, translated to lower K_{44}/K_{46} ratios and higher K_{46}/K_{66} ratios across the range of fibre layup angles, which is conducive to a higher magnitude of induced torsion. It was also seen that carbon fibre sections achieved maximum coupling at a smaller fibre orientation than the glass fibre sections.

The affinity of carbon fibre sections towards BTC is further confirmed by the coupling factors for different fibre angles. The variation of coupling factor α over the range of fibre angles for both carbon fibre and glass fibre is shown in Figure 4.5 for 40% and 90% blade length. It is seen that carbon fibre has higher magnitudes of coupling factor for the entire range of fibre angles compared to the glass fibre section. The maximum and minimum values for negative and positive values of the fibre layup angles are shown in Table 4.3. The relatively high stiffnesses in shear, axial tension and edgewise bending compared to glass fibre sections could possibly indicate a lower contribution to induced torsion. The lower mass density of the carbon fibre laminae than the glass fibre laminae indicate the development of lower axial forces, thus lowering its contribution to coupling compared to the glass fibre

blade. Thus, greater contribution from flapwise bend-twist coupling and lower contributions from secondary couplings would make carbon fibre a good choice for the material to be used in the final reference blade for the optimisation. However, the contributions from the secondary couplings cannot be accounted solely based on their stiffnesses alone. It is thus considered prudent to consider the results from the steady state load response study in section 4.2 to make the final decision regarding the material. Additionally, the relative costs of the two materials in question also are to be considered in the final decision.

TABLE 4.3: Maximum and minimum coupling factor for carbon and glass fibre blade cross-sections

Material	Maximum value	Minimum value
Carbon-epoxy	0.73	-0.73
Glass-epoxy	0.46	-0.46



(A) Flapwise bending-torsion coupling factor at 40% blade length (B) Flapwise bending-torsion coupling factor at 90% blade length

FIGURE 4.5: Flapwise bending-torsion coupling factor comparison for carbon and glass fibre blade cross-sections

4.1.4 Reduced stiffnesses

In the mathematical derivation of the stiffness matrix for the blade cross-section from the classical lamination theory, Kooijman [26] in his report, showed the dependence of the resulting stiffness terms on the dimensions of the blade cross-section and the laminate thickness. The stiffness matrix in Equation 4.1 is modified to accommodate these dependencies and is shown in Equation 4.5.

$$\begin{pmatrix} F_x \\ F_y \\ T_z \\ M_x \\ M_y \\ M_z \end{pmatrix} = \begin{bmatrix} K_{11}^* tc & K_{12}^* tc^2 & K_{13}^* tc^2 & K_{14}^* tc^2 & K_{15}^* tc^2 & K_{16}^* tc^2 \\ K_{12}^* tc^2 & K_{22}^* tc & K_{23}^* tc^2 & K_{24}^* tc^2 & K_{25}^* tc^2 & K_{26}^* tc^2 \\ K_{13}^* tc^2 & K_{23}^* tc^2 & K_{33}^* tc & K_{34}^* tc^2 & K_{35}^* tc^2 & K_{36}^* tc^2 \\ K_{14}^* tc^2 & K_{24}^* tc^2 & K_{34}^* tc^2 & K_{44}^* tc^3 & K_{45}^* tc^3 & K_{46}^* tc^3 \\ K_{15}^* tc^2 & K_{25}^* tc^2 & K_{35}^* tc^2 & K_{45}^* tc^3 & K_{55}^* tc^3 & K_{56}^* tc^3 \\ K_{16}^* tc^2 & K_{26}^* tc^2 & K_{36}^* tc^2 & K_{46}^* tc^3 & K_{56}^* tc^3 & K_{66}^* tc^3 \end{bmatrix} \begin{pmatrix} \epsilon_x \\ \epsilon_y \\ \epsilon_z \\ \kappa_x \\ \kappa_y \\ \kappa_z \end{pmatrix} \quad (4.5)$$

where t is the thickness laminate and c is the chord length of the cross-section. Thus, $[K_{ij}^*]$ represents the terms of the reduced stiffness matrix independent of their dependence on t and c . The reduced stiffnesses are only dependent on the symmetry and material properties of the profile. From this property they should be the same for any section of the blade span that uses the same airfoil profile. This is confirmed from Figure 4.6, which shows negligible difference in the reduced stiffnesses between sections at 40% and 90% blade length for both carbon and glass fibre blades. For improved readability only the important stiffnesses i.e. K_{44} , K_{55} and K_{66} have been shown in Figure 4.6.

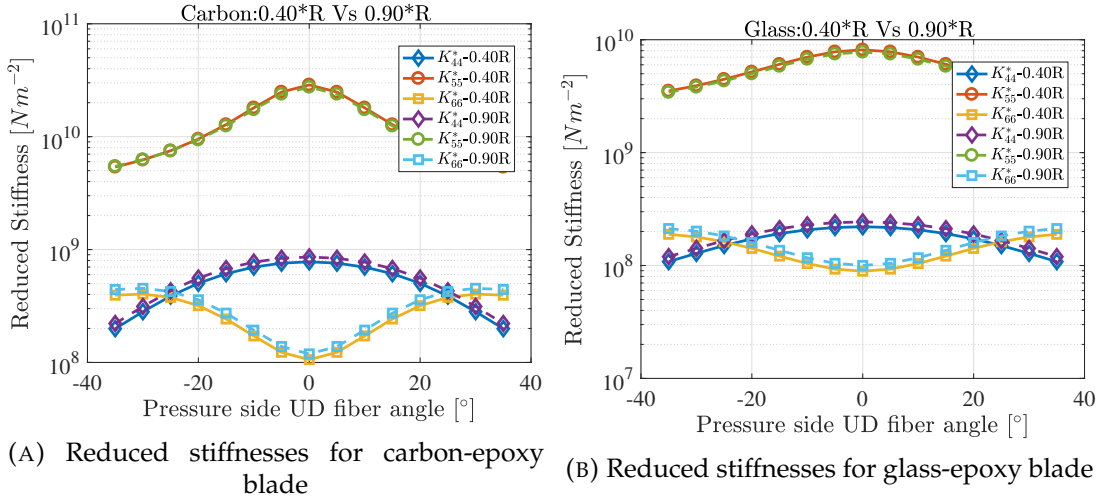


FIGURE 4.6: Comparison of reduced cross-sectional stiffnesses between 40% and 90% blade length

4.1.5 Summary

Bend-twist coupling was introduced in the reference blade geometry defined in chapter 3. Two reference blades were made of uniformly thick, unidirectional laminates with one entirely made of carbon-epoxy FRP and the other of glass-epoxy FRP. The fibre angles in the reference blade were maintained uniformly at 0° with the blade pitch axis. Bend-twist coupling was activated by altering the fibre angles from -35° to $+35^\circ$ at an interval of 5° defined with respect to the positive z-axis running from root to the tip. The blades were partially coupled from 40% blade span, corresponding to a distance of 0.3m from the root, and onward. The cross-sectional stiffnesses of the variably coupled blade and their contributions towards BTC were analysed in this study. As stated in the introductory paragraph of this section, the main aim of this study was to identify the contributions of the torsion coupling stiffness terms towards BTC, the fibre angle range that would result in twisting towards feather, the material most conducive to BTC amongst carbon and glass composites, and the dependence of the stiffnesses on cross-sectional dimensions.

A few concluding remarks have been listed below:

- Asymmetric cross-sections results in couplings between shear forces, axial tension, edgewise moment and torsion, in addition to the flapwise BTC.
- Secondary couplings individually influence the induced torsion to a lesser extent than the flapwise BTC. However, irrespective of the magnitude their combined contributions ultimately does influence the torsional deflection.

- Flapwise BTC towards feather was achieved for all positive fibre layup angles.
- A low ratio of flapwise bending stiffness to flapwise bending-torsion coupling stiffness K_{44}/K_{46} and a high ratio of flapwise bending-torsion coupling stiffness to torsional stiffness K_{46}/K_{66} would result in the highest magnitude of torsional deflection provided the moments and deflection remain the same. In generalised terms, low flapwise bending stiffness and torsional stiffness along with a high coupling stiffness results in a stronger BTC.
- Carbon outperforms glass for all fibre angles with regard to the amount of coupling seen in the cross-sections. Due to the high values of stiffnesses and lower mass density, the effect of secondary couplings may be less pronounced in carbon compared to glass. However, as the net effect of the contributions from the secondary couplings cannot be judged based on the stiffnesses alone, the response of BTC under wind loads should be considered to choose the final material.
- For the same cross-sectional profile and material the flapwise bending stiffness, torsional stiffness and the bending-torsion coupling stiffness scale with tc^3 . Where t is the laminate thickness and c is the chord of the section.

4.2 Load response: Steady

A parametric study is conducted to gauge the response of the structure to the wind loads experienced in the wind climate as specified by the Small Wind Turbine Competition. The purpose of this study is to qualify the expected behaviour of the rotor with increasing fibre layup angles that induce twist towards feather. It also would further justify the choice of material for the blade based on an assessment of the performance. Furthermore, it would give an overview of the magnitude of loads and corresponding deflections that can be expected under the present iteration of the rotor configuration. The 10-min average wind speed V distribution is represented by a Weibull distribution defined by the scale parameter $A=4.5\text{m/s}$ and shape parameter $k=2$. The resulting distribution has a mean wind speed of $V_{mean} = 4\text{m/s}$. The probability density function (pdf) and cumulative distribution function (cdf) are shown in Figure 4.16a and Figure 4.16b. The preliminary design of the rotor is simulated at steady wind speeds ranging from $V_{cut-in} = 3\text{m/s}$ to $V_{cut-out} = 16\text{m/s}$ with an increment of 1m/s using the aero-servo-elastic code HAWC2 [29]. The simulated wind is devoid of turbulence and atmospheric boundary layer effects including wind shear. Additionally, the tower shadow effect has been ignored. A total of 192 simulations are performed for both glass and carbon FRP UD blades for fibre-layup angles that initiate BTC with twist towards feather, for 0° , $+5^\circ$, $+10^\circ$, $+15^\circ$, $+20^\circ$, $+25^\circ$ and $+30^\circ$. The blade with a fibre layup angle of 0° doesn't display BTC effects and is considered to be the baseline case. The blade has been coupled from 40% blade length and on-wards. A summary of the preliminary design is given in Table 4.4.

4.2.1 Results and Discussion

In this section the results of the load response study are presented.

TABLE 4.4: Preliminary design summary of the rotor

Parameter	Value
Power Rating	500 W
Rotor Orientation, Configuration	Upwind, 3 blades
Control	Variable speed, Collective Pitch
Rotor, Hub Diameter	1.58 m, 0.08 m
Hub Height	1.3 m
Cut-in, Rated, Cut-out Wind Speed	3 m/s, 10 m/s, 16 m/s
Cut-in, Rated Rotor Speed	181.24 rpm, 604.85 rpm
Maximum Tip Speed	50.04 m/s
Shaft Tilt Angle	0°
Rotor Precone Angle	0°
Prebend	0 m
Blade fibre laminate thickness	1 mm
Blade Mass: Carbon FRP blade	255 g
Blade Mass: Glass FRP blade	318 g

Flapwise loads and deflections

The matrix system shown in Equation 4.6, represents the reduced stress-strain relationship of the blade structure applied to include only the flapwise bending and torsion moments, and their corresponding deflections for the bend-twist coupled blade.

$$\begin{bmatrix} K_b & K_{btc} \\ K_{btc} & K_t \end{bmatrix} \begin{pmatrix} \kappa_x \\ \kappa_z \end{pmatrix} = \begin{pmatrix} M_x \\ M_z \end{pmatrix} \quad (4.6)$$

where K_b is the flapwise bending stiffness, K_t is the torsional stiffness, K_{btc} is term that couples flapwise bending with torsional deflections, κ_x is the curvature in the flapwise direction, and κ_z is the curvature representing torsional deflection. M_x and M_z are the external flapwise bending moments due to the aerodynamic forces. The system in Equation 4.6 can be re-written as shown in Equation 4.7 and Equation 4.8 in order to fully grasp their coupled nature.

$$K_b \cdot \kappa_x + K_{btc} \cdot \kappa_z = M_x \quad (4.7)$$

$$K_t \cdot \kappa_z + K_{btc} \cdot \kappa_x = M_z \quad (4.8)$$

Equation 4.7 shows that for the bend-twist coupled blade the external flapwise bending moment M_x is balanced by the response of the structure due to a deflection in the flapwise direction and also the torsional deflection of the blade. In general, it is noted that for the same external moment a higher bending stiffness K_b will result in a lower deflection κ_x , with the converse being true as well. When the fibre orientation in the composite layup of the blade is changed to couple the blade, there is a decrease observed in the flapwise bending stiffness K_b with a simultaneous increase in the bending-torsion coupling stiffness K_{btc} . For BTC towards feather K_{btc} attains increasingly negative values for rising fibre layup angle. Thus, for the coupled blade the flapwise deflection will re-adjust to a higher value due to the decreased flapwise bending stiffness. Since some of the applied aerodynamic moment M_x also goes in twisting the blade, the flapwise deflection will be lower than its value for the same K_b without bend-twist coupling. Whereas, for the uncoupled case the bending moment would in its entirety be responsible for the flapwise deflection. Equation 4.8

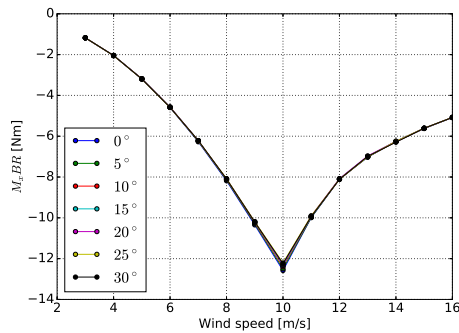
shows the equilibrium equation of motion for the external applied torsion. For the uncoupled case it would have only caused a torsional deflection κ_z . However, for the coupled case the applied torsional moment also has to contribute to the flapwise deflection of the blade. This results in a more negative torsional deflection than the uncoupled case. The relative increase in the torsional deflection results in an increase in the total pitch of the blade sections for the coupled part of the blade. The increased pitch in turn reduces the angle of attack, which leads to lower aerodynamic forces and moments. The total pitch angle of a blade section β is defined as the angle between the chord and the rotor plane and is given as the summation of the global blade pitch angle β_{pitch} , the fixed pre-twist of the section β_{twist} , the torsional deflection due to aerodynamic moments acting on the reference blade δ_z , and the induced torsional deformation θ . This relation is shown in Equation 4.9.

$$\beta(r) = \beta_{pitch} + \beta_{twist}(r) - \delta_z - \theta(r) \quad (4.9)$$

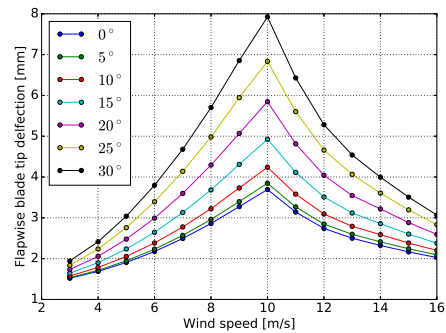
where r is the spanwise coordinate of the blade section. For positive values of the induced twist θ , the blade pitch is decreased resulting in an increased effective angle of attack and consequentially increased aerodynamic loads. This is termed as twist towards stall. Conversely, negative values of the induced twist will cause a decrease in the aerodynamic loads and is termed as twist towards feather. Hence, the aerodynamic bending and torsional moments acting on the various blade sections are reduced from their values obtained in the uncoupled case.

The flapwise blade root bending moments for the operational wind speed range are shown in Figure 4.7a and Figure 4.7c for carbon fibre and glass fibre blades, respectively. No visual change can be observed in the $M_x BR$ for the bend-twist coupled blades over the uncoupled case, for most wind speeds. However, a slight decrease in $M_x BR$ with increasing fibre layup angles is noticeable at the rated wind speed of 10m/s. The maximum value for $M_x BR$ is recorded at the rated wind speed. The reduction of the maximum $M_x BR$ relative to the uncoupled blade is visualised in Figure 4.8a, where a trend can be discerned. The relative reduction is greater in the carbon fibre blade than the glass fibre owing to the superior coupling factor of carbon fibre cross-sections. For both glass and carbon fibre blades the reduction in $M_x BR$ is seen to increase with rising fibre layup angles until they attain their maximum possible reduction. The carbon fibre blade attains a maximum relative reduction in $M_x BR$ of 2.8% at a fibre layup angle of 25°. As seen in Figure 4.5, this corresponds to the maximum coupling factor observed in the carbon-fibre cross-section at this angle. For the glass fibre blade the maximum relative reduction in $M_x BR$ of 1.1% is noticed for the fibre angle of 25°. Once again, it is seen from Figure 4.5 that this angle corresponds to the maximum coupling factor of the glass fibre cross-section. For angles above 25° the relative reduction in $M_x BR$ is seen to decrease in both carbon and glass fibre blades due to decreasing coupling strengths. A similar trend is also observed in the torsional moments shown in Figure 4.9. The relative reduction in $M_z BR$ is seen to attain its greatest value at 25° for both carbon and glass fibre blades. Once again, due to a high coupling factor, the reduction is more pronounced for the carbon-fibre blade than the glass-fibre blade.

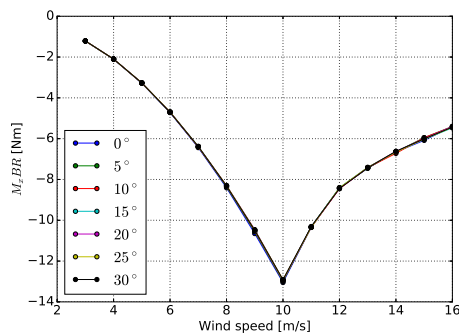
The flapwise tip deflections for the operational range of wind speeds is shown in Figure 4.7b and Figure 4.7d, for the carbon-fibre and glass-fibre blades, respectively. Their values are seen to increase with increasing fibre layup angles, corresponding to the decreasing magnitude of the flapwise bending stiffness. The highest value



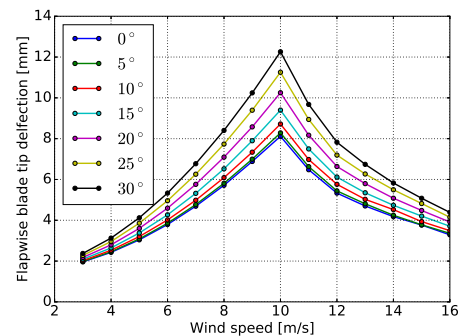
(A) Flapwise root bending moment for Carbon-FRP rotor



(B) Flapwise tip displacement for Carbon-FRP rotor

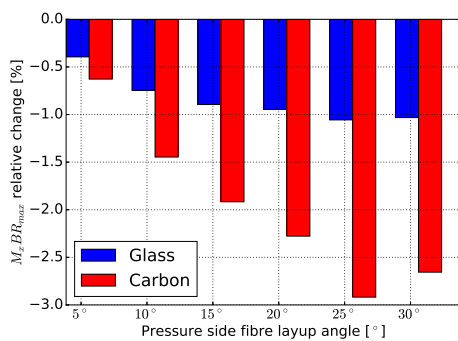


(C) Flapwise root bending moment for Glass-FRP rotor

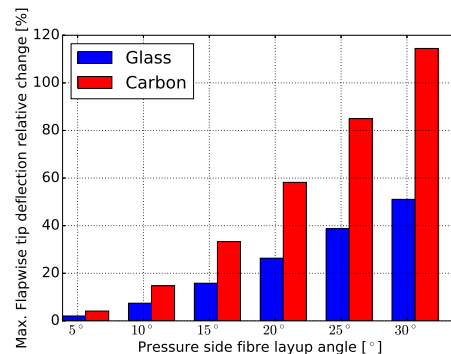


(D) Flapwise tip displacement for Glass-FRP rotor

FIGURE 4.7: Comparison between flapwise structural load and response for varying fibre layup angles

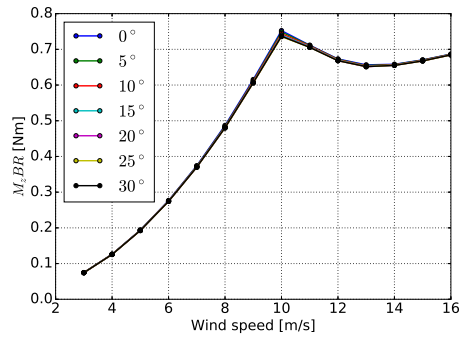


(A) Change in maximum flapwise root bending moment M_xBR_{max} at 10m/s rated wind speed

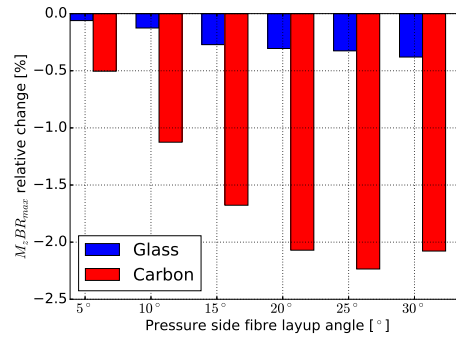


(B) Change in maximum flapwise blade tip displacement at 10m/s rated wind speed

FIGURE 4.8: Percentage change in flapwise loads and deflections with varying fibre layup angles, relative to the baseline

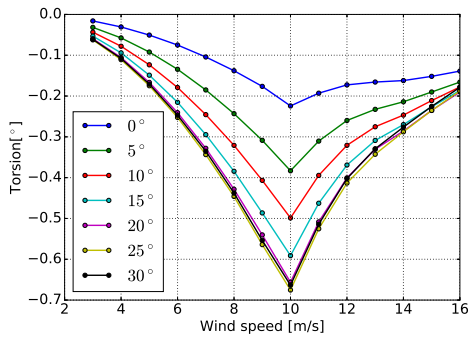


(A) Torsional moment M_z for carbon-FRP rotor for varying wind speeds

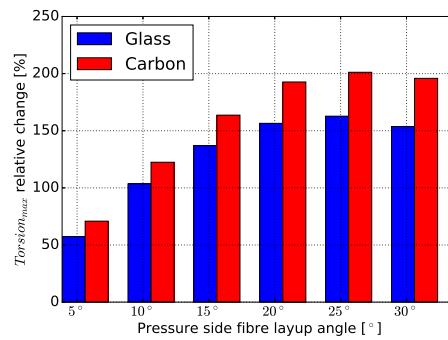


(B) Change in maximum torsional moment at 10m/s rated wind speed, relative to baseline

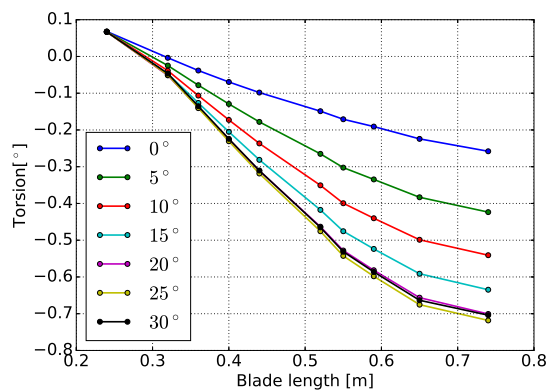
FIGURE 4.9: Torsional moment for varying positive fibre layup angles



(A) Torsional deflection for carbon-FRP rotor for varying wind speeds at 87% blade span



(B) Change in maximum torsional deflection at 10m/s rated wind speed, relative to baseline at 87% blade span



(C) Torsional deflection for carbon-FRP blade over span at 10m/s wind speed

FIGURE 4.10: Torsional deflection for varying positive fibre layup angles

of the tip deflection is attained for the upper limit of the fibre angle considered in this study, at 30°. The value of the tip deflection is lower for the carbon-fibre blade at 7.9mm than for the glass-fibre blade at 12.1mm. This is attributed to the higher values of the flapwise bending stiffness in carbon-fibre cross-sections. The value is higher even though the rate of decrease of flapwise bending stiffness with rising fibre layup angle is greater for carbon-fibre sections. This also explains the greater rise of the relative increase in tip deflection for the carbon-fibre blade in Figure 4.8b, than compared to the glass-fibre blade. The torsional deflections for the operational wind speed range measured at a spanwise location of 0.65m corresponding to 87% blade span are shown in Figure 4.10a for the carbon-fibre blade. A negative torsional deflection exists for the uncoupled case possibly as a result of the asymmetric cross-sectional profile being acted upon by shear forces. The torsional deflection is seen to attain increasingly negative values for rising fibre layup angles. However, the differences in their values attained for consecutive fibre angle decreases beyond 15°. This phenomenon is visualised from Figure 4.10b where the change in the relative increase of the torsional deflection is high for fibre layup angles of 15° and below. Whereas above 15° this rise is more gradual until the maximum relative increase in torsion is observed at a fibre angle of 25° for both glass and carbon fibre blade. Beyond this angle the relative increase in the torsional deflection with respect to the baseline gradually decreases. On closer inspection, the trend observed in the relative increase of the torsional deflection over the uncoupled case is seen to mimic the trend in the coupling factor change with increase fibre layup angles, as seen in Figure 4.5. Thus, the rise in the magnitude of the torsional deflection directly corresponds with the magnitude of the coupling factor for each fibre layup angle. The torsional deflection due to bend-twist coupling over the blade span at 10m/s wind speed is shown in Figure 4.10c. The blade is coupled from the 40% blade span location and onward. It is noticed that the absolute magnitude of the blade torsion increases with increasing blade length. This corresponds to a decreasing torsional and bending stiffness of the blade due to the lower values of chord and absolute thicknesses, as seen in Figure 3.9. Thus, the highest torsion is witnessed near the tip.

AEP and power

The annual energy production (AEP) is obtained for the wind climate expressed by the distribution plots in Figure 4.16a and Figure 4.16b. The given wind climate has an average speed $V_{avg} = 4m/s$ with almost no chance of occurrence of speeds above 14 m/s. This points to a low wind-speed climate with the turbine mostly operating in the region below the rated wind-speed $V_{rated} = 10m/s$. The AEP is calculated using Equation 4.10 shown below.

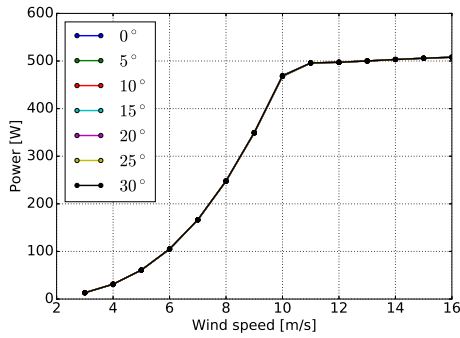
$$AEP = 8760 \cdot \sum_{i=1}^{N-1} \frac{P(V_i) + P(V_{i+1})}{2} (F(V_{i+1}) - F(V_i)) \quad ; V=3,4,5...15,16 \text{ m/s} \quad (4.10)$$

where the integer 8760 represents the total number of hours in a year, P is the power in W at wind speed V and F is the value from the CDF obtained for the wind speed V . Bend-twist coupling towards feather reduces the effective angle of attack causing a decrease in the aerodynamic forces and consequently the driving torque that is responsible for power generation. With increasing fibre layup angle and growing bend-twist coupling stiffness, a reduction in AEP caused by a decrease in the power production should be recorded. This phenomenon is expected to continue until the fibre-layup angle at which the bend-twist coupling stiffness peaks that is at

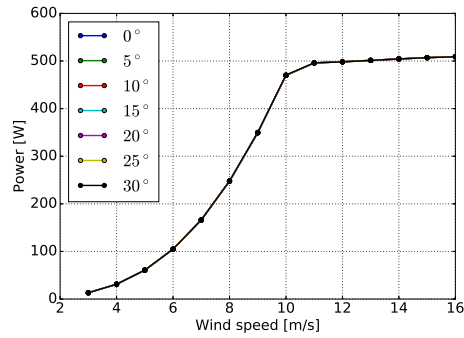
25°. However, the response of the current blade configuration to the applied aerodynamic loads presented a slight deviation from the expected behaviour. The calculated AEP values for the different fibre layup angles are shown in the Table 4.5.

TABLE 4.5: AEP for steady operation over varying fibre orientations

Fibre-layup angle	AEP Carbon-FRP[kW·hr/year]	AEP Glass-FRP[kW·hr/year]
0° (Baseline)	492.07	491.63
5°	491.67	491.24
10°	491.40	490.99
15°	491.29	490.92
20°	491.34	490.98
25°	491.55	491.19
30°	491.91	491.53



(A) Power curve for Carbon-FRP rotor



(B) Power curve for Glass-FRP rotor

FIGURE 4.11: Comparison between steady state power curves for varying fibre layup angles

The relative change in the AEP for the different fibre orientations when compared to the baseline case is shown in Figure 4.12. It is seen from both Table 4.5 and Figure 4.12 that the AEP does not decrease as expected with increasing fibre-layup angles. The relative reduction is greatest for a fibre layup angle of 15° and the value decrease with the ascending magnitudes of the remaining higher angles. The values are almost identical with relative change on the order of $10^{-2}\%$, which is small enough to be ignored. Any trend seen in Figure 4.12 has to be discounted and attributed to the possibility of numerical errors in the simulation due to non-deterministic nature of HAWC2 simulations. The absence of change in AEP stems from the identical power curves noticed in Figure 4.11a and Figure 4.11b with varying fibre-layup angles for carbon and glass-FRP blades respectively. The power generated by the wind turbine is produced by the aerodynamic torque acting on the blades in the rotor plane, which in turn is generated due to the radial integration of the tangential force F_t acting on each blade element. This tangential force is given by Equation 4.11 shown below.

$$F_t = (Cl\sin(\phi) - Cd\cos(\phi)) \cdot \frac{1}{2}\rho V_{rel}^2 \bar{c} dr \quad (4.11)$$

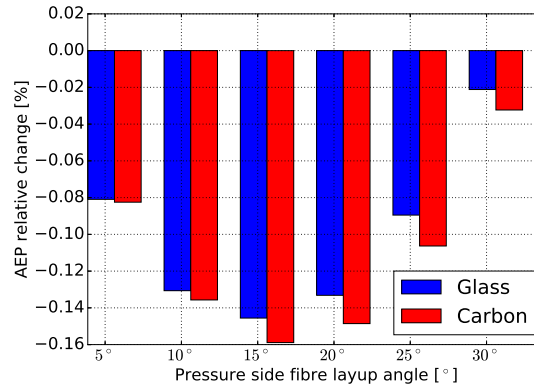


FIGURE 4.12: Percentage change in AEP with varying fibre layup angles, relative to the baseline

where C_l and C_d are the lift and drag coefficients of the airfoil used in the blade section, ϕ is the inflow angle, ρ is the air density, V_{rel} is the velocity of the oncoming wind relative to the rotating turbine blade, \bar{c} is the sectional chord, and dr is the elemental length of the blade section. In Equation 4.11 it can be seen that the tangential force vis-à-vis the power, are mainly dependent on the flow angle ϕ and the lift and drag coefficients, C_l and C_d provided steady inflow conditions and a constant blade profile. The relation for the flow angle ϕ is obtained from the velocity triangle and is given by Equation 4.12 shown below.

$$\phi(r) = \text{atan} \left(\frac{(1-a)R}{1+a'\lambda_{tip}r} \right) \quad (4.12)$$

$$AoA = \phi(r) - \beta(r) \quad (4.13)$$

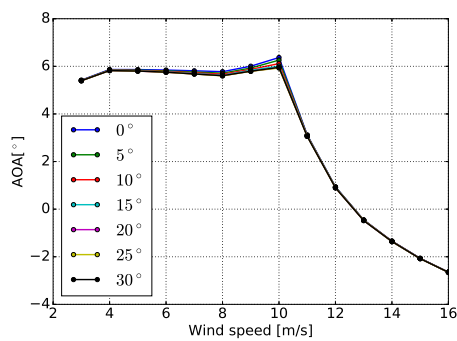
where a and a' are the axial and tangential induction factors, R is the rotor radius, r is the distance to the blade element from the rotor centre and λ_{tip} is the tip speed ratio, AoA is the angle of attack and β is the total sectional twist angle. It is important to note that the flow angle ϕ is determined by the inflow conditions as seen in Equation 4.12. Whereas, the angle of attack experienced by the blade section is defined by Equation 4.13 and depends on the flow angle and the total sectional twist angle. For a variable speed rotor such as the present case, the tip speed ratio λ_{tip} is maintained at a constant value in the partial load region below the rated wind speed, resulting in a constant flow angle for a blade section. Thus, the angle of attack experienced by the airfoil will mainly be affected by the local twist angle. It was seen in Equation 4.9, that the local twist angle depended on the global pitch, pre-defined twist, the deformation due to pitching moments for the steady case and the deformation produced by the bending-torsion coupling, of which the former are constant in the partial load region. Thus, the main variation in the total sectional twist for the partial load region is due to the deformation produced by bend-twist coupling. As the flow angle depends on the tip speed ratio and remains constant in the partial load region, any change in the angle of attack is directly a result of the BTC deformation θ . In the current configuration, the blade is coupled such that application of bending loads causes it to twist towards feather increasing the local sectional twist. From Equation 4.13, it can be seen that any increase in $\beta(r)$ will lead to a reduction in the angle of attack AoA .

However, since the flow angle remains constant in the partial load region it would not affect the tangential force. As a consequence it would not result in a deviation from the power produced in the baseline case. But, the tangential force is also dependent on the aerodynamic lift and drag coefficients, Cl and Cd . For a variable speed rotor the airfoils chosen for the power producing middle and outboard sections of the blade are carefully designed targeting a specific optimal angle of attack AoA_{design} that produces the best aerodynamic performance Cl/Cd for the design tip speed ratio. Thus when operating at the design tip speed ratio with the flow incident at the design angle of attack, the rotor will produce its maximum power. A decrease in the angle of attack from AoA_{design} causes a drop in the value of the lift coefficient Cl and hence the tangential force F_t , which as gathered from Equation 4.11 is directly proportional to the value of Cl .

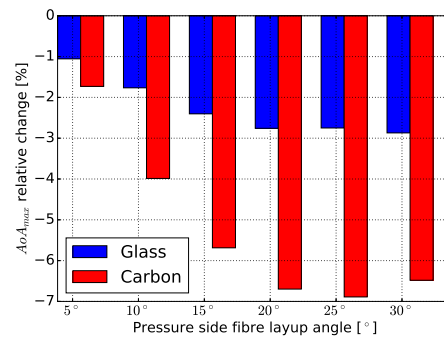
In summary, the torsional deformation θ induced by the bend-twist coupling increases the total sectional twist angle, decreasing the angle of attack AoA which causes a reduction in the lift coefficient, decreasing the tangential force from the uncoupled case. This in turn affects the power produced and results in a lower AEP. The bend-twist coupling does cause a decrease in the angle of attack from the uncoupled case as seen in Figure 4.13b, where the relative decrease in the maximum angle of attack is shown for each fibre layup angle. The maximum angle of attack is seen to occur at the rated wind speed of 10m/s. The greatest relative decrease of 6% in AoA occurs at the maximum coupling angle of 25° for the carbon fibre blade, while a smaller decrease of 2.7% similarly occurs at its maximum coupling angle of 20° for the glass fibre blade. However, as seen in Figure 4.13a, this decrease is small enough for the wind speeds in the partial load region to ensure that the angle of attack remains near its design point AoA_{design} . The angle of attack variation over the blade span at 10m/s wind speed is shown in Figure 4.13c. It is seen that with increasing blade length the difference in the angle of attack of the uncoupled blade and at a positive fibre layup angle increases with span. With increasing fibre layup angle the angles of attack are seen to decrease by greater magnitudes relative to the baseline case with greater spanwise locations. This is attributed to the increasing magnitudes of torsional deflection towards feather with increasing spanwise location, as seen in Figure 4.10c.

The design angle of attack for the blade was chosen as $AoA_{design} = 5^\circ$. The aerodynamic efficiency of this airfoil given by the lift-to-drag ratio is shown in Figure 4.15b, which is seen to be most efficient at an angle of attack in the range of $5^\circ - 6^\circ$. Thus in this range the airfoil produces the highest aerodynamic force which is translated into a high power coefficient C_p for the rotor blades. Figure 4.13a shows that the normal point of operation obtained from the steady aero-elastic simulations is close to $AoA_{oper} = 5.5^\circ$, which is still in the most efficient region of the airfoil. The decrease in lift coefficient Cl for the corresponding decrease in the angle of attack is not sufficient enough to cause a substantial deviation from the power produced in the baseline case. The lift coefficient over the range of operational wind speed measured at 87% spanwise location is shown in Figure 4.14a. It is seen that the greatest decrease in the Cl as a result of BTC towards feather is noticed at the rated wind speed of 10m/s. For the remaining wind speeds in the partial load region the decrease in the Cl is smaller. The relative reduction in the lift coefficient also increase in absolute magnitude with increasing fibre layup angles until it peaks at 25° . At this point carbon-fibre and glass-fibre blade sections experience their greatest coupling

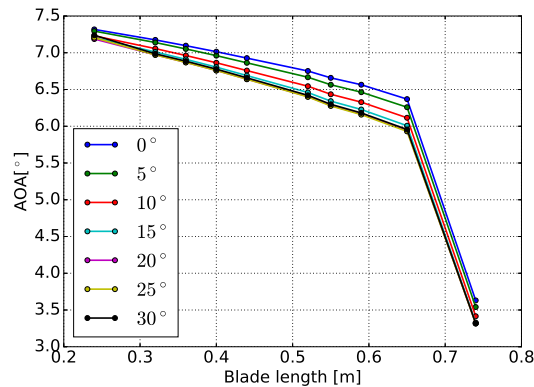
strength. Beyond this point the magnitude of the relative reduction decreases. At 25° carbon-fibre blade records a relative reduction of 4.1%, while the relative reduction in the glass-fibre blade is considerably lower at 1.6%. The spanwise distribution of the lift coefficient at a wind speed of 10m/s is shown in Figure 4.14c. The trend is similar to that observed for the spanwise distribution in the angle of attack. It is also clear that even for the greatest of reductions in the lift coefficient, its value still remains in the vicinity of the design lift coefficient of 0.9. This translates in a minuscule reduction in power at best. The lift polar for the SD-7032 airfoil is shown in Figure 4.15a. Since the given wind climate has a low mean wind speed of 4m/s, the small decrease of the angle of attack in the vicinity of this wind speed results in the marginal decrease in AEP witnessed over the different fibre-layup angles.



(A) Angle of attack AoA for carbon-FRP blade over wind speed range at 87% blade span



(B) Change in AoA_{max} relative to the uncoupled case for 10m/s wind speed, at 87% blade span

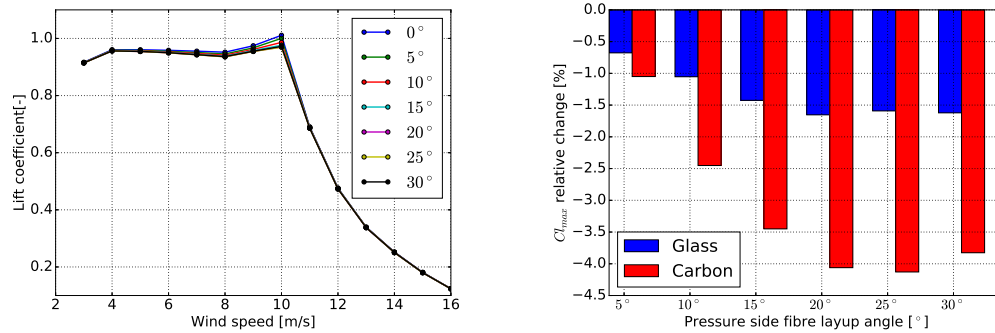


(C) Angle of attack AoA for carbon-FRP blade over span at 10m/s wind speed

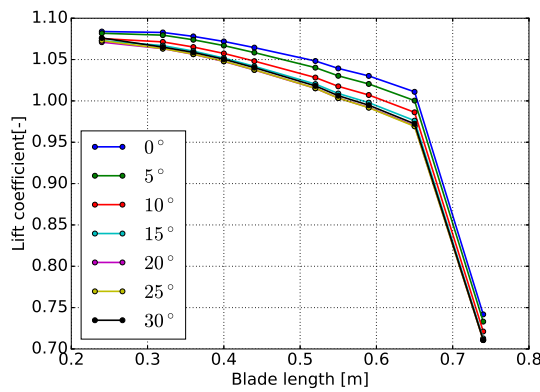
FIGURE 4.13: Angle of attack AoA for varying fibre layup angles

4.2.2 Summary

The load response of the rotor was presented for steady wind conditions in the operating range from $V_{cut-in} = 3m/s$ to $V_{cut-out} = 16m/s$ in section 4.2.1. The fibre-layup angles were varied from 0° to 30° with an increment of 5° , such that the bending of

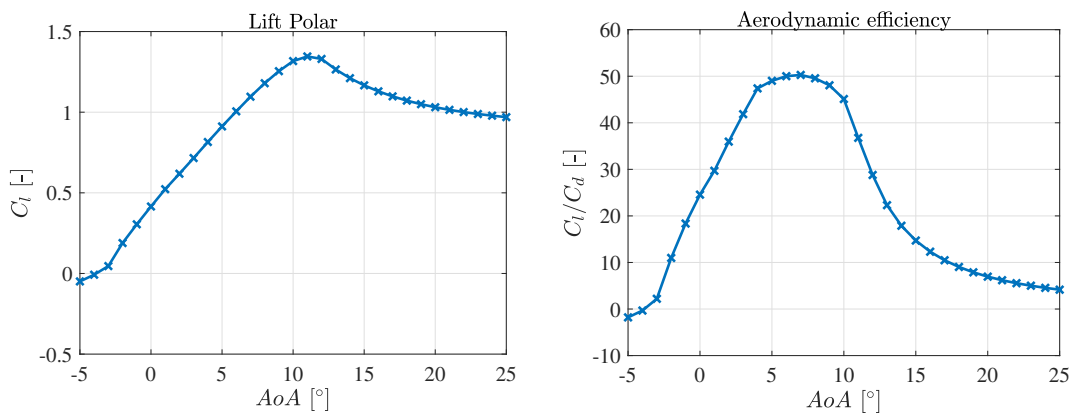


(A) Lift coefficient Cl for carbon-FRP blade over wind speed range at 87% blade span (B) Change in Cl_{max} relative to the uncoupled case for 10m/s wind speed, at 87% blade span



(C) Lift coefficient Cl for carbon-FRP blade over span at 10m/s wind speed

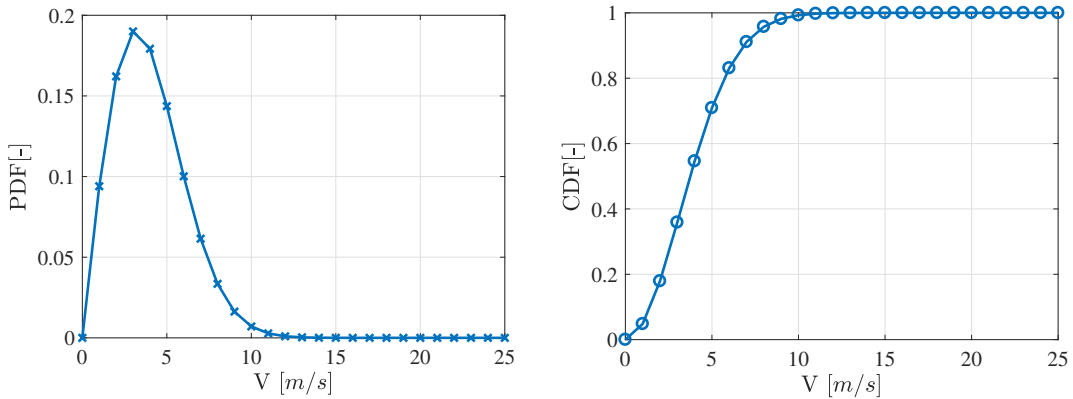
FIGURE 4.14: Lift coefficient Cl for varying fibre layup angles



(A) Lift coefficient over angles of attack

(B) Lift-to-drag ratio over angles of attack

FIGURE 4.15: Aerodynamic coefficient curves for SD-7032 airfoil



(A) Weibull pdf for parameters $A=4.5\text{m/s}$ and $k=2$ (B) Weibull cdf for parameters $A=4.5\text{m/s}$ and $k=2$

FIGURE 4.16: Wind speed distributions for the given wind climate

the blade produced a torsional deflection towards feather. An increase in the flapwise blade tip displacement and a reduction in the flapwise bending loads with increasing fibre-layup angles was noted for both glass-fibre and carbon-fibre blades. It was also observed that absolute change in the flapwise loads over the different fibre angles was negligible. This trend was also seen in the AEP in section 4.2.1 which also showcased negligible difference over variations in the fibre layup angles. The reason was that both parameters are affected by the same underlying phenomenon of a small decrease in the angle of attack. The reduction in the angle of attack was not large enough to push the aerodynamic performance of the airfoil below its optimal design range. Thus, although there was a decrease in the aerodynamic forces it was too small to have a profound effect on flapwise load reduction.

It is predicted that decreasing the flapwise bending and torsional stiffness of the blade will make it more responsive to the aerodynamic loads and thus may result in larger induced torsional deformations and consequently higher load reductions. The increased magnitudes of the torsional deflections with decreasing flapwise bending and torsional stiffnesses over the blade span was already witnessed. This decrease was due to the reduction in chord over the blade span. The stiffness scales linearly with the skin laminate thickness and a reduction would also result in lighter and consequently cheaper design. However, they are currently set at the minimum manufacturing limit of 1mm throughout the blade. Another method would be to increase the fibre-layup angle further so as to decrease the flapwise bending stiffness. This would however also be accompanied by a decrease in the bend-twist coupling factor.

Chapter 5

Multidisciplinary Optimisation

This chapter presents the results of the multidisciplinary optimisation (MDO) carried out on the reference blade finalised in chapter 4. The aim of the optimisation is to obtain the best possible spanwise distribution of fibre layup angle and laminate thickness with the objective of minimising the aerodynamic loads while at the same time reducing the AEP by a marginal amount. The case for optimisation for incorporating BTC in the 500W turbine is made in section 5.1. Next, the multidisciplinary optimisation framework, the workflow of the aero-structural optimisation and the tools used are briefly described in section 5.2. This is followed by a description of the optimisation problem itself including the objective function, the design variables and the constraints, and the cases set up for optimisation in section 5.3. In section 5.4 the results of the optimisation are presented and discussed. Next, the challenges faced during the optimisation of the 500W small wind turbine are discussed in section 5.5. Based on this discussion recommendations are made in section 5.6 to ensure a successful MDO and enhanced BTC in the 500W turbine blades. The chapter is concluded with a summary.

5.1 Case for optimisation

The parametric studies conducted in chapter 4 analysed the various aspects of introducing bend-twist coupling in a 0.75m long wind turbine blade designed to generate a rated power of 500W. The interplay between stiffnesses of the blade sections, the geometry of the profile, the applied aerodynamic loads and the appropriate spanwise location to begin coupling showcased the complexity involved in incorporating BTC in design. Although BTC as a phenomenon and its resulting benefits to load reduction have been investigated by the wind energy research community and industry alike (as presented in section 2.2), its application to small wind turbines and the new challenges that arise as a consequence have not been adequately addressed. It was seen in chapter 4 that for the 500W turbine with the small rotor swept area of $2m^2$, the high values of the flapwise bending and torsional stiffnesses stifled any reductions in the steady state loads. The decrease in the angle of attack from the uncoupled case was simply not great enough to bring about a significant decrease in loads.

In this context, small wind turbines of this scale require a higher degree of precision in implementing BTC than that can be achieved from parametric studies alone. A precise implementation of BTC would make it possible to achieve the greatest possible reduction in loads leading to an improvement of the fatigue strength and operational life of the turbine, reduce the aggressive behaviour of the controller and the corresponding pitch actuation effort, and result in decreased mass of the rotor due to lower bending and torsional stiffnesses. The wind turbine design problem is

already of a multidisciplinary nature with aerodynamics, control and manufacturing playing a various degrees of decisive roles in the process. In this scenario, the multiple interdependencies of design variables further complicate the process. Additional interdependencies arise with the implementation of BTC. Only a multidisciplinary optimisation approach to design can successfully negotiate the numerous design variables to extract the best possible bend-twist coupled design. As highlighted in section 2.2, the benefits in designing wind turbines through optimisation have been recorded by Bottasso et al. [10], [9], Ning et al. [39] and Zahle et al. [52]. However, these studies were performed on multimewatt turbines with only Bottasso et al. [10] implementing BTC.

For the small wind turbine studied in this thesis, such an multidisciplinary optimisation approach is applied to the implementation of BTC with load minimisation as the main design driver. The utilised optimisation tools and work-flow is based upon the study by Zahle et al. [52], [51] on the DTU 10MW turbine.

5.2 Optimisation framework and work-flow

The HAWTOpt2 [51], [52] aero-structural design tool developed by DTU Wind Energy is utilised to implement the optimisation of the 500W small wind turbine. This tool encompasses the FUSED-Wind optimisation framework [40], which itself has been extended from NASA's open-source OpenMDAO v1.x [18] multidisciplinary optimisation framework for adoption specifically to wind turbine design. The OpenMDAO framework handles the workflow and dataflow within HAWTOpt2 and allows for implementation of parallel simulation cases and numerical methods. It adopts a modular structure of data flow, enabling isolated model development and making them easier to build and maintain [37]. OpenMDAO and its extension FUSED-Wind are both built in the Python programming language. HAWTOpt2 basically consists of python libraries, modules and packages from OpenMDAO and FUSED-Wind, with in-house developed wrapper codes to interface with external solvers for the numerous wind turbine design phases. An example of this structure is shown in Figure 5.1. These external solvers have a high likelihood of being written in a programming language other than Python. Due to the open source nature of Python, there exists numerous packages to interface with a variety of other development languages [14]. For example, two of the interfaced design tools in HAWTOpt2, HAWC2 and BECAS, are programmed in the FORTRAN [41] and MATLAB programming languages respectively.

5.2.1 OpenMDAO

MDAO (Multidisciplinary Design Analysis and Optimisation) involves optimisation of complex systems consisting of numerous individual models that have interdependent relationships and thus are said to be coupled. A solver is required to correctly interface and govern the data flow between these models in order to find a converged solution. OpenMDAO provides the framework to enable the flow of data and the solvers to find a converged solution at the system level. It uses analytic multidisciplinary derivatives to compute system-level gradients for the gradient-based optimiser. If analytic derivatives aren't provided it produces numerical finite difference derivatives [37]. In the present context, OpenMDAO works with the gradient-based interior point optimiser IPOPT [50] which is interfaced through the wrappers in PyOptSparse [43], which is a Python-based package for nonlinear optimisation.

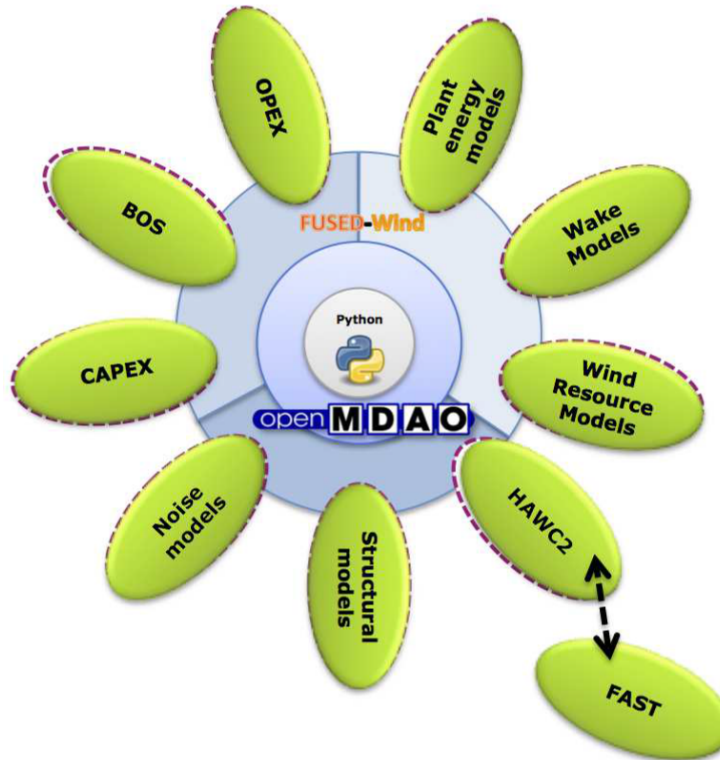


FIGURE 5.1: HAWTOpt2 internal structure with OpenMDAO and FUSED-Wind core and interfaces to external models [17]

OpenMDAO defines the multidisciplinary problem using three constructs, namely *System*, *Component* and *Group*. Complex systems with coupled models are represented in OpenMDAO by systems of non-linear equations in a hierarchy set by the system model [38]. The *System* class consists of a system of explicit or implicit equations that need to be solved either analytically or numerically to find the unknowns. *Component* and *Group* are sub-classes of the *System* class and are used to define the model. The *Component* class is at the lowest level in the hierarchical structure of OpenMDAO. Its sub-classes are the only classes allowed to create the variables necessary to define the model and create wrappers for external analysis codes. Additionally, analytic derivatives for the model defined in the *Component* can also be specified, assisting in speeding up the computation by avoiding finite difference to compute derivatives. Finally, the *Group* construct is used to develop complex models from the individual models defined using *Component*. A group essentially limits the scope of the data generated by a model to within its scope. The data flow between two different *Components* within a group can be established by either implicitly or explicitly defining a link between the variables, for example between output of one model and input of another. A *Group* can have several sub-groups with each having their own sub-groups and components nested within each other. Dataflow can be achieved between the nested groups and components across the various levels of the defined hierarchy of the model. So in essence, a *Group* is responsible for assembling different system of equations defined by the *Components*, and solving them together to obtain a converged solution. Whereas a *Component* is only responsible for defining the systems of equations and the variables.

Once the complex model has been defined by a *Group* consisting of various *Components* and *sub-Groups*, a *Problem* construct is set-up that contains the entire model

with its coupled relationships. *Problem* is at the highest level in the OpenMDAO hierarchy and has a corresponding top-level *Group* called *root*, and a *Driver* that is responsible for executing the model in a particular way and controlling the solution. Analyses, experiments and optimisation on the complex system are carried out through the *Problem* instance.

An in-depth explanation of the various structures in OpenMDAO along with detailed examples can be found in the official documentation [38].

5.2.2 HAWTOpt2 work-flow

HAWTOpt2 has been briefly introduced in the beginning of section 5.2. In this section the workflow is explained in the context of the optimisation that was implemented in this thesis.

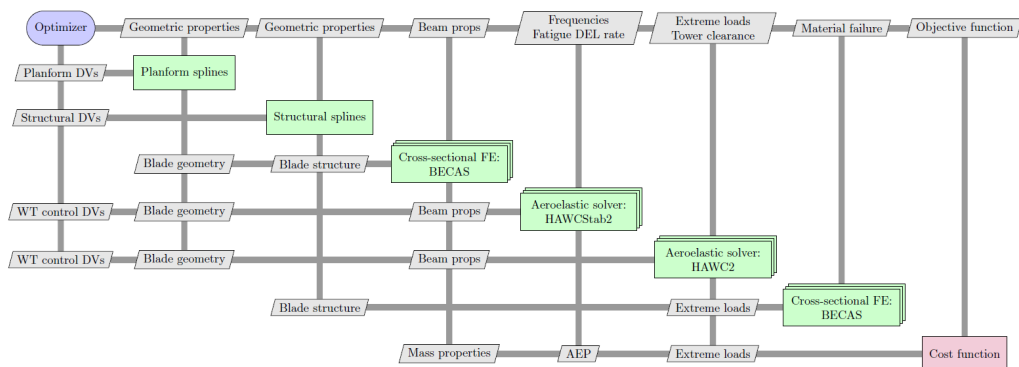


FIGURE 5.2: HAWTOpt2 workflow [52]

The extended Design Structure Matrix diagram (XDSM) [27] of the workflow in HAWTOpt2 is shown in Figure 5.2. The overlapping boxes in Figure 5.2 indicate the parallel executions of each blade cross-section in BECAS and load case in HAWC2. The various components with brief explanations on their role are listed.

FUSED-Wind

The Structural Splines and Planform Splines shown in Figure 5.2 form a part of the FUSED-Wind extension to OpenMDAO. Three different spline types, namely Bezier, linear and P-chip are included. The planform and structure properties that are added as design variables of the optimisation problem are manipulated by attaching the chosen spline at different positions along the blade span. These positions are the spline control points (CPs) and they encompass the properties of the chosen spline. During the gradient-based optimisation these spline control points are perturbed from zero by a bounded magnitude. The lower and upper bounds of the chosen planform and structure design variables, further subjected to constraints, are specified and translated into the bounds by appropriately scaling them. The magnitudes of the perturbed splines are then multiplied by their respective scalars and reflect the change in the value of the corresponding structure and planform design variables. The summation of this change and the original values of the design variables then provides the new distribution of those structure and planform design variables over the blade span. An example of structural perturbation for the thickness of a spar cap for the DTU 10MW wind turbine by a linear spline is shown in Figure 5.3. The

spline control points are represented by the red dots. A small perturbation 0.01m is added only to the control point at the 40% spanwise location. The corresponding design variable value is also perturbed by the same amount as seen by the final spar cap thickness at the same spanwise location, which is increased by 0.01m and has a value of 0.05m. The blue dotted line represents the linear spline. The spar thickness between the perturbed control point and the unperturbed ones are increased according to the distribution provided by the spline.

The design variables and constraints in the context of the optimisation in this thesis is described in section 5.3.

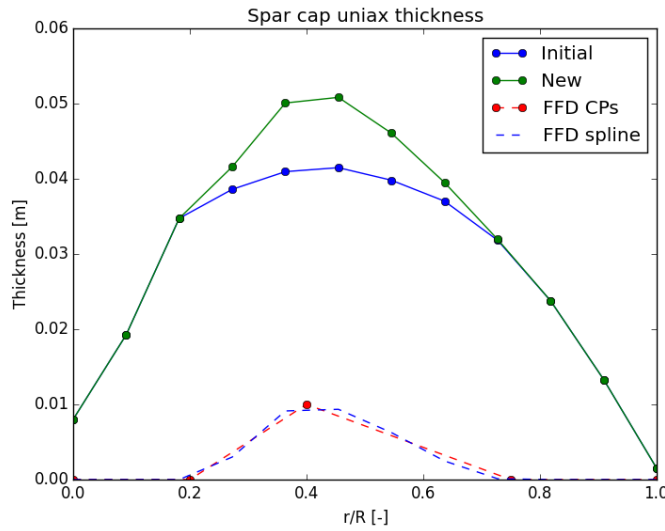


FIGURE 5.3: Thickness perturbation for the blade spar-cap of DTU 10MW wind turbine [40]

BECAS

The altered platform and structure variables establish a new definition of the blade geometry and internal structure. This information is then passed on to BECAS. BECAS evaluates the cross-sectional stiffness and mass properties of the blade. It also allows for calculation of the material failure with respect to the ultimate and fatigue loads.

Bend-twist coupling is possible due to the anisotropic properties of the composite laminates used in the blade. Thus, in order to facilitate the analysis of the blade with the inclusion of bend-twist coupling, a fully populated stiffness matrix at each of the specified blade sections is generated, along with important information regarding the location of the centre of gravity, shear centre locations, elastic centre locations and mass distribution.

HAWC2

HAWCStab2, in its current version, lacks functionality to evaluate anisotropic structural properties of blades. Thus, this step in the workflow is skipped since it would not be able to capture the changes in the response of the structure due to the inclusion of bend-twist coupling.

HAWC2 consists of a geometrically non-linear Timoshenko finite beam element structural model, and an unsteady BEM including effects of shed-vorticity, dynamic

stall and dynamic inflow [29]. Time domain load simulations are carried out using the aero-hydro-servo-elastic tool HAWC2. Although initially these simulations were to be carried out on a full design load basis described in IEC 61400-2 [46], it was later decided to first perform the optimisation cases using only the ultimate analysis part of the DLC1.1 case from the standard. The DLCs with turbulence have been neglected for the optimisation cases for reasons made clear in section 5.3.

Only after obtaining promising results with DLC1.1 would the design load basis be extended to include the rest of the DLC cases namely DLC1.2, DLC1.3, DLC1.4, DLC1.5, DLC2.2, DLC2.3, DLC3.1 and DLC3.2. This decision was taken due to a combination of limited computational resources on the cluster and constraints imposed by the restricted time-frame of this project. The cluster resources were limited because a small time-step had to be used per iteration of a HAWC2 simulation. The time step could not be longer than 0.003s due to the high rotational speed range of 181rpm - 604rpm of the wind turbine. At a time step of 0.003s the aero-structural response would be calculated for an azimuthal resolution range of 3.26° - 10.8° for the rotational speed range of 181rpm - 604rpm. This time-step corresponds to a 40-60 minute real simulation time per case depending on the number of iterations it would take to find the aero-structural solution per each time-step. A design load basis including all the DLC cases mentioned earlier would entail 124 cases. Since the HPC is a resource shared by countless researchers from different departments at DTU, students were advised not to use more than 5 computing nodes. The problem in this thesis has 17 structural blade sections. Keeping in line with the parallel computing nature of the problem, it is recommended not to use processes greater than the number of structural sections per each node. Thus, at maximum 85 processes would be available at a given time. HAWC2 executes the simulation serially, leading to the execution of a single case on a single processor. Depending on the number of processes employed on the cluster to carry out these simulations, a complete once-run of the 124 cases would take between 2.5 hours - 3 hours of real time. For an optimisation problem, a number of iterations have to be run in order for the solution to start converge. Along with the solution time taken by the gradient-based solver to compute the finite difference gradients and evaluation of the objective functions, each new iteration of the optimisation also includes a complete regeneration of the blade planform and structure, calculation of the structural properties in BECAS followed by the simulation cases in HAWC2. For a design load basis of 124 cases this would be unfeasible. From experience it would take approximately 48 - 72 hours for just 15 to 20 iterations of the optimiser. The cluster also limits the maximum computing time to 72 hours per job. After starting the optimisation with the full DLB, the compute times were placing constraints on error redressal and debugging. In lieu of this, the decision to initially optimise for only DLC1.1 was taken. It is important to note that except for the HAWC2 time-step and azimuthal resolution values, the cluster compute times are averages through visual inspection. A detailed study with respect to the average compute time was not performed. Thus these numbers are only indicators and accordingly the range of variation offered is quite large.

The resulting ultimate load envelopes obtained from HAWC2 are utilised as input to BECAS to perform a failure analysis and obtain the blade failure index for the blade. The blade pitch angle and the rotor speed range can be utilised as control design variables in the optimisation. Other data representing the aero-structural response of the turbine, including the maximum blade tip displacement, the maximum and minimum flapwise, edgewise and torsional moments, the thrust force, the tower bottom and tower top out-of-plane and in-plane moments, the steady state

power curve and the resulting AEP, and the aerodynamic lift coefficients of the blade sections may be utilised as operational design constraints and to define the cost function for the optimisation. The cost function used in the current thesis is defined in section 5.3.

5.3 Problem setup

In this section the nature of the optimisation cases are specified including a description of the objective function, design constraints and design variables for the chosen cases.

5.3.1 Objective function

As mentioned in section 5.2, the optimisation being carried out using HAWTOpt2 utilises a gradient based optimiser. Since gradient based optimisers rely on the first derivatives or the slopes of the variables, introduction of randomness or noise in the variables is not conducive to their success. Thus, turbulent cases are not utilised in the optimisation process, especially in the time-domain. As a result, fatigue loads affecting the turbine cannot be used either as constraints or in the objective function. Instead, the optimisation utilises extreme loads in the objective function and also as constraints. As was seen through the parametric studies in chapter 4, flapwise BTC reduces the flapwise bending moment by decreasing the effective angle of attack leading to a decrease in the aerodynamic forces. The aerodynamic lift force is the largest contributor to the thrust force which in turn is responsible for the flapwise bending moments. Thus, a decrease in the aerodynamic lift force would have the greatest reduction in the flapwise bending moment compared to the edgewise bending moment which is governed primarily by the influence of gravitational forces. Thus, flapwise bend-twist coupling would also cause the greatest reduction in the flapwise fatigue loads. In lieu of that, the maximum flapwise bending load is considered for minimisation in the objective function. The hypothesis for this thesis was presented in chapter 1 and is restated here.

Hypothesis: Material bend-twist coupling is an effective means to substantially decrease the aerodynamic loads in a small wind turbine blade with only a marginal decrease in AEP.

The above hypothesis has been proven for large kilo-watt and multimegawatt wind turbine blades in various studies as witnessed from the literature review presented in section 2.2. Based on this information it is decided to have an objective function that does not rely only on reduction in the loads and inevitably resulting in a subdued power production. Accordingly, an objective function is considered in Equation 2.5 consisting of two weighted objective functions. These part objective functions include maximising the AEP and the simultaneous minimisation of the flapwise root bending moment (M_xBR) relative to the uncoupled blade. Equation 2.5 is reproduced for convenience in Equation 5.1.

$$C = - \left(f \cdot \frac{AEP(\{x_p, x_s, x_{oper}\}, p)}{AEP(\{0, 0, 0\}, p)} + (1 - f) \cdot \frac{M_xBR(\{0, 0, 0\}, p)}{M_xBR(\{x_p, x_s, x_{oper}\}, p)} \right) \quad (5.1)$$

where C represents the cost function, AEP is the annual energy production, M_xBR

is the flapwise blade root bending moment, f is the weight given to the aerodynamic and structural parameters that determines the trade-off, x_p are the collection of the blade planform design variables, x_s is the collection of the blade structural variables, x_{oper} is the collection of wind turbine control variables and represents the variables that are kept constant. $AEP(\{0, 0, 0\}, p)$ and $M_x(\{0, 0, 0\}, p)$ represent the AEP and the flapwise root bending moment for the baseline uncoupled rotor. The weight f is to be varied from 0 to 0.4 with an incremental step of 0.1. At $f = 0$ the cost function is entirely dependent on the minimisation of $M_x BR$ relative to the uncoupled blade with no regard to the AEP. At $f = 0.4$, the objective function would have a 60% dependence on the minimisation of the $M_x BR$ and a 40% dependence on maximisation of the AEP.

However, the steady load response parametric study in section 4.2 showed that even for the strongest of bend-twist couplings the flapwise bending moment decrease was only marginal with almost no change observed in the AEP. Thus, this could be regarded as an indicator that the solution obtained through the multidisciplinary optimisation would show only a marginal decrease in the AEP for the best case scenario. If such a situation arises, then the dependence of the objective function on maximising the AEP could be counter-productive for the given design variables and constraints. In this regard, it is decided that the weight factor f would be initially set at zero. An increase in the f would only be considered for the objective function if for $f = 0$ the optimisation results would contain a reduction in AEP that is 5% or more.

5.3.2 Optimisation cases

For various reasons stated early on in this report, the small wind turbine in this thesis has been designed to have a rated power of 500W with a maximum rotor radius limited to 0.79m. The rated power, range of the rotational speed and the tip speed ratio were selected based on the limitations of the Small Wind Turbine Competition and with the ultimate goal to win the competition with the highest AEP produced in the specified wind climate. As can be gleaned from the hypothesis, the goal of this thesis is to establish the effectiveness of implementing bend-twist coupling in an existing small wind turbine blade. Thus, the 500W small wind turbine was considered a good candidate to investigate the benefits, if any, of implementing BTC in small wind turbine blades where the aerodynamic design and operational parameters are fixed. Changes could only be made to the structural design space to realise this goal. Implementing material bend-twist coupling over a geometric coupling through blade sweep, would save blade manufacturing costs as the mould used for the uncoupled blade could be reused for the bend-twist coupled design. The only changes would be in the material of the laminate, the laminate thickness and the fibre layup angle. In this regard, the multidisciplinary optimisation problem in this thesis is focused on optimising the structural parameters that can lead to an effective implementation of material bend-twist coupling.

Two optimisation cases are setup to carry out the implementation. In the first case the laminate thickness is maintained at the minimum limit of 1mm imposed by manufacturing constraints, while the fibre layup angles are allowed to be varied by the optimiser. A variation of this case is also setup, where only the optimisation constraints are altered. In the second case, both the laminate thickness and the fibre layup angles are allowed to be varied by the optimiser. In all these cases the planform variables x_p including the twist, chord, distance of the pitch axis from the leading edge, relative thickness distributions and rotor precone are considered as

constants for the optimisation. The control variables in blade pitch angle and the rotor speed range are also considered as constants. A tabulated list of the optimisation problem with the design variables and constraints for all the cases are provided in subsection 5.3.3.

5.3.3 Design variables and constraints

Case 1

The problem formulation for the aero-structural optimisation of the 500W blade maintaining the laminate thickness at the minimum manufacturing limit of 1mm is given in Table 5.1. The definition of the objective function $C(\{0, x_s, 0\}, p)$ has been provided in Equation 5.1. The fibre layup angle in the unidirectional carbon fibre laminae in the pressure side and suction side skin of the blade sections are subjected to upper and lower bounds of $\pm 30^\circ$. Since the fibre layup angle is a structural design variable varying with blade span, a free form deformation (FFD) spline has been assigned to it. The spline control points are located at the normalised spanwise locations given by [0.4, 0.6, 0.8, 1.0]. In other words at 40%, 60%, 80% and 100% spanwise locations of the blade. Each of this control point represents a separate instance of a design variable for the fibre layup angle that is altered during the optimisation. The locations of the span that lie in between these control points obtain values defined by the spline distribution. A linear FFD spline has been assigned to the fibre layup angle on both the pressure and suction side skins of the blade sections. This results in a total of 8 design variables.

The flapwise blade root bending moment $M_x BR$ for every design load case is constrained to an upper limit set by the maximum flapwise blade root bending moment in the uncoupled reference case. This maximum value is obtained with respect to the set of maximum values of $M_x BR_{ref}$ for all three turbine blades. The upper limit of the $M_x BR$ constraint is however relaxed by 2%. This relaxation is intended to account for non-deterministic nature of the results obtained from the aero-elastic simulations performed by HAWC2. The results of two HAWC2 simulations with the exact same conditions are seen to show some variations and do not end up with the exact same value. This issue is known to the developers of HAWTOpt2 [52] at Technical University of Denmark, Risø and the relaxation values chosen for the constraints have been selected in consultation with them.

The thrust force acting on the rotor T at each wind speed is constrained to an upper limit specified by the maximum thrust force on the uncoupled case, and has been relaxed by 2%. Similarly, the tower bottom fore-aft moment $M_X TB$ for every design load case simulation is also constrained with an upper bound set by the maximum value in the uncoupled reference case, relaxed by 1%. The final constraint is the material failure index or the ultimate strain criteria. Its upper bound is set at 1. An increase of the material failure index above this value for any of the blade structural sections leads to ultimate failure in the blade. Since only the steady DLC1.1 cases are considered with variation from $V_{in}=3\text{m/s}$ to $V_{out}=16\text{m/s}$ with an increment of 1m/s, there are 14 design load cases and wind speeds. This results in a total of 59 constraints.

Case 2

This optimisation case allows for the spanwise laminate thickness distribution to be a design variable manipulated by the optimiser, in addition to the fibre layup angle distribution. The laminate thickness for both the pressure side and the suction side

TABLE 5.1: Design problem formulation: Case 1

	Variable/Function	Description	Quantity
minimise	$C(\{0, x_s, 0\}, p)$	Objective function	
with respect to	$-30^\circ \leq r01angle \leq +30^\circ$	Pressure side (Region 1) fibre layup angle	4
	$-30^\circ \leq r02angle \leq +30^\circ$	Suction side(Region 2) fibre layup angle	4
		Total design variables	8
subject to	$M_x BR \leq 1.02 * \max(M_x BR_{ref})$	max. $M_x BR$ constraint for each DLC	14
	$T \leq 1.02 * \max(T_{ref})$	Thrust constraint for each wind speed	14
	$M_x TB \leq 1.01 * \max(M_x TB_{ref})$	Tower bottom fore-aft moment constraint	14
	material failure index ≤ 1.0	Ultimate strain criteria constraint for each blade structural section	17
		Total constraints	59

skins of the blade section are subjected to upper and lower bounds of $\pm 0.005m$. Being a structural design variable, it is represented by a bezier-type FFD spline with control points specified at the normalised spanwise locations of $[0, 0.2, 0.55, 0.85, 1]$. In other words, at spanwise locations of 0%, 20%, 55%, 85% and 100% blade length. These control points are manipulated by the optimiser according to the specified bounds subject to constraints. The laminate thicknesses of the rest of the blade are determined by the bezier curve distribution through these points. To prevent negative thicknesses the laminate thickness variables are constrained between a lower bound of 0.0002m and an upper bound of 0.005m. As a result 10 more design variables are added to the count for Case 1, increasing their total number to 18.

The constraint bounds are scaled by 0.001m to obtain non-dimensional bounds. The reason for the scaling of the constraints is to ensure that the non-zero derivatives of the constraints and design variables are of the same order of magnitude. According to Wächter [49] for non-linear optimisation problems solved using IPOPT it is essential to determine good scaling factors such that extremely small and large non-zero entries in the gradients are avoided. The total number of constraints are increased to 69. The design problem formulation for Case 2 can be seen in Table 5.2.

5.3.4 Optimiser setting

The optimiser settings in IPOPT used for the MDO are provided in Table 5.3. By default IPOPT uses a residual tolerance of 10^{-8} as the convergence criteria. For the optimisation performed here the tolerance convergence criteria of the residuals is not used to determine a optimised solution. The residuals of the MDO never satisfy the specified criteria of 10^{-8} . Although, a different tolerance level can be set in the optimiser, no convergence studies have been performed in HAWTOpt2 to obtain a criteria to set such a value. The dependence of such a value on the turbine size and other parameters is unknown. Thus, for the optimisation cases performed in this

TABLE 5.2: Design problem formulation: Case 2

	Variable/Function	Description	Quantity
minimise	$C(\{0, x_s, 0\}, p)$	Objective function	
with respect to	$-30^\circ \leq r01angle \leq +30^\circ$	Pressure side (Region 1) fibre layup angle	4
	$-30^\circ \leq r02angle \leq +30^\circ$	Suction side (Region 2) fibre layup angle	4
	$-0.005[m] \leq r01thick \leq 0.005[m]$	Pressure side (Region 1) laminate thickness	5
	$-0.005[m] \leq r02thick \leq 0.005[m]$	Suction side (Region 2) laminate thickness	5
		Total design variables	18
subject to	$M_x BR \leq 1.02 * \max(M_x BR_{ref})$	max. $M_x BR$ constraint for each DLC	14
	$T \leq 1.02 * \max(T_{ref})$	Thrust constraint for each wind speed	14
	$M_x TB \leq 1.01 * \max(M_x TB_{ref})$	Tower bottom fore-aft moment constraint	14
	material failure index ≤ 1.0	Ultimate strain criteria constraint for each blade structural section	17
	$0.2 \leq r01thick \leq 5$ thickness scalar= 0.001 [m]	Pressure side (Region 1) laminate thickness constraint	5
	$0.2 \leq r02thick \leq 5$ thickness scalar= 0.001 [m]	Suction side (Region 2) laminate thickness constraint	5
		Total constraints	69

thesis the optimisation was allowed to be executed for a maximum of 100 iterations of the optimiser. The convergence of the solution was checked visually by plotting the value of the objective function against the number of evaluations. If the objective function does not change by significant amounts over a number of iterations, the solution is said to be converged.

TABLE 5.3: IPOPT settings

Parameter	Description	Quantity
linear_solver	Linear solver to be used for step calculation	ma27
mu_strategy	Update strategy for barrier parameter	adaptive
max_iter	Maximum number of iterations	100
force_fd	Force finite differencing	True
fd_size	Finite difference step size	10^{-4}

5.4 Results and Discussion

In this section the results of the optimisation problems formulated in section 5.3 are presented and discussed. As was mentioned in subsection 5.3.1, the weight f in the objective function defined in Equation 5.1 is maintained at zero for these cases. The objective function thus is entirely dependent on the minimising the flapwise blade root bending moment $M_x BR$ and can be redefined as shown in Equation 5.2.

$$C = - \left(\frac{M_x BR(\{0, 0, 0\}, p)}{M_x BR(\{0, x_s, 0\}, p)} \right) \quad (5.2)$$

where x_s are the structural design variables and p are the turbine parameters kept constant. The planform design variables x_p and operational design variables X_{oper} are not used in the optimisation cases and hence are set as zero. The value of the objective function C begins from a value of -1 as the base iteration is equal to the reference iteration of the uncoupled case. For a successful optimisation the value of the objective function should become more negative with every evaluation, until it plateaus out and refuses to minimise further. That is when the solution is considered to be converged, as the no improvements can be gained from further optimisation. Case 1, Case 1.1 and Case2 seek to minimise Equation 5.2 and the results of these attempts are presented.

5.4.1 Case 1

In this optimisation case the aim was to achieve an optimal spanwise distribution of the fibre layup angle with the blade being coupled from a location of 40% blade length and onward. The laminate thickness was uniformly maintained at the minimum limit of 1mm set by manufacturing constraints. The optimisation was carried out for the objective function shown in Equation 5.2 with respect to the design variables and constraints shown in Table 5.1. This optimisation case was executed for a total of 100 iterations of the optimiser.

The evolution of the value of the objective function with each evaluation is shown in Figure 5.4. It is seen that the objective function remains close to its starting value

of -1 throughout the optimisation. The function shows a variation that is in the order of magnitude of 10^{-3} , with no trend of divergence from the base value. Thus, the objective function was not minimised for this case.

A comparison between the fibre layup angle and laminate thickness distributions of the reference uncoupled rotor and the final version obtained from the optimisation attempt are shown in Figure 5.5. The laminate thicknesses are maintained at 1mm, equal to the reference case. The fibre layup angles on both pressure side and suction side of the blade sections are seen to have departed from their baseline state. The pressure side fibre layup angle is positive at the 40% blade length mark but quickly obtains negative values with increasing span. On the suction side however the angles are seen to be positive for most of the span and obtain negative values only near the blade tip. The magnitudes of the fibre layup angles are small and in the order for magnitude of 10^{-2} . For successful bend-twist coupling towards feather, the pressure side should have a positive distribution of the fibre layup angle and the suction side should have a negative distribution. The negative sign on the suction side is due to the change in direction of the outward surface normal of the blade section from the pressure side to the suction side. On the suction side the blade surface normal points in the opposite direction than when on the pressure side. Thus, in order for both the fibre angles on both sides of the blade cross-section to mirror each other they need to have opposite signs.

The unsuccessful bend-twist coupling in the optimisation attempt is also noticed from Figure 5.6c, showing the spanwise distribution of the flapwise bending-torsion coupling stiffness K_{46} . For bend-twist coupling towards feather the value of K_{46} should be negative. However, K_{46} is seen to obtain low positive values with its highest magnitude at the 40% span and decreasing towards the tip to its reference state. Positive values of K_{46} are indicators of BTC towards stall. But due to the small magnitude of the coupling, the effect of the observed fibre layup angle distribution is negligible. Yet another indicator of the lack of BTC is the flapwise bending stiffness distribution and torsional distribution, both of which are seen to have nearly the same value as the reference case. In a successfully bend-twist coupled blade, a decrease in the flapwise bending stiffness accompanied by a slight increase in the torsional stiffness is expected.

The comparison of the maximum flapwise blade tip deflection and maximum flapwise bending moments between the reference uncoupled case and the final version from the optimisation attempt is shown in Figure 5.7. The relative change in the maximum flapwise bending moment with respect to the baseline blade, seen in Figure 5.7c, does not show a clear trend especially in the partial load region below the rated wind speed of 10 m/s. Beyond the rated wind speed the rotor is controlled by pitch actuation thus BTC has a diminished role. The small increase seen in this region could be attributed to increased loads due to BTC towards stall noticed in the blade from the optimisation attempt. A corresponding increase in the flapwise blade tip deflection is also noticed in the partial load region. The differences seen can also be attributed to a contribution from the non-deterministic outcome of the HAWC2 simulations. The spanwise angle of attack is examined in Figure 5.8, at a wind speed of 7m/s which shows the greatest relative increase in the flapwise bending moment and tip deflection. It is seen that any change in angle of attack is almost non-existent. Thus, the increase observed in the flapwise loads and tip deflection in the partial load region cannot be accounted for by the small degree of BTC towards stall, as it seems to have no effect on the angle of attack.

The results presented for this optimisation case indicate a clear failure in minimising the objective function and in turn to minimise the flapwise blade root bending moment. The optimiser was not able to utilise bend-twist coupling towards feather to achieve this aim.

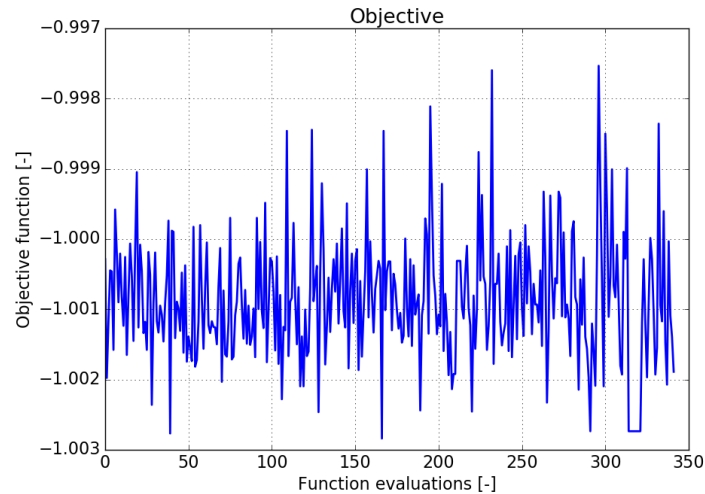
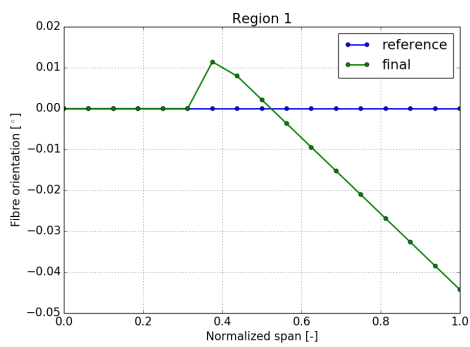


FIGURE 5.4: Case 1: Value of the objective function with each evaluation for a total of 100 optimiser iterations

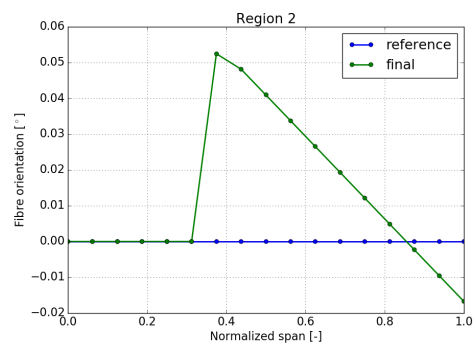
5.4.2 Case 2

In this optimisation case the aim was to achieve an optimal spanwise distribution of the fibre layup angle and the laminate thickness. Once again the blade was coupled from a location of 40% blade length and onward. However, the laminate thickness was allowed to be manipulated throughout the blade. The lower limit of the laminate thickness was set at 0.2mm, which is below the minimum set by the manufacturing constraint. The optimisation was carried out for the objective function shown in Equation 5.2 with respect to the design variables and constraints shown in Table 5.2. This optimisation case was executed for a total of 100 iterations of the optimiser.

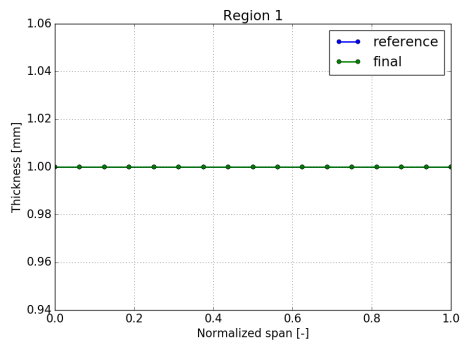
The development of the objective function with each evaluation is shown in Figure 5.9. It is seen that the value increases from its base value of -1 in the first few iterations and settles at a value around -0.85 . For the remainder of the iterations, the value is seen to be maintained around this point with slight variations, until near the end when it increase further. It is evident that the optimiser is unable to minimise the objective function. But, unlike Case 1, an increase in the objective function from its base value of -1 means that the maximum flapwise bending moment in the optimisation attempt was higher than the reference value for the uncoupled rotor. With a final value of the objective function at -0.8 , the flapwise bending moment after this optimisation attempt was 25% higher than the reference value. There is a constraint placed on the flapwise blade root bending moment not exceeding the reference value by 2%, as seen in Table 5.2. Thus, this constraint was violated during the optimisation. Hence, the optimisation problem defined by this case too has failed to achieve its objective.



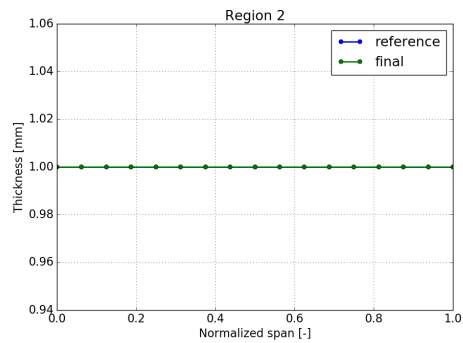
(A) Pressure side fibre layup angle



(B) Suction side fibre layup angle



(C) Pressure side laminate thickness



(D) Suction side laminate thickness

FIGURE 5.5: Case 1: Comparison of fibre layup angle and laminate thickness spanwise distribution between reference and final version

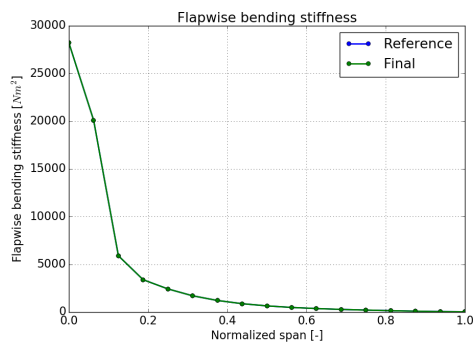
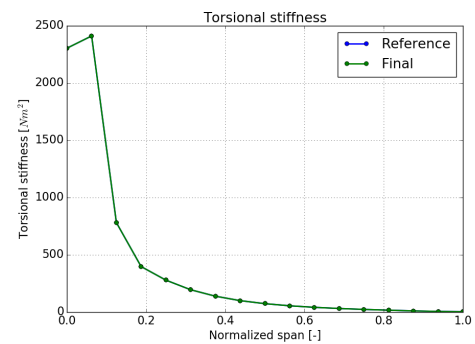
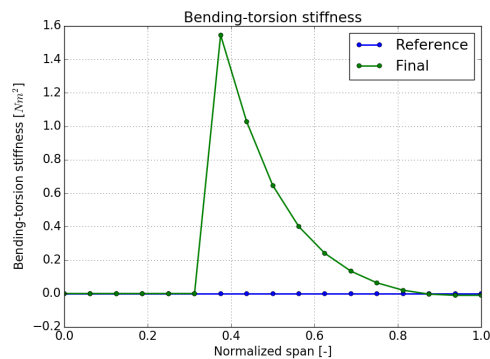
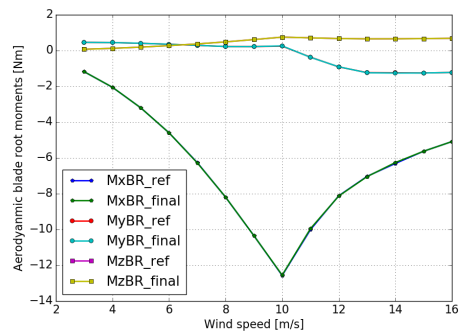
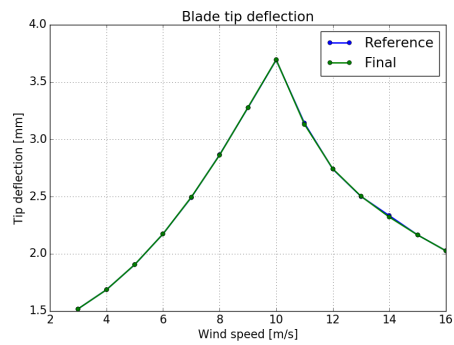
(A) Flapwise bending stiffness K_{44} (B) Torsional stiffness K_{66} (C) Flapwise bending-torsion coupling stiffness K_{46}

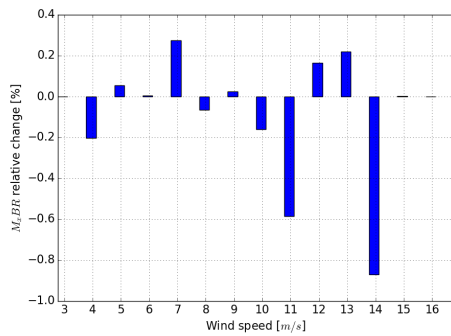
FIGURE 5.6: Case 1: Comparison of flapwise bending, bending-torsion and torsional stiffness spanwise distributions between reference and final version



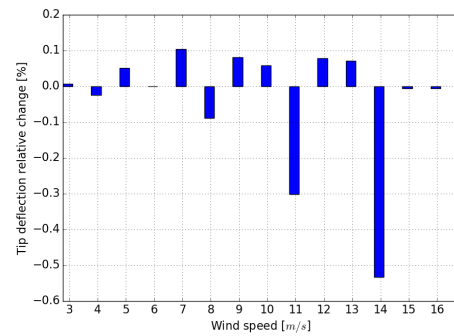
(A) Flapwise, torsional and edgewise moments



(B) Maximum flapwise blade tip deflection

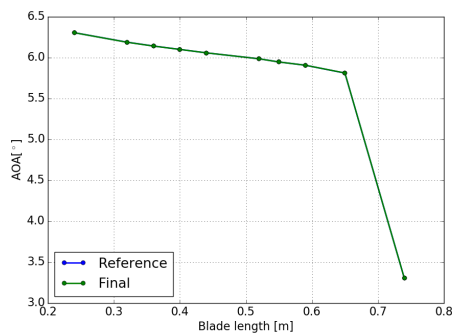


(C) Change in flapwise bending moment relative to reference

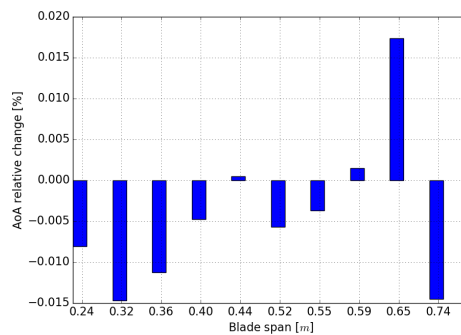


(D) Change in flapwise tip deflection relative to reference

FIGURE 5.7: Case 1: Comparison of aerodynamic moments and maximum flapwise tip deflection between reference and final version



(A) Angle of attack at 7m/s



(B) Angle of attack of final version relative to reference

FIGURE 5.8: Comparison of spanwise angle of attack distribution between final version and reference case at 7 m/s

The spanwise distribution of the fibre layup angle and laminate thickness for both the pressure and suction sides of the blade sections are shown in Figure 5.10. It is seen that the fibre layup angle once again attains a low value which is in the order of magnitude of 10^{-2} . The laminate thicknesses, seen in Figure 5.10c and Figure 5.10d, increase from their reference value of 1mm. Their new value varies from around 2.5 mm near the root to a maximum of 3mm at around 80% span. Beyond this point they decrease quickly to 1.2mm at the tip.

As explained in subsection 4.1.4, the cross-sectional stiffnesses of the blade sections scale proportionally with laminate thickness. The increase in the laminate thickness is translated into an increase in the flapwise bending and torsional stiffness, as seen in Figure 5.11a and Figure 5.11b. This is especially evident closer to the root as the chord too has higher values compared to the mid-section and the tip, leading to high magnitudes of stiffness. The flapwise bending-torsion stiffness K_{46} distribution is shown in Figure 5.11c. The positive values of K_{46} indicate BTC towards stall, stemming from the negative fibre layup angle in the pressure side of blade sections. However, the low magnitude of this value makes the strength of BTC negligible.

The maximum flapwise blade root bending moment and flapwise blade tip deflection for the span are shown in Figure 5.12. A reduction in the flapwise blade tip deflection and an increase in the flapwise blade root bending moment could be attributed to the increase in the flapwise bending stiffness as a result of increased laminate thickness. The blade is more stiffer than the reference case leading to a smaller flapwise deflection.

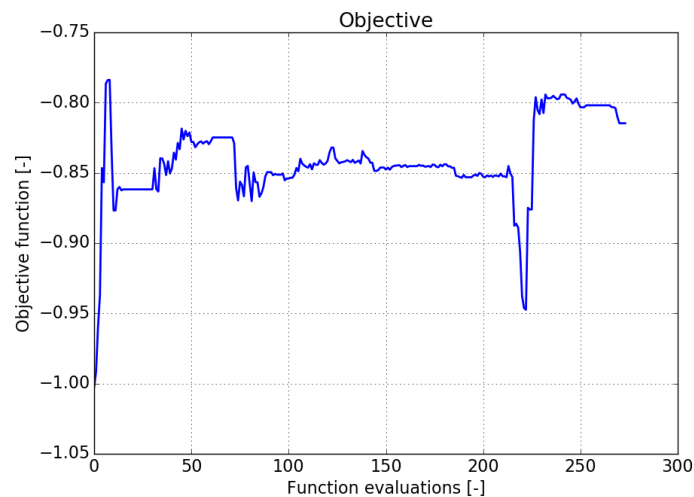
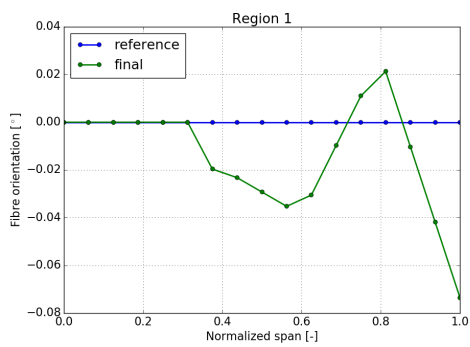


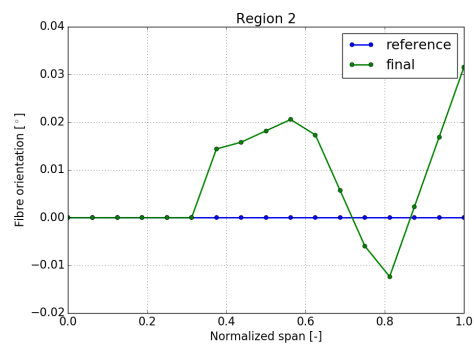
FIGURE 5.9: Case 2: Value of the objective function with each evaluation for a total of 100 optimiser iterations

5.5 Challenges in optimisation

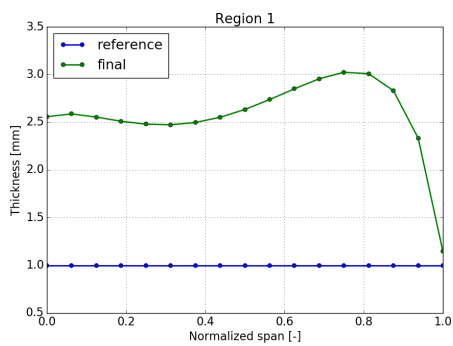
As discussed in section 5.1, the primary aim of utilising the multidisciplinary optimisation was to obtain a spanwise distribution of fibre layup angles and laminate thicknesses with the existing blade planform, that would give the best possible reduction in the loads unobtainable through parametric studies alone. However, the



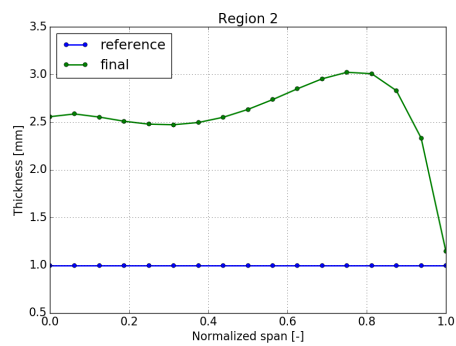
(A) Pressure side fibre layup angle



(B) Suction side fibre layup angle



(C) Pressure side laminate thickness



(D) Suction side laminate thickness

FIGURE 5.10: Case 2: Comparison of fibre layup angle and laminate thickness spanwise distribution between reference and final version

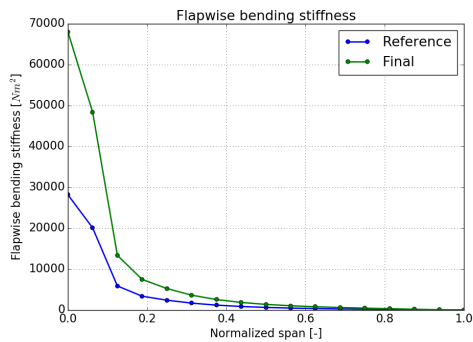
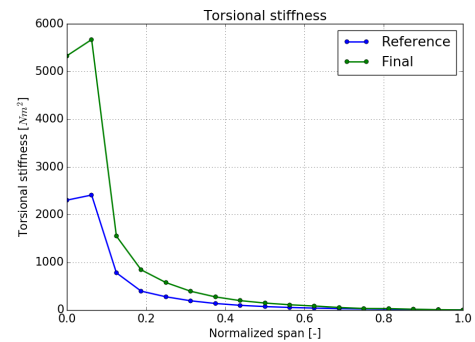
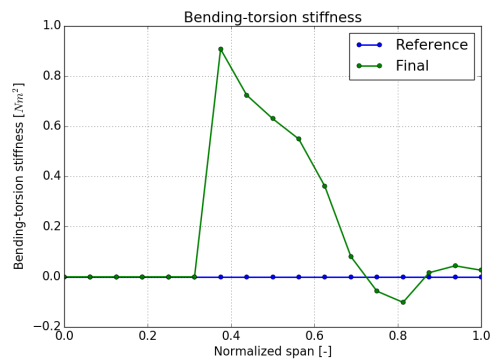
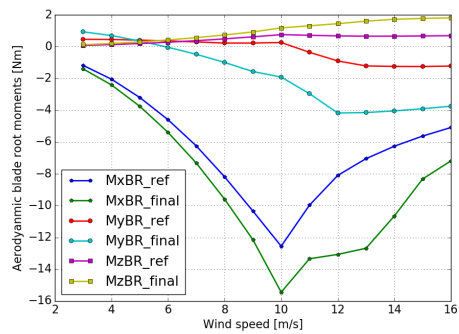
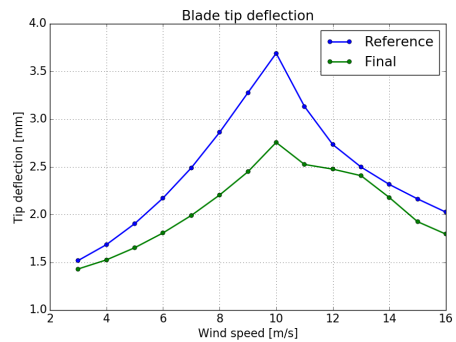
(A) Flapwise bending stiffness K_{44} (B) Torsional stiffness K_{66} (C) Flapwise bending-torsion coupling stiffness K_{46}

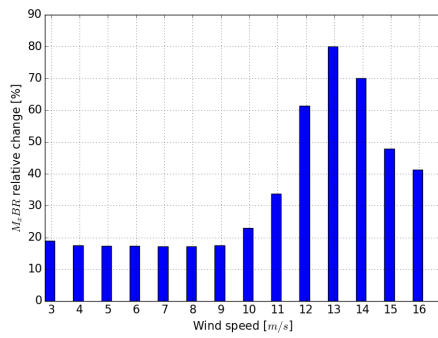
FIGURE 5.11: Case 2: Comparison of flapwise bending, bending-torsion and torsional stiffness spanwise distributions between reference and final version



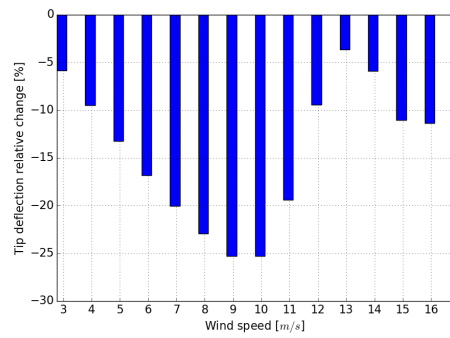
(A) Flapwise, torsional and edgewise moments



(B) Maximum flapwise blade tip deflection



(C) Change in flapwise bending moment relative to reference



(D) Change in flapwise tip deflection relative to reference

FIGURE 5.12: Case 2: Comparison of aerodynamic moments and maximum flapwise tip deflection between reference and final version

results presented in section 5.4 depict the failure of the optimisation problems that were setup to implement material bend-twist coupling successfully in a 0.75m long 500W small wind turbine blade.

5.5.1 Scaling, finite difference step and constraint violations

Case 1 is focused on obtaining the best possible spanwise fibre layup angle distribution for a fixed laminate thickness of 1mm. But the objective function isn't able to minimise much further than the baseline value of -1 . Since there are no constraint violations recorded in this case, the failure of the optimisation is attributed to either bad gradients or that the problem cannot be optimised further.

Since the external solvers used in this optimisation do not supply OpenMDAO with analytic gradients, it uses finite difference methods to compute gradients of the objective function and constraints. Along with correct scaling of the design variables and constraints, the right value of the finite difference step size is essential to obtain a fast, converging solution without sudden variations [52]. The objective function development shown in Figure 5.4, displays sudden changes in the value of the objective function with steep zig-zag behaviour. Though this variation is on the order of magnitude of 10^{-3} , such a behaviour and the lack of convergence of the optimisation thereof, could be attributed to bad scaling of the design variables and the chosen finite difference step size of 10^{-4} not being the correct one.

Alternatively, the failure of the optimisation in Case 1 could be attributed to a lack of a better solution than the reference case. However, from the parametric study performed in section 4.2 there clearly are more viable solutions providing different magnitudes of relative reduction in the flapwise blade root bending moment. The greatest reduction of -2.9% is obtained when the blade is being coupled at 25° fibre layup angle from 40% blade length and onward. Thus, the optimisation should at least attain this fibre layup angle distribution even if a better one does not exist. The failure to do so, points to a combination of two possible reasons. First, the best possible relative reduction in flapwise blade root bending moment could not be much higher than the one with constant fibre layup angle of 25° . Second, bad scaling of design variables and constraints along with an inappropriate choice of the finite difference steps results in poor, inaccurate gradients of the objective and constraints.

The inaccurate gradients most probably are unable to correctly capture the small gains in the flapwise bending moment reduction that can be made through the alteration of the fibre layup angle along the blade span. This may lead to an underprediction of the effectiveness of the positive fibre layup angles to reduce the flapwise bending moment to a greater value than is currently being achieved.

In Case 2, laminate thicknesses are also set as design variables along with the fibre layup angles. The value of the objective function, seen in Figure 5.9, to increase from its reference value of -1 to around -0.8 - -0.85 . This increase violates the flapwise blade root bending moment constraint. It is also seen that the objective function is not able to recover from this constraint violation, as for most of the iterations the value never minimises. Like in Case 1, this constraint violation could be attributed to poor gradients due to bad scaling and a wrong finite difference step size. However, in addition to the gradient with respect to the fibre layup angle the presence of laminate thickness as a design variable provides another poor gradient leading to the constraint violation.

5.5.2 Torsional stiffness and solidity

Irrespective of the fibre angle and laminate thickness spanwise distributions that could have been achieved by the optimisation with accurate gradients, it is evident from the parametric studies that the relative reduction in the steady state flapwise bending loads is low. A higher possible reduction would have allowed for a more robust response from the optimiser despite the inaccurate gradients. In fact, the low allowances in flapwise load reduction could have increased the sensitivity of the optimisation by being over-dependent on the quality of the constraint scaling and gradients. Zahle et al. [52] have shown that in their optimisation of the DTU 10MW turbine [4] using HAWTOpt2 to maximise the AEP, the quality of the gradients are fairly good for a range of finite difference step sizes varying from 7.5×10^{-3} to 10^{-1} , provided that the scaling of the design variables and constraints are properly done. The rates of convergence are however, affected by the finite difference step size. Thus their study displayed the robustness of the optimiser in performing the optimisation smoothly albeit at different rates.

The reason for the low relative reduction in the flapwise blade root bending moments in the 500W turbine is that the blades are not sufficiently soft in torsion. In other words, the torsional stiffness is too high for the aerodynamic loads being generated by the prevailing blade planform with a length of 0.75m. The high torsional stiffness which further increases from its uncoupled value with increasing fibre layup angle, provided low torsional deformation due to BTC. A low torsional deformation means that the angle of attack is not reduced sufficiently for BTC towards feather to bring about a sizeable reduction in load. As explained in subsection 4.1.4 the torsional stiffness scales proportionally to the laminate thickness and the cube to the chord of the blade cross-section. An effective means of making the blade more flexible in torsion would be to decrease the cross-sectional chord length and in turn produce a more slender blade. The downside of decreasing the chord length is that the other cross-sectional stiffnesses including the flapwise bending stiffness too scale to the cube of the chord. Hence for a slender blade, flapwise blade tip deflection would increase enhancing the risk of the blade hitting the tower under the action of extreme wind loads. However, maintaining a sufficient tower clearance would solve this issue. A rule of thumb for larger turbines is that the allowance for the blade tip deflection under extreme conditions should be 0.2 times the rotor radius. In the case of the 500W turbine that would result in an extreme flapwise blade tip deflection of 0.55m. Currently, for the highest flapwise moment reduction achieved at a constant fibre layup angle distribution of 25° , the maximum flapwise tip deflection under steady conditions is 11mm, which is 85% higher than the uncoupled blade. Thus, there is sufficient space to accommodate larger flapwise blade tip deflections as a result of a slender blade profile.

In order to enforce the argument advocating the need of a slender blade profile to enhance material BTC in the 500W wind turbine blade, a comparison of the solidity is provided with the DTU 10MW turbine blade. The DTU 10MW turbine has a slender blade profile but is still more conservative when compared to the modern HAWTs in the wind industry. Additionally, an AEP optimisation carried out on the DTU 10 MW using HAWTOpt2 resulted in the final design obtaining a shear-twist coupling. The twisting under applied loads caused a 6% decrease in the flapwise damage equivalent load (DEL) [52]. Finally, the data for the DTU 10MW blade is readily available. Thus, a relatively conservative slender blade profile proven to be

receptive towards material torsion coupling, and the ease of availability of its blade data makes the DTU 10MW a good subject for comparison.

Rotor solidity(σ) is defined as the total blade area by the swept area. The solidity as a function of the normalised blade span is given by Equation 5.3.

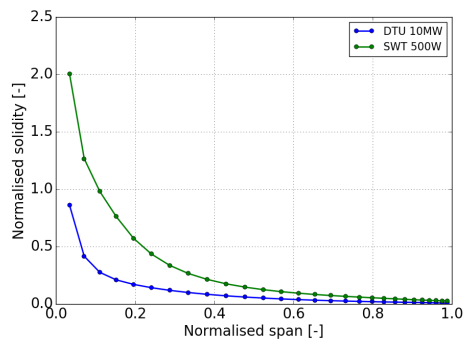
$$\sigma(r') = \frac{\left(\frac{c(r')}{R}\right) B}{2\pi r'} \quad (5.3)$$

where R is the blade radius, r' is the position of a blade section measured from the rotor centre normalised by the blade radius, B is the number of blades in the turbine and $c(r')$ is the chord distribution as a function of the normalised blade span. The solidity is a measure of energy capture from the available wind resource for the given rotor swept area. Thus, for the same swept area, a higher solidity would result in higher torque and allow the rotor to operate with its maximum efficiency at lower tip-speed ratios. This feature makes a high solidity rotor endearing for small wind turbines which typically operate in low wind speed conditions. The higher torque due to higher solidity would allow start-up at lower speeds. Consequently, operating at low tip speed ratio would mean that the magnitude of the rotor speed Ω range could be decreased. In this regard, a high blade solidity is beneficial to small wind turbines. However, in order to improve torsional flexibility of the blade and to extract the most benefit from BTC a slender blade is favourable.

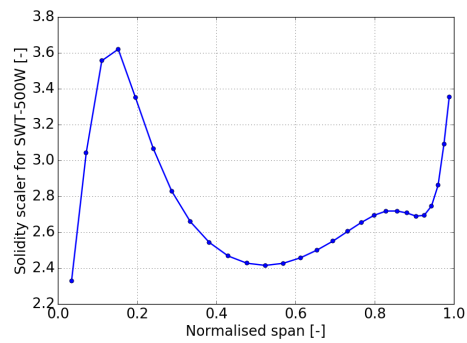
The rotor solidity as a function of the normalised blade spans are compared between the 500W and DTU 10MW blades in Figure 5.13a. The current 500W blade clearly has a solidity that is greater by a factor ranging from 2.4 to 3.6 over the normalised span, with respect to the DTU 10MW blade. The ratio of the solidity of the 500W blade to that of the DTU 10 MW over the normalised span is shown in Figure 5.13b. Since both HAWTs are three bladed, the main difference in their solidity stems from the broader profile employed by the 500W blade. The chord over the blade span normalised by their respective radii is seen in Figure 5.13c. The normalised chord of the 500W blade is seen to be much higher than that of the DTU 10MW. However, on dividing it by the solidity ratio a normalised chord distribution equal to that of the DTU 10 MW can be obtained. The resulting profile of the scaled 500W turbine (shown by the red dotted lines in Figure 5.13c) is more slender than the original design. It is expected that for the scaled 500W blade, the slender profile would provide a much higher torsional flexibility. Due to the dependence of the cross-sectional stiffnesses on the cube of the chord, a solidity ratio range of 2.4 to 3.6 over the span would provide cross-sectional stiffness scaling by factors ranging from 13.8 to 46.7.

The gains made in blade flexibility and BTC with a slender profile for the current 500W blade however needs a re-balancing in the operational parameters of the wind turbine. The altered blade planform with lower solidity would potentially lower the maximum power coefficient achieved through the design. The tip speed ratio would also need to be appropriately re-selected leading to a change in the rotor speed range. If the current rated power of 500W is to be more-or-less maintained then a higher tip-speed ratio and a higher rotor speed values would be required.

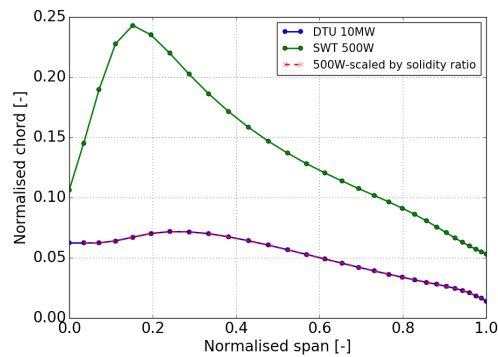
Alternatively, the tip-speed ratio and rotor speed values can be kept unchanged inviting a decrease in the rated power due to the decreased power coefficient. However, the rated power of 500W can be achieved by increasing the blade length and hence capturing energy from a larger rotor swept area.



(A) Solidity and blade span normalised by the radii for DTU 10MW and SWT 500W



(B) Ratio of the normalised solidity of SWT 500W to the DTU 10MW



(C) Chord and blade span normalised by the radii for DTU 10MW, SWT 500W, and SWT 500W scaled by the solidity ratio

FIGURE 5.13: Comparison of solidity and chord of 500W, DTU 10MW and a scaled version of 500W blades normalised by their respective radii

5.6 Recommendations

Based on the analysis presented in section 5.5 on the challenges encountered in the multidisciplinary optimisation the following recommendations are provided:

- It is recommended that a sensitivity study on finite difference gradient quality be performed. This is done by finding the gradients of the flapwise blade root bending moment $M_x BR$ with respect to the fibre layup angle $r01angle$ at the design variable points (spline control points) along the blade span for various finite difference step sizes. It would involve executing the complete aero-structural workflow with the stiffness computations in BECAS followed by aeroelastic simulations in HAWC2. Additionally, appropriate re-scaling of the constraints and design variables should be carried out such that their non-zero derivatives are neither too large or too small. These parametric studies in relation to the optimisation would allow for a rapid, smooth converging solution.
- The solidity of the current 500W blade should be decreased by employing a slender blade profile. The resulting blade would have a greater flexibility than the current one, enhancing the effect of flapwise BTC. The larger gains would also aid in improving the robustness of the optimisation problem despite the presence of poorly scaled constraints and inaccurate gradients.
- A slender profile would translate into a lower optimal aerodynamic power coefficient for the same tip-speed ratio as the original SWT 500W. A re-adjustment of the rated power, tip-speed ratio, rotor speed range and magnitude would have to be appropriately carried out. Alternatively, the blade length could be increased to maintain the rated power albeit with a slender profile conducive to BTC.
- Provided appropriate parameter scaling and accurate gradients are obtained through sensitivity studies, a MDO could be carried out using HAWTOpt2. In addition to the fibre layup angle and laminate thickness distributions, the spanwise chord distribution, rotor speed values and tip-speed ratio could be set as design variables with a constraint on the flapwise blade root bending moment and maximum allowable flapwise tip deflection. The objective function could be set by accordingly weighing AEP reduction and flapwise blade root bending moment reduction.

5.7 Summary

This chapter detailed the process involved in executing multidisciplinary optimisation of the 500W turbine blade to ensure the most beneficial outcome from implementing material bend-twist coupling towards feather on a fixed planform. The HAWTOpt2 aero-structural design tool using OpenMDAO as its core was utilised to implement the optimisation. Essentially, the optimisation was structural in nature with the blade planform and turbine operational parameters remaining constant. The spanwise fibre layup angle and laminate thickness distribution were the only structural design variables that were allowed to be manipulated by the optimiser. The objective function comprised of two different individual objective functions weighed according to the situation. The two parts involved minimising the

flapwise blade root bending moment M_xBR and maximising the AEP. The existing literature conveyed a marginal decrease in the AEP for the presence of flapwise bend-twist coupling. As a result it was decided to perform initial optimisation with no contribution from the part of the objective function that maximises AEP. In other words, the weight was completely given to the minimisation of M_xBR . Two optimisation design problems, Case 1 and Case 2, were setup. Case 1 maintained a uniform laminate thickness at the minimum value of 1mm set by manufacturing limits, but the fibre layup angle was kept as a design variable. Case 2 allowed both laminate thickness and fibre layup angle distribution as design variables. Both optimisation cases failed with Case 1 not minimising the objective function further than the base value of -1 , whereas Case 2 showed an increase in the value of the objective function resulting in a constraint violation.

The reasons for the failure in the MDO were attributed primarily to poor scaling of the constraint and design variables, and a wrong choice of the finite difference step size. Poor scaling of the constraints and design variables creates first order non-zero gradients that are either extremely large or extremely small, impeding the optimisation. A wrong choice of the finite difference step size along with the presence of poorly scaled design variables gives rise to inaccurate gradients of the objective function and constraints. These in turn lead to sudden variations in the objective function and decreases the robustness of the solver.

The maximum relative reduction in M_xBR obtained through BTC for a constant fibre layup angle of 25° was -2.9% . This decrease was deemed insufficient to be successfully captured by the poor gradients of the optimiser. The primary reason for the low reduction was a low torsional deformation due to the high torsional stiffness of the blade for the aerodynamic loads applied on the 0.79m long blade. A slender blade profile produced by lowering the chord length would greatly enhance the torsional deformation by making the blade more flexible. However, this would in turn also affect the performance of the turbine.

Finally, based on a discussion of the challenges encountered in the optimisation the following was recommended:

- A sensitivity study on the gradient quality due to the choices of the finite difference step size and parameter scaling with regard to the chosen structural design variables and constraints should be performed.
- The solidity of the current 500W blade should be decreased by employing a slender blade profile resulting in a blade with higher flexibility.
- As a consequence of the slender blade profile, a re-evaluation of the operational parameters of the turbine including the rotor speed range, the tip-speed ratio, the rated wind speed and the rated power is required.
- A MDO design case could be performed in order to obtain a beneficial implementation of BTC for the slender blade profile by balancing the minimisation of AEP and M_xBR through weights.

Chapter 6

Conclusion

The purpose of this thesis was to establish the effectiveness of including material bend-twist coupling (BTC) in a small wind turbine blade by incorporating it in the rotor design process through a multidisciplinary constrained optimisation approach. The performance metrics measuring the effectiveness of BTC such as flapwise blade root bending moment, torsional deflection and AEP for the optimised design were then to be compared against the uncoupled reference turbine.

The first task was to design the reference blade by following the constraints imposed by the regulations of the Small Wind Turbine Competition. With respect to the rotor design, the competition placed limitations on the maximum rotor swept area and the site wind climate. The rotor swept area was fixed to a maximum of $2m^2$ constraining the maximum possible blade length to 0.75m. The site wind climate had an average wind speed of 4m/s. Thus, the turbine had to be designed to maximise the power for low wind speeds, in order to obtain a winnable AEP with regard to the competition. The aerodynamic design, including the definition of the blade planform, operational parameters and airfoil choice was created in the previous iteration of the competition. The key design philosophy that went in selecting the operational parameters and the airfoil choice has been explained. A tip-speed ratio of 5 and a rated power of 500W was selected. A low tip speed ratio allows for lower start-up rotor speed. Existing studies on the dependence of power coefficient variation on the lift to drag ratio of airfoils over different tip-speed ratios showed that for a tip-speed ratio of 5, an optimal power coefficient of 0.45 is obtained for a lift to drag ratio of 50. Accordingly, SD7032 airfoil with a relative thickness of 10% was selected due to its stable performance across the range of Reynolds numbers experienced by the wind turbine. The blade planform was borrowed from the previous iteration of the SWT 500W turbine, but was verified using a BEM code and measurements from the actual blade. The low wind climate prompted the selection of a low cut-in wind speed of 3m/s, a rated wind speed of 10m/s and a cut-out wind speed of 16m/s. A rotor performance analysis was carried out on the aerodynamic design with the appropriately chosen design parameters. The performance was in accordance with the aerodynamic design goals for the mid-span and out-board regions. However, there were losses in the performance in the in-board region due to increasing relative thicknesses of the profile and a manufacturing limitation on the maximum twist angle. This caused the in-board sections to operate in their respective stall regions.

Next, the internal structure of the blade was chosen and the composite materials were shortlisted. Carbon-epoxy FRP of type Tenax UTS50 F13 12K and glass-epoxy FRP of type E-glass were selected as the potential materials for the blade. The laminate properties for both glass-epoxy and carbon-epoxy FRP was computed from

the fibre and resin properties using micro-mechanics equations for composites. Accounting for the restrictions on the magnitude of the aerodynamic forces and moments placed by the small blade length, the blade was made as flexible as possible in order to make it soft in torsion and thus aid BTC. With a focus on increasing the flexibility of the blade, the spar was excluded from the design, the laminate thickness of the skin was maintained at the minimum manufacturing limit of 1mm, a sandwich material was not included and lastly only one layer of unidirectional composite laminate was used throughout the blade. The spanwise distribution of the cross-sectional stiffnesses were compared for the two reference blades made of carbon fibre and glass fibre. The carbon fibre blade was seen to have higher flapwise bending, edgewise bending and torsional stiffnesses along the span. A decrease in the stiffnesses with increasing span was attributed to the reduction in cross-sectional dimensions. The trend was seen to mimic the spanwise chord distribution trend. After finalising the aerodynamic design, the turbine operational parameters and the internal blade structure, the reference blade thus produced was utilised to tune the DTU Wind Energy controller. The tuning of the controller is required to perform time-domain aero-servo-elastic simulations in HAWC2.

Upon finalising the reference blade and tuning the controller, two parametric studies were carried out. First, a stiffness study was conducted wherein the cross-sectional stiffnesses for both glass and fibre blades were analysed for a range of negative and positive fibre layup angles. The material BTC was introduced through manipulation of the fibre layup angle in the cross-section, such that the pressure side and suction side angles "mirrored" each other. The main aim of this study was to identify the contributions of the torsion coupling stiffness terms towards BTC, the fibre angle range that would result in twisting towards feather, the material most conducive to BTC amongst carbon and glass composites, and the dependence of the stiffnesses on cross-sectional dimensions. Asymmetric cross-sections resulted in couplings between shear forces, axial tension, edgewise moment and torsion, in addition to the flapwise BTC. Secondary couplings individually influenced the induced torsion to a lesser extent than the flapwise BTC. However, irrespective of the magnitude their combined contributions ultimately did influence the torsional deflection. Flapwise BTC towards feather was achieved for all positive fibre layup angles. A low ratio of flapwise bending stiffness to flapwise bending-torsion coupling stiffness K_{44}/K_{46} and a high ratio of flapwise bending-torsion coupling stiffness to torsional stiffness K_{46}/K_{66} resulted in the highest magnitude of torsional deflection in the study, provided the moments and deflection remain the same. In generalised terms, low flapwise bending stiffness and torsional stiffness along with a high coupling stiffness resulted in a stronger BTC. Carbon outperformed glass for all fibre angles with regard to the amount of coupling seen in the cross-sections. Due to the high values of stiffnesses and lower mass density, the effect of secondary couplings were considered to be less pronounced in carbon compared to glass. However, as the net effect of the contributions from the secondary couplings could not be judged based on the stiffnesses alone, the response of BTC under wind loads had to be considered to choose the final material. For the same cross-sectional profile and material the flapwise bending stiffness, torsional stiffness and the bending-torsion coupling stiffness were found to scale with tc^3 . Where t is the laminate thickness and c is the chord of the section.

Second, a load response study was carried out for varying positive fibre layup angles in both carbon-fibre and glass-fibre blades, under steady wind conditions for the operational wind speed range. An increase in the flapwise blade tip displacement and a reduction in the flapwise bending loads with increasing fibre-layup angles was noted for both glass-fibre and carbon-fibre blades. It was also observed that absolute change in the flapwise loads over the different fibre angles was negligible. This trend was also seen in the AEP which also showcased negligible difference over variations in the fibre layup angles. The reason was that both parameters are affected by the same underlying phenomenon of a small decrease in the angle of attack. The reduction in the angle of attack was not large enough to push the aerodynamic performance of the airfoil below its optimal design range. Thus, although there was a decrease in the aerodynamic forces it was too small to have a profound effect on flapwise load reduction.

Decreasing the flapwise bending and torsional stiffness of the blade would have made it more responsive to the aerodynamic loads and possibly resulted in larger induced torsional deformations and higher load reductions. The stiffness scales linearly with the skin laminate thickness and a reduction would have also resulted in lighter and consequently cheaper design. However, being set at the minimum manufacturing limit of 1mm throughout the blade the thickness cannot be decreased further. Another method could be to increase the fibre-layup angle further so as to decrease the flapwise bending stiffness. This would however also be accompanied by a decrease in the bend-twist coupling factor.

The case for implementing BTC using MDO is made by arguing that the optimiser can negotiate the relationships between the various parameters in a more precise manner than can be done using sensitivity studies alone. Thus, it was expected that through MDO a higher reduction in the flapwise bending loads could be achieved compared to the uncoupled case, than indicated by the load response study. The HAWTOpt2 aero-structural design tool using OpenMDAO as its core was utilised to implement the optimisation. The optimisation was structural in nature with the blade planform and turbine operational parameters remaining constant. The spanwise fibre layup angle and laminate thickness distribution were the only structural design variables that were allowed to be manipulated by the optimiser. The objective function comprised of two different individual objective functions weighed according to the situation. The two parts involved minimising the flapwise blade root bending moment $M_x BR$ and maximising the AEP. The existing literature conveyed a marginal decrease in the AEP for the presence of flapwise bend-twist coupling. As a result it was decided to perform initial optimisation with no contribution from the part of the objective function that maximises AEP. In other words, the weight was completely given to the minimisation of $M_x BR$. Two optimisation design problems, Case 1 and Case 2, were setup. Case 1 maintained a uniform laminate thickness at the minimum value of 1mm set by manufacturing limits, but the fibre layup angle was kept as a design variable. Case 2 allowed both laminate thickness and fibre layup angle distribution as design variables. Both optimisation cases failed with Case 1 not minimising the objective function further than the base value of -1 , whereas Case 2 showed an increase in the value of the objective function resulting in a constraint violation.

The reasons for the failure in the MDO were attributed primarily to poor scaling of the constraint and design variables, and a wrong choice of the finite difference step

size. Poor scaling of the constraints and design variables creates first order non-zero gradients that are either extremely large or extremely small, impeding the optimisation. A wrong choice of the finite difference step size along with the presence of poorly scaled design variables gives rise to inaccurate gradients of the objective function and constraints. These in turn lead to sudden variations in the objective function and decreases the robustness of the solver.

The maximum relative reduction in M_xBR obtained through BTC for a constant fibre layup angle of 25° was -2.9%. This decrease was deemed insufficient to be successfully captured by the poor gradients of the optimiser. The primary reason for the low reduction was a low torsional deformation due to the high torsional stiffness of the blade for the aerodynamic loads applied on the 0.79m long blade. A slender blade profile produced by lowering the chord length would greatly enhance the torsional deformation by making the blade more flexible. However, this would in turn also affect the performance of the turbine.

Finally, based on a discussion of the challenges encountered in the optimisation the following was recommended:

- A sensitivity study on the gradient quality due to the choices of the finite difference step size and parameter scaling with regard to the chosen structural design variables and constraints should be performed.
- The solidity of the current 500W blade should be decreased by employing a slender blade profile resulting in a blade with higher flexibility.
- As a consequence of the slender blade profile, a re-evaluation of the operational parameters of the turbine including the rotor speed range, the tip-speed ratio, the rated wind speed and the rated power is required.
- A MDO design case could be performed in order to obtain a beneficial implementation of BTC for the slender blade profile by balancing the minimisation of AEP and M_xBR through weights.

The hypothesis that was formulated in the introduction of the report stated "Material bend-twist coupling is an effective means to substantially decrease the aerodynamic loads in a small wind turbine blade with only a marginal decrease in AEP". Small wind turbines are usually designed with high solidity. The resulting aerodynamic loads may not be high enough, and the blade not flexible enough to make BTC effective. Due to the low gains achieved by implementing BTC through parametric studies, it was hoped that MDO could bring about the greatest possible load reduction through BTC due to the mathematical handling of the problem by balancing different dependencies. The failure of the MDO cases makes it difficult to establish whether bend-twist coupling can truly be effective on a small wind turbine.

However, the parametric studies did show that bend-twist coupling is certainly beneficial in bringing about load reduction. It can be argued that the effectiveness of BTC cannot be successfully judged through its implementation on a fixed planform blade for the 500W turbine. To make BTC more beneficial a concurrent design approach is required wherein the aerodynamic design is altered in tandem with the structural design. In conclusion, the stated hypothesis couldn't be completely defended with the studies in this thesis.

It was originally intended that the blade designed through MDO would be manufactured to be used in the Small Wind Turbine Competition. It was also the intention to carry out experimental measurements in the wind tunnel and through a static load test. There were several delays of a severe nature during the course of this thesis, especially with the implementation of bend-twist coupling in the HAWTOpt2 workflow. As HAWTOpt2 is currently under development, there were bugs encountered in the underlying code that were not conducive towards the implementation of BTC. These bugs were fixed, but by then a substantial time had been lost, cutting short the scope of this thesis.

Bibliography

- [1] Thomas D Ashwill. "Passive load control for large wind turbines". In: *AIAA, April* (2010).
- [2] Christian Bak. "Aerodynamic design of wind turbine rotors". In: *Advances in wind turbine blade design and materials*. Ed. by Povl Brøndsted and Rogier Nijssen. Woodhead Publishing, 2013. ISBN: 978 0 85709 426 1.
- [3] Christian Bak. "Sensitivity of key parameters in aerodynamic wind turbine rotor design on power and energy performance". In: *Journal of Physics: Conference Series*. Vol. 75. 1. IOP Publishing. 2007, p. 012008.
- [4] Christian Bak et al. "Description of the DTU 10 MW reference wind turbine". In: *DTU Wind Energy Report-I-0092* 5 (2013).
- [5] José Pedro Blasques. "Multi-material topology optimization of laminated composite beams with eigenfrequency constraints". In: *Composite Structures* 111 (2014), pp. 45–55.
- [6] Jose Pedro Blasques and Mathias Stolpe. "Multi-material topology optimization of laminated composite beam cross sections". In: *Composite Structures* 94.11 (2012), pp. 3278–3289.
- [7] JP Blasques and RD Bitsche. "An efficient and accurate method for computation of energy release rates in beam structures with longitudinal cracks". In: *Engineering Fracture Mechanics* 133 (2015), pp. 56–69.
- [8] JP Blasques et al. "Accuracy of an efficient framework for structural analysis of wind turbine blades". In: *Wind Energy* (2015).
- [9] Carlo L Bottasso, Filippo Campagnolo, and Alessandro Croce. "Multi-disciplinary constrained optimization of wind turbines". In: *Multibody System Dynamics* 27.1 (2012), pp. 21–53.
- [10] CL Bottasso et al. "Optimization-based study of bend–twist coupled rotor blades for passive and integrated passive/active load alleviation". In: *Wind Energy* 16.8 (2013), pp. 1149–1166.
- [11] Mark Capellaro. "Design Limits of Bend Twist Coupled Wind Turbine Blades". In: *53rd AIAA/ASME/ASCE/AHS/ASC Structures, Structural Dynamics and Materials Conference 20th AIAA/ASME/AHS Adaptive Structures Conference 14th AIAA*. 2012, p. 1501.
- [12] Christos C Chamis. "Simplified composite micromechanics equations for hygral, thermal and mechanical properties". In: *Sampe Quarterly* 15 (1984), pp. 14–23.
- [13] MC Cheney and PAM Spierings. "Self-regulating composite bearingless wind turbine". In: *Solar Energy* 20.3 (1978), pp. 233–240.
- [14] Python Community. *Python Wiki*. Available at <https://wiki.python.org/moin/IntegratingPythonWithOtherLanguages> note = Accessed: 2017-07-26.

- [15] DC Corbet and CA Morgan. "Report on the passive control of horizontal axis wind turbines". In: *ETSU WN 6043* (1992).
- [16] Nicolas Fichaux et al. "UpWind: Design limits and solutions for very large wind turbines". In: *Sixth Framework Programme* (2011).
- [17] Carlo Tibaldi Frederik Zahle. *Rotor Design Optimization Tools and Cost Models*. Technical University of Denmark. IQPC Workshop for Advances in Rotor Blades for Wind Turbines, Bremen, 2015.
- [18] Justin S. Gray, Kenneth T. Moore, and Bret A. Naylor. "OpenMDAO: An Open-Source Framework for Multidisciplinary Analysis and Optimization". In: *13th AIAA/ISSMO Multidisciplinary Analysis and Optimization Conference, Fort Worth, TX, AIAA, AIAA-2010-9101*. AIAA. Fort Worth, Texas, 2010. URL: <http://www.aric.or.kr/treatise/journal/content.asp?idx=134451>.
- [19] Morten Hartvig Hansen, Mac Gaunaa, and Helge Aagaard Madsen. *A Beddoes-Leishman type dynamic stall model in state-space and indicial formulations*. Tech. rep. Risø-R-1354(EN). Technical University of Denmark, 2004.
- [20] Morten Hartvig Hansen and Lars Christian Henriksen. "Basic DTU wind energy controller". In: *DTU Wind Energy Report-E-0018, DTU Wind Energy* (2013).
- [21] LC Henriksen and KA Kragh. "The linear Aero-Servo-Elastic code HAWC-Stab2: User Manual". In: *Report no. E-0022, DTU Wind Energy* (2013).
- [22] *INTERNATIONAL SMALL WINDTURBINE CONTEST 2017*. Available at <http://www.iswtc.com/note={Accessed:2017-04-17}>.
- [23] IRENA. *Wind Power Technology Brief*. Available at http://www.irena.org/DocumentDownloads/Publications/IRENA-ETSAP_Tech_Brief_Wind_Power_E07.pdf (2016-03-07) note = Accessed: 2017-04-17.
- [24] NM Karaolis, PJ Mussgrove, and G Jeronimidis. "Active and passive aeroelastic power control using asymmetric fibre reinforced laminates for wind turbine blades". In: *Proceedings of the 10th British Wind Energy Conference, London*. 1988, pp. 446–458.
- [25] Taeseong Kim. *Lecture notes for 46310: Projects in Wind Turbine Aeroelasticity*. Technical University of Denmark, 2017.
- [26] HJT Kooijman. *Bending-torsion coupling of a wind turbine rotor blade*. Netherlands Energy Research Foundation ECN Petten, Netherlands, 1996.
- [27] Andrew B Lambe and Joaquim RRA Martins. "Extensions to the design structure matrix for the description of multidisciplinary design, analysis, and optimization processes". In: *Structural and Multidisciplinary Optimization* 46.2 (2012), pp. 273–284.
- [28] Hans Hvidtfeldt Larsen and Leif Sønderberg Petersen. *DTU International Energy Report 2014: Wind energy—drivers and barriers for higher shares of wind in the global power generation mix*. 2014.
- [29] Torben J Larsen and Anders Melchior Hansen. *How 2 HAWC2, the user's manual*. Tech. rep. Risø National Laboratory, 2007.
- [30] Bernitt Mads Linander. "Aero-elastic design and analysis of a small HAWT with active/passive pitch control". MA thesis. Denmark: Technical University of Denmark, 2015.
- [31] Don Lobitz and David Laino. "Load mitigation with twist-coupled HAWT blades". In: *37th Aerospace Sciences Meeting and Exhibit*. 1999, p. 33.

- [32] Don Lobitz and Paul Veers. "Aeroelastic behavior of twist-coupled HAWT blades". In: *1998 ASME Wind Energy Symposium*. 1998, p. 29.
- [33] Don Lobitz, Paul Veers, and David Laino. "Performance of twist-coupled blades on variable speed rotors". In: *2000 ASME Wind Energy Symposium*. 2000, p. 62.
- [34] Don W Lobitz and Paul S Veers. "Load Mitigation with Bending/Twist-coupled Blades on Rotors using Modern Control Strategies". In: *Wind Energy* 6.2 (2003), pp. 105–117.
- [35] DW Lobitz, PS Veers, and PG Migliore. *Enhanced performance of HAWTs using adaptive blades*. Tech. rep. Sandia National Laboratory, 1996.
- [36] Leon Mishnaevsky Jr. "Composite materials in wind energy technology". In: *Thermal to Mechanical Energy Conversion: Engines and Requirements*, EOLSS Publishers: Oxford, UK (2011).
- [37] NASA. *Open-MDAO*. Available at <http://openmdao.org/> note = Accessed: 2017-07-25.
- [38] NASA. *OpenMDAO Documentation*. Available at <http://openmdao.readthedocs.io/en/1.7.3/index.html> note = Accessed: 2017-07-27.
- [39] S Andrew Ning, Rick Damiani, and Patrick J Moriarty. "Objectives and constraints for wind turbine optimization". In: *Journal of Solar Energy Engineering* 136.4 (2014), p. 041010.
- [40] DTU Risø NREL. *FUSED-Wind*. Available at <http://www.fusedwind.org/> note = Accessed: 2017-04-17.
- [41] FORTRAN community Ondřej Čertík. *Fortran Documentation*. Available at <http://www.fortran90.org/> note = Accessed: 2017-07-26.
- [42] Cheng Ong, Julie Wang, and Stephen Tsai. "Design, manufacture and testing of a bend-twist D-spar". In: *37th Aerospace Sciences Meeting and Exhibit*. 1999, p. 25.
- [43] Ruben E. Perez, Peter W. Jansen, and Joaquim R. R. A. Martins. "pyOpt: A Python-Based Object-Oriented Framework for Nonlinear Constrained Optimization". In: *Structures and Multidisciplinary Optimization* 45.1 (2012), pp. 101–118. DOI: 10.1007/s00158-011-0666-3.
- [44] Peter J Schubel and Richard J Crossley. "Wind turbine blade design". In: *Energies* 5.9 (2012), pp. 3425–3449.
- [45] MS Selig et al. *Summary of Low-Speed Airfoil Data, Vol. 2, University of Illinois at Urbana-Champaign*. 1997.
- [46] IEC TC88-MT. "Iec 61400-2: Wind turbines—part 2: Design requirements for small wind turbines". In: *International Electrotechnical Commission, Geneva* (2005).
- [47] Poryzala Tomek. "Wind Turbine Mechanical Passive Pitch Control". MA thesis. Denmark: Technical University of Denmark, 2016.
- [48] Paul Veers, Gunjit Bir, and Donald Lobitz. "Aeroelastic tailoring in wind-turbine blade applications". In: *Proceedings, Windpower*. Vol. 98. 1998, pp. 291–304.
- [49] Andreas Wächter. "Short Tutorial: Getting Started With Ipopt in 90 Minutes". In: *Combinatorial Scientific Computing*. Ed. by Uwe Naumann et al. Dagstuhl Seminar Proceedings 09061. Dagstuhl, Germany: Schloss Dagstuhl - Leibniz-Zentrum fuer Informatik, Germany, 2009. URL: <http://drops.dagstuhl.de/opus/volltexte/2009/2089>.

- [50] Andreas Wächter and Lorenz T Biegler. "On the implementation of an interior-point filter line-search algorithm for large-scale nonlinear programming". In: *Mathematical programming* 106.1 (2006), pp. 25–57.
- [51] Frederik Zahle et al. "Aero-elastic optimization of a 10 mw wind turbine". In: *33rd Wind Energy Symposium*. 2015, p. 0491.
- [52] Frederik Zahle et al. "Design of an aeroelastically tailored 10 MW wind turbine rotor". In: *Journal of Physics: Conference Series*. Vol. 753. 6. IOP Publishing. 2016, p. 062008.